

Journal of Astronomical Telescopes, Instruments, and Systems

AstronomicalTelescopes.SPIEDigitalLibrary.org

Polarization modeling and predictions for Daniel K. Inouye Solar Telescope part 5: impacts of enhanced mirror and dichroic coatings on system polarization calibration

David M. Harrington
Stacey R. Sueoka
Amanda J. White

SPIE.

David M. Harrington, Stacey R. Sueoka, Amanda J. White, "Polarization modeling and predictions for Daniel K. Inouye Solar Telescope part 5: impacts of enhanced mirror and dichroic coatings on system polarization calibration," *J. Astron. Telesc. Instrum. Syst.* **5**(3), 038001 (2019), doi: 10.1117/1.JATIS.5.3.038001.

Polarization modeling and predictions for Daniel K. Inouye Solar Telescope part 5: impacts of enhanced mirror and dichroic coatings on system polarization calibration

David M. Harrington,* Stacey R. Sueoka, and Amanda J. White
National Solar Observatory, Pukalani, Hawaii, United States

Abstract. The Daniel K. Inouye Solar Telescope (DKIST) is designed to deliver accurate spectropolarimetric calibrations across a wide wavelength range and large field of view for solar disk, limb, and coronal observations. DKIST instruments deliver spectral resolving powers of up to 300,000 in multiple cameras of multiple instruments sampling nanometer scale bandpasses. We require detailed knowledge of optical coatings on all optics to ensure that we can predict and calibrate the polarization behavior of the system. Optical coatings can be metals protected by many dielectric layers or several-micron-thick dichroics. Strong spectral gradients up to 60 deg retardance per nanometer wavelength and several percent diattenuation per nanometer wavelength are observed in such coatings. Often, optical coatings are not specified with spectral gradient targets for polarimetry in combination with both average- and spectral threshold-type specifications. DKIST has a suite of interchangeable dichroic beam splitters using up to 96 layers. We apply the Berreman formalism in open-source Python scripts to derive coating polarization behavior. We present high spectral resolution examples on dichroics where transmission can drop 10% with associated polarization changes over a 1-nm spectral bandpass in both mirrors and dichroics. We worked with a vendor to design dichroic coatings with relatively benign polarization properties that pass spectral gradient requirements and polarization requirements in addition to reflectivity. We now have the ability to fit multilayer coating designs which allow us to predict system-level polarization properties of mirrors, antireflection coatings, and dichroics at arbitrary incidence angles, high spectral resolving power, and on curved surfaces through optical modeling software packages. Performance predictions for polarization at large astronomical telescopes require significant metrology efforts on individual optical components combined with system-level modeling efforts. We show our custom-built laboratory spectropolarimeter and metrology efforts on protected metal mirrors, antireflection coatings, and dichroic mirror samples. © The Authors. Published by SPIE under a Creative Commons Attribution 4.0 Unported License. Distribution or reproduction of this work in whole or in part requires full attribution of the original publication, including its DOI. [DOI: [10.1117/1.JATIS.5.3.038001](https://doi.org/10.1117/1.JATIS.5.3.038001)]

Keywords: instrumentation; polarization; Mueller matrix; Daniel K; Inouye Solar Telescope; spectropolarimetry.

Paper 18131 received Dec. 27, 2018; accepted for publication May 8, 2019; published online Jun. 3, 2019.

1 DKIST Optics and Polarization Models for Calibration

The Daniel K. Inouye Solar Telescope (DKIST) on Haleakalā, Maui, Hawai'i, is presently under construction with operations beginning around 2020. The telescope has a 4.2-m off-axis F/2 primary mirror (4.0 m illuminated) and a suite of polarimetric instrumentation in a Coudé Laboratory (CL).^{1–3} Many of the proposed science cases rely on high spectral resolution polarimetry with imaging capabilities from scanning or tilting the instrument. Optics allow for stepping of spectrograph slits, scanning through wavelengths with Fabry–Pérot interferometers and using imaging fiber bundles to create imaging spectropolarimetric capability over visible and near-infrared (NIR) wavelengths covering wide fields of view. Many science cases require strictly simultaneous observation of several spectral lines with multiple instruments. DKIST can operate up to eight polarimetric cameras simultaneously to achieve these goals.

DKIST uses seven mirrors to collect and relay light to a rotating CL to provide flexible capabilities.^{1,4–8} Operations involve

four polarimetric instruments presently spanning the 380- to 5000-nm wavelength range. We also have two high-speed imagers covering visible and NIR wavelengths. A sequence of dichroic beam splitters (and optionally windows or mirrors) called the facility instrument distribution optics (FIDO) allows for changing of instrument configurations on a timescale of less than half an hour. The FIDO optics allow simultaneous operation of three polarimetric instruments optimized from 380 to 1800 nm, while all using the adaptive optics (AO) system for correction.^{7–10} Another instrument [cryogenic near-infrared spectropolarimeter (Cryo-NIRSP)] can receive all wavelengths to 5000 nm but without using the AO system. We refer the readers to recent papers outlining the various capabilities of the first-light instruments.^{1,3,5,7,8}

This paper is part of a series investigating polarization performance expectations for the DKIST instrument suite. In HS17,¹¹ we outlined the DKIST optical layout and properties of a very simple enhanced silver mirror coating model. This coating recipe was used in Zemax to estimate the field of view and beam footprint variation of the combined system optics to visible spectropolarimeter (ViSP) and Cryo-NIRSP. We also showed the predicted Mueller matrix for the DKIST primary and secondary mirrors, mounted ahead of our

*Address all correspondence to David M. Harrington, E-mail: dharrington@nso.edu

calibration optics. In H17a,¹² we showed polarization calibrations of a nighttime telescope and system calibrations with a ViSP using the daytime sky. In H18,¹³ we applied the Berreman calculus^{14,15} to polarization fringes formed in multilayer crystals with predictions and data collected in the laboratory and at a solar telescope. We then extended this calculus in HS18¹⁶ to converging and diverging beams. Fringes were measured at various focal ratios and compared to simulations in converging beams at solar and nighttime telescopes as well as in the laboratory. We also showed thermal models for the DKIST retarders along with thermal perturbation models for the polarization fringes.¹⁶ We recently have investigated spatial variation of retardance across multilayer retarders made of polished crystals, stretched polycarbonate, and ferroelectric liquid crystals in HS18b.¹⁷ This variation was then included in the DKIST optical model to show polarization calibration errors as functions of field angle and wavelength. We used a definition of calibration efficiency to show how we can use a single calibration retarder to simultaneously and efficiently calibrate all DKIST instruments from 380 to 1650 nm, representing the entire first-light AO-corrected suite. In this paper, we extend the coating model efforts of HS17¹¹ to many vendors, highly enhanced metals, hundred-layer dichroics, and our system of beam splitters. We present measurements and coating models for all optics presently coated in the DKIST telescope and most of the first-light instrument suite along with system-level predictions for polarization performance. We show some issues with complex coating formulas particularly for our high spectral resolving power instrument suite. We introduce tolerance analysis at the system level, given new measurements of spatial and shot-to-shot coating variability.

We show in Fig. 1 the optical and mechanical layouts of the instruments in the CL. The left-hand graphic shows the optical Zemax model of the instruments with the beam propagating to the various focal planes close to where polarization modulation occurs. The dark blue beam shows the diffraction limited near-infrared spectropolarimeter (DL-NIRSP), which uses an imaging fiber bundle to create spectropolarimetric images on

three separate cameras. The light blue beam shows the ViSP which uses a slit to scan the field of view while imaging simultaneously with three separate cameras. The magenta beam shows the visible tunable filter (VTF) imaging through a Fabry–Pérot type spectropolarimeter. These three instruments represent the available post-AO polarimetric instrumentation. There are also two high-speed imaging systems collectively called the visible broadband imager (VBI) with red and blue channels. Additional instrumentation is associated with the AO system low-order wavefront sensor (WFS) and high-order WFS. All AO instruments see the first beam splitter associated with the WFS-BS1 in transmission. The high-order WFS is fed by the Fresnel reflection off the uncoated surface of WFS-BS1, as seen by the cyan-colored rays in Fig. 1.

Complex polarization modulation and calibration strategies are required for such a multi-instrument system.^{7,8,18–20} At present design, three different retarders are in fabrication for use in calibration near the Gregorian focus.^{7,18,21} The planned 4-m European Solar Telescope (EST), though on-axis, will also require similar calibration considerations.^{22–24} The upcoming Chinese Giant Solar Telescope is exploring segmented designs and modeling coating variability between segments.^{25,26} Many solar and nighttime telescopes have performed polarization calibration of complex optical pathways.^{27–49}

As part of the CL, there are multiple interchangeable dichroic beam splitters, windows, and mirrors collectively called the FIDO. The FIDO optics is configurable to distribute various wavelengths to different instruments as observers require. The optics is mounted in stations labeled following a CL station numbering system CL2 and CL3. As all AO-assisted instruments see the first beam splitter WFS-BS1 in transmission, we start the numbering system at 2. The optics is designed such that the wedge angles are matched in each optic, and every instrument sees either two or four beam splitters in transmission to compensate for the wedge and associated wavelength variation in beam deflection. The two stations CL2 and CL3 use a reflection off the optic. There are two optical stations after these reflections named CL2a and CL3a, respectively. We show a

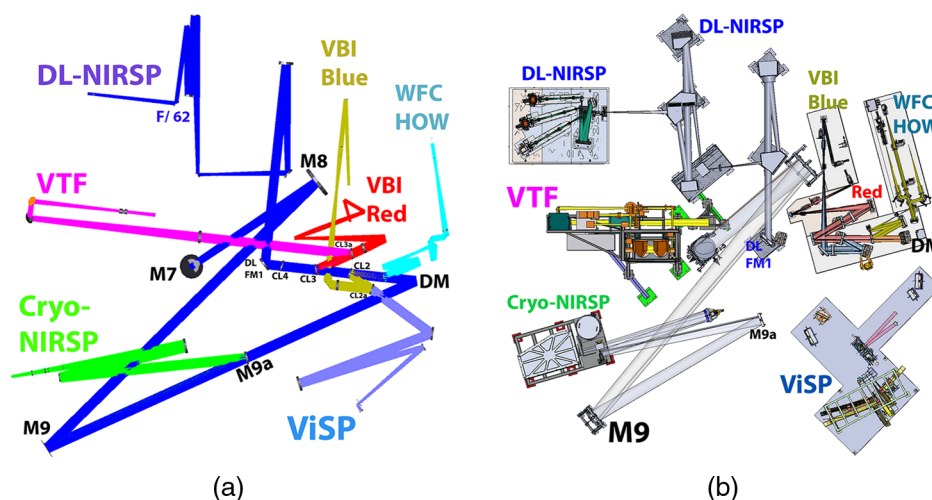


Fig. 1 (a) DKIST CL optical Zemax model and (b) mechanical model. The telescope feeds the beam at $F/53$ to the CL. M7 folds the beam level with the lab floor. M8 collimates the beam. M9 directs the beam toward various instruments. The FIDO system of dichroics sends selectable wavelength ranges simultaneously toward various combinations of instruments (ViSP, VTF, DL-NIRSP, and VBI). Each instrument has multiple cameras used simultaneously. The optional M9a directs the entire beam toward Cryo-NIRSP.

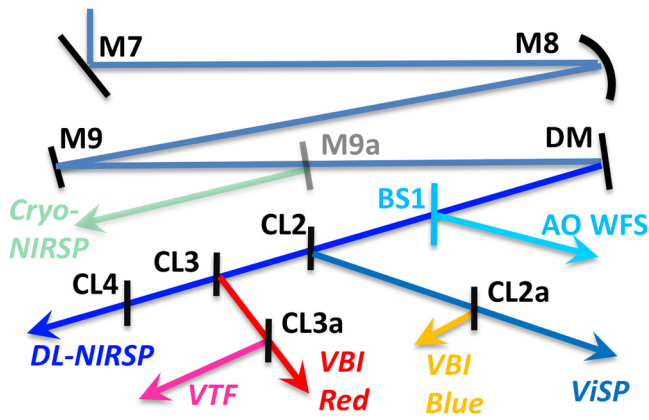


Fig. 2 The CL cartoon layout beginning with DKIST mirrors M7 through the deformable mirror M10 (DM). FIDO optic stations CL2, CL2a, CL3, CL3a, and CL4 can be configured using a suite of mirrors, windows, and dichroics to optimize the configuration for particular use cases. The first beam splitter is permanently mounted and feeds the WFS.

cartoon layout of the CL optics in Fig. 2. We follow the same color convention as in Fig. 1. The FIDO mirrors, dichroics, and windows interchangeably used in the CL stations will be discussed in later sections. There is a separate instrument that does not use the AO but instead uses a seeing limited, all-reflective beam path. The Cryo-NIRSP covers wavelengths up to 5000 nm by inserting a pickoff mirror before the AO system.

Each of the instruments is built by different teams with a variety of mirror coatings, often using multiple formulas from multiple vendors in several independent coating chamber shots. The DKIST instrument mirrors can be just one or two protective layers up to very complex enhanced protected-type coatings with 29 dielectric layers over the metal and a coating thickness of over 3 μm . The interchangeable FIDO mirrors, windows, and dichroics are provided by DKIST and also have a diversity of coatings. The dichroic coating designs include up to nearly 100 dielectric layers and thickness of 9 μm . These coatings can produce spectrally diverse and complex behavior requiring a detailed treatment, as outlined in this paper.

DKIST is designed as a multidecade lifespan facility supporting a diverse array of use cases with a suite of polarimeters. The slit spectropolarimeter, integral field fiber-fed imaging spectropolarimeter, and the above-described Fabry–Pérot imaging spectropolarimeter step or scan across solar features on disk, limb, and corona. Often multiple cameras within multiple instruments work in concert with both active and adaptive optics locking onto nearby solar features for wavefront correction and pointing stabilization. The suite of instruments is designed to be flexible in configuration, upgradable, stable in calibration, and support an incredibly diverse range of science objectives.

Within the current DKIST science planning process, there are already hundreds of proposed observing cases spanning near-ultraviolet wavelengths (0.393 μm) to thermal infrared (4.6 μm) often with several cameras on several instruments operating simultaneously. The expected flux levels from on-disk observations at visible wavelengths to coronal observations in the thermal infrared range in amplitude by at least factors of millions. Very large changes are also anticipated in spatial and

spectral sampling, camera frame rates, modulation strategies, and time-to-noise limits. Some use cases are seeing limited without AO and are sampled coarsely to achieve very high sensitivity. Other cases use the AO system to achieve diffraction-limited performance with sampling at the highest spatial and spectral powers delivered. The DKIST AO system has 1600 actuators and is anticipated to deliver Strehl ratios of 0.3 at 500-nm wavelength in median seeing conditions.^{4,6,50} The DKIST upgrade to multiconjugate AO already in progress should push delivered high-Strehl performance to wider fields.^{51–53} Polarization modulation speeds can span multiple orders of magnitude (e.g., the ferroelectric liquid crystal modulator in VTF is capable of kiloHertz rates versus discrete modulation on timescales <0.01 Hz for coronal observations with DL-NIRSP or Cryo-NIRSP).^{9,54}

Expected solar magnetic field strengths can range from a fraction of a Gauss spatially unresolved below the DKIST diffraction limit to several kilogausses covering the entire instantaneous field of view of a DKIST instrument. Translation of an error in magnetic field to an error in measured Stokes vectors implies some numerical techniques to relate changes in modeled field properties to errors in a measurement through some kind of atmospheric model and inversion process. A general, instrument-unspecific framework to systematically relate the error bars in a Stokes measurement to the error bars in a magnetic field through an inversion code does not exist. Often, specific measured Stokes vectors can be perturbed by changing the assumed instrument calibrations to assess field errors such as in Sec. 12 of Jaeggli.⁵⁵ Signal-to-noise estimates and simple models for instabilities of individual components can also be related to field uncertainties in specific cases.⁵⁶

Detailed performance predictions are useful in assessing the inaccuracies that can arise when observing and calibrating across such a wide range of instrument configurations. We also find the system-level performance predictions useful in estimating the magnitude of variations and assessing the calibration techniques required. We require knowledge of the optical surfaces, the coating behavior across field angle and pupil position, and the modes of intended use (slit scanning, pupil steering, and temporal sampling). For calibrations to be accurate, we must assess the magnitude of expected errors and the stability of all components in the optical system.

Often, most science cases call for continuum polarization stability so that the zero point and length of the recovered Stokes vector is comparable between different instrument pointings (sometimes called the image mosaic, field mosaic, or other terms of varying applicability). The requirements on the orientation of the vector (which manifest from retardance spatial variation and other coordinate geometry issues) are often less stringent as a few degrees of orientation variation in a recovered Stokes vector does not directly impact comparison of differing solar atmosphere models. Depolarization is often ignored as it is usually a small fraction of a percent change in the magnitude of a recovered Stokes vector, and it can be modeled with proper system-level tools (e.g., for DKIST¹¹).

With this paper, we extend our prior modeling efforts to include several parameters of optical coatings required for a realistic system-level modeling. Any altitude-azimuth telescope with a nonzero field of view has temporal dependence across the field as mirror groups change their relative geometry. Realistic coatings are not identical between coating runs and are only within manufacturing tolerances of nominal designs.

Polarization properties of real coated mirrors never cancel perfectly. The transmission, diattenuation, polarizance, and retardance parameters can be individually perturbed by field rotation, spatially nonuniform coatings, and optical instabilities. By knowing the wavelength dependence of the system performance at high spectral resolving power, we can effectively plan for calibrations at appropriate configurations (e.g., spectral resolution, field scanning, spatial sampling, and temporal averaging). We also design coatings that do not cause undue calibration challenges, such as coatings changing retardance by >1 wave in a few nanometer of wavelength. This work updates performance models that will inform limits to the accuracy of calibration techniques when we decide how wide of a field we can step, modes for field scanning, available spectral binning, and wavelength interpolation. Some of these updates will be included in the instrument performance calculators used in planning observations (published online at Ref. 57).

1.1 Mirror Grouping Models, Polarization, and System Mueller Matrices

We create a polarization model for the telescope and the suite of instruments using our knowledge of the optical coatings and substrates. We have shown, in HS17,⁵⁸ some predictions for the polarization behavior of the telescope and instrument feed optics using nominal coating formulas derived with the Zemax-provided refractive indices. We have shown that the mirrors introduce some slight field-of-view dependence for the polarization calibration as well as a very mild depolarization from our off-axis primary and secondary mirrors. The magnitude of field-dependent variation shown in our prior work⁵⁸ is not changed by our work presented here. In this paper, we consider only the on-axis beam at the nominal instrument boresight. Field-of-view considerations represent a significant complication. A common technique for simplifying the system polarization models is to group mirrors together that maintain a fixed orientation with respect to each other. We call this the group model. For DKIST systems engineering, we also need to predict the Mueller matrix of the system while accounting for polarization properties of the many mirrors mounted in front of the polarization modulators in each instrument. The basic calibration plan is to use the DKIST calibration optics to simultaneously fit for the telescope group model, the modulation matrix of the instruments and certain properties of the calibration optics. We show here the mathematics behind some of the simplifications assumed in the group model. We then assess how to predict these terms in later sections of the paper.

In this work, we denote the Stokes vector as $\mathbf{S} = [I, Q, U, V]^T$. In this formalism, I represents the total intensity, Q and U are the linearly polarized intensity along polarization position angles 0 deg and 45 deg in the plane perpendicular to the light beam, and V is the right-handed circularly polarized intensity. The typical convention for astronomical polarimetry by the International Astronomical Union is for the $+Q$ electric field vibration direction to be aligned to celestial North–South, while $+U$ has the electric field vibration direction aligned to North–East and South–West. The propagation axis points toward the observer. In laboratory settings, frequently, $+Q$ is defined as horizontal or vertical. For solar studies, a common definition is to have $+Q$ parallel to the solar equator or in the positive right ascension direction^{59–61}

$$\mathbf{M}_{ij} = \begin{pmatrix} II & QI & UI & VI \\ IQ & QQ & UQ & VQ \\ IU & QU & UU & VU \\ IV & QV & UV & VV \end{pmatrix}. \quad (1)$$

The Mueller matrix is the 4×4 matrix that transfers Stokes vectors.^{62–64} Each element of the Mueller matrix is denoted as the transfer coefficient.^{64,65} For instance, the coefficient $[0, 1]$ in the first row transfers Q to I and is denoted as QI . The first row terms are denoted as II , QI , UI , and VI . The first column of the Mueller matrix elements are II , IQ , IU , and IV . In this paper, we will use the notation in Eq. (1). The output Stokes vector is related to the input vector via a simple transfer equation $\mathbf{S}_{i\text{output}} = \mathbf{M}_{ij} \mathbf{S}_{i\text{input}}$. With this formalism, the Stokes vector from some patch of solar atmosphere would be transferred by the Mueller matrix of each optic between the Sun and the sensor.

We adopt a notation where a rotation is denoted as \mathbb{R} . We note that a rotation of a Mueller matrix must include rotations on both sides of the matrix to preserve input coordinate systems: $\mathbb{R}(-\theta) \mathbf{M} \mathbb{R}(-\theta)$. There are three main coordinate rotations in DKIST. The elevation axis is between M4 and M5 (\mathbb{R}_{E_I}). The azimuth axis is between M6 and M7 (\mathbb{R}_{A_z}). The DKIST CL is on a rotating platform so that there is a separate rotational degree of freedom with the coude angle in addition to the azimuth of the target (\mathbb{R}_{T_A})

$$\mathbf{S}_{\text{coude}} = \mathbb{R}_{T_A} \mathbb{R}_{A_z} \mathbf{M}_6 \mathbf{M}_5 \mathbb{R}_{E_I} \mathbf{M}_4 \mathbf{M}_3 \mathbf{M}_2 \mathbf{M}_1 \mathbf{S}_{\text{input}}, \quad (2)$$

$$\mathbf{S}_{\text{Cryo}} = \mathbf{M}_{\text{CFM}} \mathbf{M}_{\text{CSM}} \mathbf{M}_{9a} \mathbf{M}_9 \mathbf{M}_8 \mathbf{M}_7 \mathbf{S}_{\text{coude}}, \quad (3)$$

$$\mathbf{S}_{\text{thruAO}} = \mathbf{M}_{\text{BS1b}} \mathbf{M}_{\text{BS1f}} \mathbf{M}_{\text{DM}} \mathbf{M}_9 \mathbf{M}_8 \mathbf{M}_7 \mathbf{S}_{\text{coude}}. \quad (4)$$

There are six mirrors that collect the solar flux and relay the beam to the CL. The seventh mirror (M7) folds the beam onto the CL floor. The eighth mirror (M8) is an off-axis collimating mirror and the ninth mirror (M9) is a coma-correcting fold mirror with a specific figure. With this notation, we can explicitly compute the transfer equations to see how Stokes vectors will behave at various locations along the optical path. In Eq. (2), we show the input Stokes vector $\mathbf{S}_{\text{input}}$ being transferred from the telescope primary mirror to the CL $\mathbf{S}_{\text{coude}}$ just before reflecting off M7

$$\mathbf{S}_{\text{toDL}} = \mathbf{M}_{\text{CL4b}} \mathbf{M}_{\text{CL4f}} \mathbf{M}_{\text{CL3b}} \mathbf{M}_{\text{CL3f}} \mathbf{M}_{\text{CL2b}} \mathbf{M}_{\text{CL2f}} \mathbf{S}_{\text{thruAO}}, \quad (5)$$

$$\mathbf{S}_{\text{DL}} = \mathbf{M}_{\text{FM4}} \mathbf{M}_{\text{FM24}} \mathbf{M}_{\text{FSM}} \mathbf{M}_{\text{FM2}} \mathbf{M}_{\text{FM2}} \mathbf{M}_{\text{OAMI}} \mathbf{M}_{\text{FMI}} \mathbf{S}_{\text{toDL}}. \quad (6)$$

The instrument Cryo-NIRSP does not use the AO system. The system uses a pickoff flat mirror called M9a at 9-deg incidence angle that directs light to this instrument. The next mirror in the system is a flat pupil steering mirror we denote CSM working at 4-deg incidence angle. This is followed by the off-axis mirror focusing the beam at $F/18$ using a 1.1-deg fold angle-denoted CFM. The beam passes through the polarization modulator to the spectrograph entrance slit. Equation (3) shows the Mueller matrices transferring the CL Stokes vector to the Cryo-NIRSP modulator. The Cryo-NIRSP feed optics and modulator properties are described in our prior references.^{16,17,58,66}

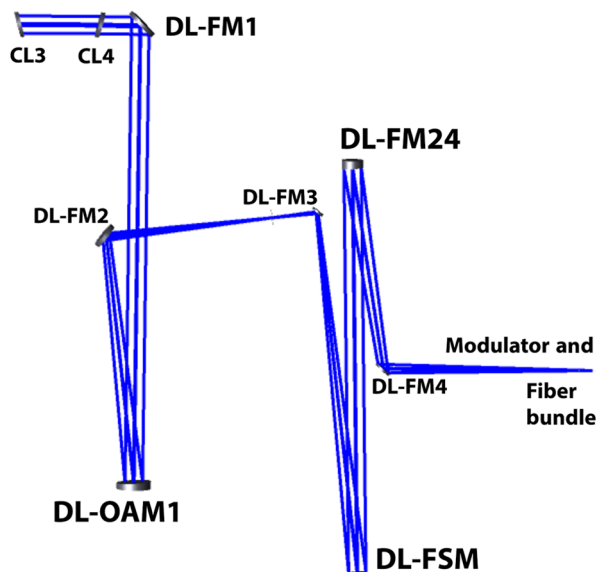


Fig. 3 The DL-NIRSP $F/24$ optical Zemax model from the CL3 FIDO optic station through the seven instrument reflections to the modulator and fiber bundle.

For the rest of the polarimetric instruments, the beam must propagate through the AO system, as shown in Eq. (4). The DL-NIRSP, ViSP, and VTF all see M7, M8, and M9 as well as the tenth mirror as the AO system deformable mirror ($DM = M10$). All instruments using the AO system must also account for the WFS-BS1 transmission and diattenuation from both the uncoated front surface and the broadband antireflection-coated wedged back surface, which we denote in Eq. (4) as BS1f and BS1b, respectively.

As an example of the Mueller matrix calculation, we show in Eq. (5) the dichroic coating front surface reflection and broadband antireflection-coated back surface reflections off the interchangeable FIDO optics feeding the DL-NIRSP instrument. We explicitly call out the optical stations CL2, CL3, and CL4 along with the separate Mueller matrices for the front and back surface reflections. We show later both theoretical models and polarimetric measurements for several of the FIDO dichroic coatings used for computing the system Mueller matrices.

The mirrors included in the DL-NIRSP relay optics also need to be included to compute the expected Mueller matrix of the system to the modulator. In Eq. (6), we show the optics transferring the Stokes vector exiting the last FIDO optic through the DL-NIRSP mirrors in the $F/24$ configuration to the modulator mounted in front of the imaging fiber bundle. The Zemax optical model for the on-axis field angle is seen in Fig. 3

$$\mathbf{S}_{\text{group}} = \mathbf{M}_{\text{Mod}} \mathbb{R}_{TA} \mathbb{R}_{Az} \mathbf{M}_{5,6} \mathbb{R}_{EI} \mathbf{M}_{3,4} \mathbf{M}_{1,2} \mathbf{S}_{\text{input}}. \quad (7)$$

The fundamental assumption of the group model is that the static optics can all be multiplied together and fit with a greatly reduced number of variables. For the present modeling efforts, we also ignore all field-of-view dependence though we can calculate magnitudes and make the models more complex as needed. We show the group model in Eq. (7).

The primary and secondary mirrors are ahead of the calibration optics so they are fit separately using a variety of techniques. The third mirror is near a focal plane and is actively pointed to maintain optical alignment by small amounts. The

third and fourth mirrors are modeled together as a group, ignoring the small angular offsets. The first four mirrors are upstream of the elevation axis. Similarly, M6 is near a pupil plane and is also tilted by small amounts to maintain optical alignment. The fifth and sixth mirrors are modeled together as a group. After the rotations about the azimuth and coudé table axes, all optics are fixed and become part of the Mueller matrix for all optics ahead of the modulator, denoted as \mathbf{M}_{Mod} . This Mueller matrix is expected to be computed for all field angles and wavelengths on every sensor and it includes all optics in the relay optics, AO system, FIDO, and within the instruments

$$\begin{pmatrix} II & QI/II & UI/II & VI/II \\ IQ/II & QQ/II & UQ/II & VQ/II \\ IU/II & QU/II & UU/II & VU/II \\ IV/II & QV/II & UV/II & VV/II \end{pmatrix}. \quad (8)$$

We have shown an example for DL-NIRSP with the $F/24$ configuration in Eqs. (4)–(6). The Mueller matrix combines polarization behavior of six surfaces through the feed optics and AO system, six surfaces with complex dichroic coatings in FIDO, and another seven mirror surfaces inside DL-NIRSP ahead of the modulator. For any configuration change in FIDO or an instrument, the Mueller matrix must be calculated. This Mueller matrix will be computed for several example FIDO configurations later in this paper. Later in this paper, we provide an assessment of the sensitivity to mirror coating properties on each mirror. The assumptions underlying the simplifications in the group model will also be assessed.

We will also adopt an astronomical convention for displaying Mueller matrices where we will normalize every element by the II element to remove the influence of transmission on the other matrix elements, as seen in Eq. (8). Thus, subsequent figures will display a matrix that is not formally a Mueller matrix but is convenient for displaying the separate effects of transmission, retardance, and diattenuation in simple forms. The transmission is shown in the $[0,0]$ element, while all other elements are normalized by transmission for convenient interpretation.

1.2 Summary: Optical Path and Predicting System Polarization

We have outlined the DKIST optical path to the CL through the instruments to the modulating retarders. We have provided a model for polarization of the various optics in the system by functional groups called the group model. The six mirrors between the sky and the CL are combined into three groups that rotate with respect to one another. We have then shown how the Mueller matrices of the coudé relay optics, the AO system, the FIDO dichroics, and internal instrument optics are combined into a single Mueller matrix representing all optics ahead of the polarization modulator. We have shown an example of the DL-NIRSP instrument in the $F/24$ configuration and describe the 19 optical surfaces that will impact this system Mueller matrix. The ViSP and Cryo-NIRSP instruments are described in a prior reference.¹¹ Next, we have shown how we can measure polarization properties of coated optics in reflection and transmission. We have examined the mirror data sets and repeatability in Sec. 2. Section 3 shows examples of fitting mirror coating models to data sets along with a comparison of metrology for retardance and diattenuation from multiple instruments. We have shown broadband antireflection coatings



Fig. 4 The NLSP installed in the Boulder laboratory.

in Sec. 4 used in DKIST beam splitters and calibration optics. Models for FIDO dichroic coatings and examples from our vendor are shown in Sec. 5. We have discussed transmission and polarization artifacts only seen at high spectral resolving power. We have then combined this coating information to show predictions of the group model parameters and the Mueller matrix from the derived optical coating properties of all optics between the sky and the polarimeter. The combined spectral behavior of the mirrors, beam splitters, and windows is assessed in a few anticipated DKIST observing configurations in Sec. 6.

2 NSO Laboratory Spectropolarimeter and Performance

The National Solar Observatory Laboratory Spectropolarimeter (NLSP) uses two spectrographs to simultaneously measure polarized spectra with a wire grid polarizing beam splitter (PBS). We use a collimated optical setup for polarization measurement. A fiber-coupled light source is collimated by an achromatic doublet lens and then stopped to a circular beam of 4-mm diameter using laser cut masks. This provides a narrow-field, uniform, collimated light source. A polarization state generator consists of a rotating wire grid polarizer and rotating third-wave achromatic linear retarder mounted upstream of the sample location. After the sample, a rotating third-wave linear retarder is mounted as a modulator. The final optic is a fixed orientation-analyzing wire grid polarizer, which is also used as a PBS. As detectors, we use visible and NIR spectrographs from Avantes. The visible spectrograph covers 380 to 1200 nm, while the NIR spectrograph covers 900- to 1650-nm wavelength.

The beam transmitted through the wire grid polarizer feeds the visible spectrograph via filters, aperture stops, and a lens. At the lens focus, a fiber couples light to the spectrograph. The beam reflected off the wire grid polarizer is passed through a separate set of filter, aperture stop, and lens optics into the NIR spectrograph. This NIR arm has an additional polarizer with wires parallel to the analyzer to remove the Fresnel reflection component off the glass and to maintain high contrast. Figure 4 shows a picture of the system with the polarization state generator half on the right and the spectropolarimeter half on the left. The sample under test goes on the rotation and translation stage in between the two sides.

We have a reflective configuration for NLSP where a sample can reflect the beam to an additional set of optics. As this

reflective setup must always have an optic in the sample location, we cannot calibrate absolute reflectivity. But we can use our calibration of the system optics to measure the retardance and diattenuation of the sample. Presently, we have only calibrated this channel at a fixed incidence angle (AOI) of 45 deg, but the system is capable of a much wider range of angles. The sample is mounted on a rotation stage controlling AOI which itself is mounted on a translation stage.

The mirrors for the DKIST optics and the coudé instruments are provided by various instrument partners who use a range of commercial vendors. There is a great diversity of enhanced protected, protected, and bare metal mirrors in the path between the sun and any DKIST camera. In addition, many-layered dielectric dichroic coatings are part of the FIDO system. The ViSP will see one dichroic coating in reflection and another in transmission with the appropriate antireflection coating at 15-deg incidence. The VTF will see one dichroic in transmission and two in reflection. The DL-NIRSP will see three dichroics in transmission with the three antireflection coatings. All these instruments will see the WFS beam splitter in transmission with a broadband antireflection coating on the back side.

In Table 1, we list many samples of the DKIST-enhanced protected silver coating that we tested. We show the many witness samples collected from coating shots of the identical formula procured for the DKIST telescope optics, as well as two of the coudé instrument: DL-NIRSP and Cryo-NIRSP and preliminary evaluation samples from an unknown run. These witness samples represent what should be identical coatings spatially across the chamber over many repeated coating shots. The N column shows how many witness samples we have from each run, representing different spatial positions within the coating chamber. The run 13BE18 is noted as both the mirror and the witness sample substrates are SiC. We also note that run 14BE04 contained both DKIST mirrors M3 and the spare M6. We received a sample from the coating shot just before M4, which we denote as $M4_{pre}$. We also have a spare fifth mirror denoted as $M5_s$. For the specific case of the DL-NIRSP mirror DL F00-207, we did not receive a sample, but this is a small flat optic so we tested the optic directly. One of the samples from the DL-NIRSP team was labeled 16BE15/17 but the sample had

Table 1 DKIST enhanced Ag mirror samples.

Name	Run	N	Name	Run	N
DKIST M2	13BE18	2	DKIST Eval 1	Unknown	1
DKIST M3	14BE04	1	DKIST Eval 2	Unknown	1
DKIST $M4_{pre}$	15BA34	1	DKIST Eval 3	Unknown	1
DKIST M4	15BA35	2	Cryo-NIRSP 1	16BB07	1
DKIST M5	12BD18	1	Cryo-NIRSP 2	16BB21	1
DKIST $M5_s$	12BD19	1	Cryo-NIRSP P	16BD15	2
DKIST M6	14BE05	1	DL-NIRSP 1	16BE16	1
DKIST $M6_s$	14BE04	1	DL-NIRSP 1a	16BE17	1
DKIST M7	16BD16	1	DL-NIRSP 1b	16BE17	1
DKIST M10	15BA23	4	DL F00-207	16BB22	1

Table 2 Other Ag and Al mirror samples.

Name	Run	<i>N</i>
DKIST M1	AFRL bare Al	2
DKIST M1 spare	AFRL bare Al	2
FIDO samples		
IOI Enh. ProtAg	EAg-300 5-5033	1
IOI Enh. ProtAg	EAg-700 8-6282	1
IOI Enh. ProtAg	EAg1-450 8-6898	1
FIDO C-M1 _{pre}	EAg1-420 6-7759	2
FIDO C-M1	EAg1-420 6-7766	3
ViSP recoat	EAg1-420 6-7767	3
DKIST M9	EAg1-450 9-3095	3
Other samples		
DL-NIRSP EMF	Protected Ag	1
DKIST M8 EMF	Protected Ag99b	3
ViSP Very-EAg	29 layer + Ag	2
ViSP RMI EAg	Protected enhanced Ag	2
Zygo M9a Samp.	Protected enhanced Ag	4
Zygo DL-FM1	Protected enhanced Ag	1
BBSO newport	Protected enhanced Ag	2
GREGOR	Protected Ag	2
Thorlabs	Protected Ag	3
Edmund Optics ^{vbi}	Protected Ag	1
Edmund Optics	Protected Ag	4

16BE17 marked on the side so we make the assumption that this is a separate spatial position for 16BE17 that we denote as 1b, which is shown as italics in Table 1.

We show several alternate coating samples in Table 2. We have the bare aluminum coatings from the 4-m primary mirror as well as the spare commissioning mirror both done by the Air Force Research Labs (AFRL) on Haleakala, adjacent to DKIST. We tested the enhanced protected silver mirror samples from Infinite Optics, Inc. (IOI) during FIDO mirror and dichroic coating assessments. We had been given coating designs, reflectivity, and diattenuation along with samples for enhanced silver (EAg) formula names 300, 700, 1-420, and 1-450. We are partly through coating several other DKIST mirrors (M9 and the FIDO mirrors) with an IOI coating. We also note that three of the ViSP mirrors were originally a very enhanced 29-layer silver coating that was subsequently stripped and recoated with the IOI coating EAg1-420.

The bottom section of Table 2 shows witness samples that we have tested from commercial sources. Some will be used in DKIST, while others are used at other solar telescopes, including

the Big Bear Solar Observatory (BBSO) Goode Solar Telescope (GST, formerly the New Solar Telescope, NST), and the GREGOR solar telescope. The two samples from the very-enhanced ViSP mirrors have been tested. There is an additional large flat from Edmund Optics procured for the DKIST VBI-blue instrument that we tested and is denoted in Table 2. This mirror is likely similar to some of the BBSO mirrors from Edmund Optics with a catalog protected silver coating. We later bought four small samples from Edmund Optics nominally with the same protected silver coating to assess variability. We also include the three Thorlabs-protected silver mirrors that we used at NSO for laboratory testing. These samples were all procured at one time but without any guarantee of being from the same coating shot. On some DL-NIRSP mirrors, the nominal DKIST-specified silver formula has not been procured. We also show measurements of this alternate protected silver coating by Dynasil's evaporated metal films (EMFs). The team did not receive witness samples for this alternate coating so we tested the DL-NIRSP spectrograph flat optic F00-201 directly in NLSP. We also coated DKIST M8 at EMF with a blue-enhanced version of the Ag99 coating that we label as Ag99b. Zygo Corporation provided four samples of their nominal enhanced protected silver coating as part of the FIDO project coating the removable mirror feeding Cryo-NIRSP (M9a). Zygo also coated the fold mirror to DL-NIRSP after the sequence of beam splitters (DL-FM1). We also obtained a sample from the two coating runs of the enhanced protected silver used for the ViSP internal fold mirrors. One of these folds is after the coated slit mask and impacts the system polarization modulation matrix.

We demonstrate here the use of the Berreman calculus to fit the coating data from NLSP as well as to compare polarization performance of various coated mirrors and dielectrics. We use the common equation for a Mueller matrix derived from a single flat fold. Details of the Mueller matrix equations used are in Sec. 12. The reflectivities parallel and perpendicular to the plane of incidence (R_p and R_s) can be used to derive the transmission and diattenuation terms. In the normalized Mueller matrix, the IQ/II and QI/II terms are a normalized reflectivity difference ratio $(R_s - R_p)/(R_s + R_p)$. The retardance (δ) is a term in the UV rotation matrix in the lower right quadrant.

With NLSP, we are able to characterize the coatings as applied to DKIST telescope and instrument optics. In any manufacturing process, there will be variation. The witness samples from a nominal coating formula applied by a vendor well within manufacturing tolerances to several DKIST optics and to the DL-NIRSP and Cryo-NIRSP instrument feed optics are shown in Fig. 5. The curves show retardance varying from under 150 deg to just over 200 deg. The different color curves highlight how the coating applied to the DL-NIRSP instrument gives significantly different results in retardance from the DKIST telescope optics and the Cryo-NIRSP feed optics. The solid red horizontal line in Fig. 5 shows how the wavelength of zero net mirror retardance varies from 810 to 885 nm depending on the coating.

These retardance changes can be caused by only a few nanometers variation in thickness of a dielectric layer in a multilayer coating. These variations are well within typical manufacturing tolerances and are entirely expected, particularly when retardance or diattenuation targets are not included in the coating specifications. The reflectivity of all our mirrors easily passes

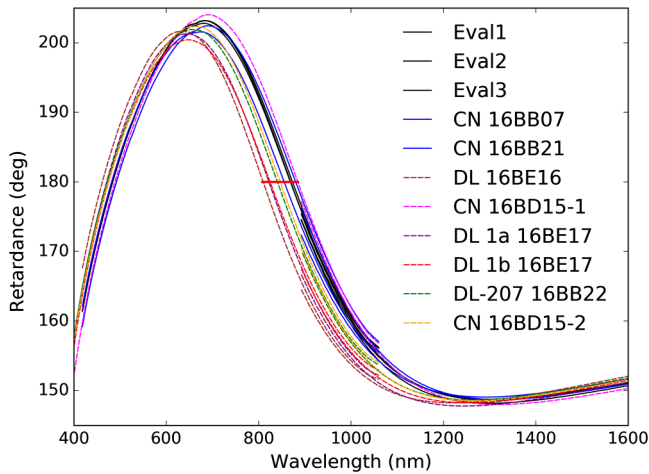


Fig. 5 The retardance computed from the Mueller matrix elements measured with the reflective arm of NLSP at 45-deg incidence angle. The measured retardance is near the theoretical unperturbed 180-deg at two wavelengths, around 460 and 810 nm. The short horizontal bar shows a 60-nm spread in wavelengths for 180-deg retardance in the NIR. We separately show the visible and NIR spectrograph data sets with good agreement in the 900- to 1100-nm wavelength overlap range.

the DKIST reflectance criteria. The NLSP-measured retardance differences are orders of magnitude larger than the NLSP sensitivity and we show later in this paper how these changes impact the system polarization performance predictions.

3 Mirror Coating Models and Fits to Polarization

We begin assessing the DKIST coatings by following our previously published technique^{11,67} to select a simple one- or two-layer coating model. We identify the best fit of the model retardance to the NLSP measurements using only the thickness of the dielectric coating layers as variables. The refractive

indices of the layer materials are interpolated from lookup tables derived from public references such as refractiveindex.info. This simple method is quite limited in that only retardance is fit, not diattenuation or reflectivity. An additional limitation is that only a single incidence angle is used in the fit. However, having a model coating that reasonably reproduces the spectral behavior and magnitude of retardance, diattenuation, and reflectivity allows us to estimate the magnitude of several types of polarization artifacts possible in DKIST. We provide more details below and in Sec. 10.

Any imperfections in knowledge of the materials, number of layers, or material refractive index will degrade the model fit. A grid of coating retardance models are computed for each thickness of the dielectric material. The predicted retardance is then subtracted from the NLSP data to create an error curve. These retardance error curves are squared and summed to create a single wavelength averaged error metric which is minimized to determine the fit. In the left-hand graphic of Fig. 6, we show two example retardance curves for the DKIST-enhanced protected silver samples. The solid black line shows measurements of a witness sample for the DKIST instrument DL-NIRSP. The dashed dark blue line shows an example fit model coating of ZnS at 8-nm thickness coated over 100 nm of Al₂O₃ using the Boidin et al.⁶⁸ refractive index formula on top of silver. This coating has the theoretical 180-deg retardance upon reflection at wavelengths of 462 and 810 nm.

The solid blue line of Fig. 6 shows another DKIST witness sample of the same coating formula but from a different shot than the DL-NIRSP instrument shown in black. There is some normal and expected shot-to-shot variation in the manufacturing process. The dashed red line in the left-hand graphic shows an example fit model coating of ZnS at 10-nm thickness coated over 105 nm of Al₂O₃ using the Boidin et al.⁶⁸ refractive index formula on top of silver. This coating has the theoretical 180-deg retardance upon reflection at wavelengths of 483 and 870 nm, which corresponds to a change of 21- and 60-nm wavelength, respectively, from the prior coating shot. This coating

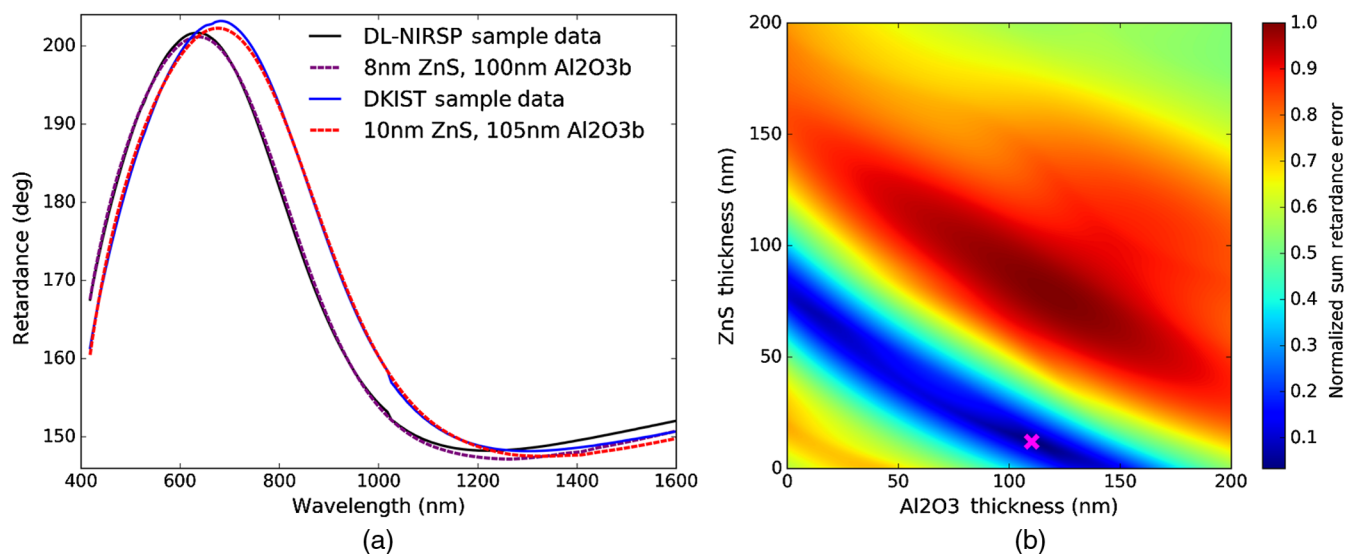


Fig. 6 (a) Shows measured and modeled retardance curves for two enhanced protected silver samples. The solid curves show NLSP measurements and dashed curves show best-fit two-layer coating models. (b) Shows the wavelength averaged retardance error normalized from 0 to 1 for a two-layer protective coating of ZnS over Al₂O₃ on top of the silver base layer.

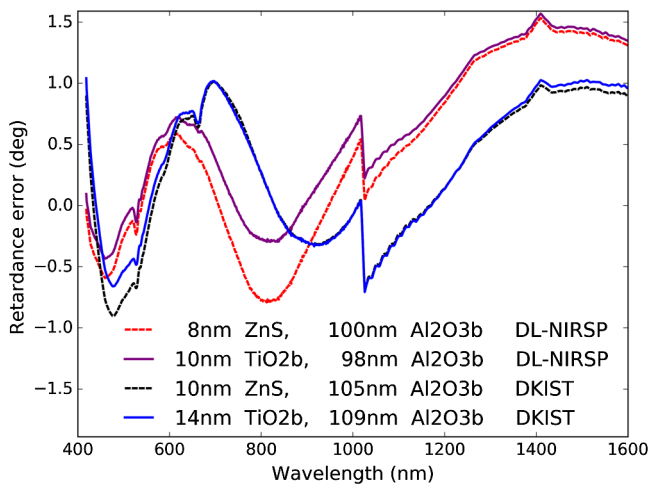


Fig. 7 The difference between retardance data and models for a reflection off a DKIST-enhanced protected silver sample following Fig. 6(a). Residuals are roughly 1-deg retardance but are orders of magnitude larger than our statistical limits. The step in error at 1020-nm wavelength is caused by the change between visible and NIR spectrographs.

model fit is different from the DL-NIRSP sample by about 2 nm in the top ZnS layer and 5 nm in the bottom Al_2O_3 layer. The retardance fits match the appropriate data set well and are very significantly different from each other.

This technique uses a simple brute-force search of the possible coating formulas and is limited to a very small number of variables. Essentially two thicknesses are fit but the refractive index wavelength dependence for each dielectric must be specified as well as the wavelength range over which to compute errors. The right-hand plot of Fig. 6 shows the wavelength averaged error value on a color scale for the DKIST sample against the thickness for the ZnS and Al_2O_3 layers. Red shows high error values, while dark blue into black shows the error minimum values. The magenta cross marks the coating model solution identified with this simple brute-force method.

Figure 7 shows the difference between a few best-fit models and the NLSP data sets. We follow same color scheme as Fig. 6 for coating models made with the various ZnS and Al_2O_3 refractive index models. We also now include a new model with the TiO_2 refractive index equation from Boidin as the top coating layer. The best-fit coating layer thickness only changes by a few nanometers when using these different refractive index equations. The retardance error changes magnitude slightly, with larger errors at the extreme wavelength ends of the data set. We can clearly see spectral oscillations in retardance error of 1.5-deg peak to peak. In essence, both two-layer models are incomplete at reproducing the measured spectral complexity at levels below ± 1 deg retardance. This ± 1 deg retardance error is orders of magnitude above our NLSP metrology statistical noise limits and indicates the limitations of the simple two-layer thickness fitting technique. With NLSP, our data are now of sufficient quality that we must add more variables to include variable refractive index dependence on wavelength, the metal refractive index values, and to also include reflectivity and diattenuation in the fitting metric. However, this model is sufficient for estimating the DKIST system calibration behavior and for showing how real coatings may impact DKIST polarization models.

The materials deposited and their refractive indices upon deposition are one of the major limitations to this modeling. When we have vendor-provided refractive index data or can adjust the refractive index wavelength interpolation, we achieve significantly better fits. Figure 8 shows measurements and associated retardance fits to three enhanced protected silver mirror samples from IOI. The mirrors represent different coating formulas, materials, and design choices.

The default materials and refractive we used in fitting the DKIST mirrors above are provided in standard software packages such as the Thin Film Calculator (TFCalc), Zemax optical design studio, or in text books such as McCall, Hodgkinson, and Wu (MHW).¹⁵ With vendor-provided refractive index data and coating designs (in TFCalc files or as Zemax coating recipes), we follow the same coating layer thickness fit to match the retardance values. We then revise the model to use the as-built thicknesses to show the diattenuation prediction. We did not revise the refractive index of the dielectric materials or the silver or allow any variation of material refractive index. As shown above, the diattenuation is very sensitive to the complex refractive index of the silver coating and so we do not expect good fits for these parameters.

The green lines in Fig. 8 show the NLSP data. Left shows retardance and right shows diattenuation. Most retardance curves in green are nearly invisible as the model fits nearly perfectly overlay the retardance data set. For diattenuation, NLSP measures the IQ and QI elements of the Mueller matrix independently, so both are shown to demonstrate systematic and statistical error limits. The blue curves show our Python-script calculations using the Berreman calculus when using the vendor-provided refractive indices where given, and nominal TFCalc values otherwise. Typical fits are now within 0.5-deg retardance error peak to peak and a much smaller RMS for the IOI samples. The fit was significantly worse for the DKIST EAg sample shown above in Figs. 6 and 7. This mismatch is likely caused by both varying refractive indices of coating materials and additional coating layers not included in our fit as we have no vendor information on this coating. We can clearly see an artifact in the NLSP data set around 680-nm wavelength corresponding to a 0.5-deg narrow spike. Our fits also fail significantly at shorter wavelengths (where the refractive index interpolations are worse).

With the TFCalc model revisions to the dielectric thicknesses, we can also compare NLSP diattenuation measurements to various theoretical calculations. In the right-hand graphics of Fig. 8 we show the diattenuation and a measurement provided by IOI in the upper right. The IOI diattenuation measurements shown in dashed black are recorded with orthogonal polarizers in their Shimadzu spectrophotometer to measure reflectivity of S and P polarization states.

The TFCalc silver default refractive index values are used in this dashed black line. The fits are generally within 0.5% diattenuation but with high spectral variation in the quality of the fit. We ran another Berreman model using the MHW¹⁵ refractive index for silver to demonstrate the impact of a change in assumed metal optical properties. This alternate model matches the data better at different wavelengths. We note the MHW indices are only fit across visible wavelengths and are only plotted where the material properties are valid. As metallic coatings deposited in coating chambers can have variation in properties with deposition, a mismatch between literature values and actual as-coated data is expected.

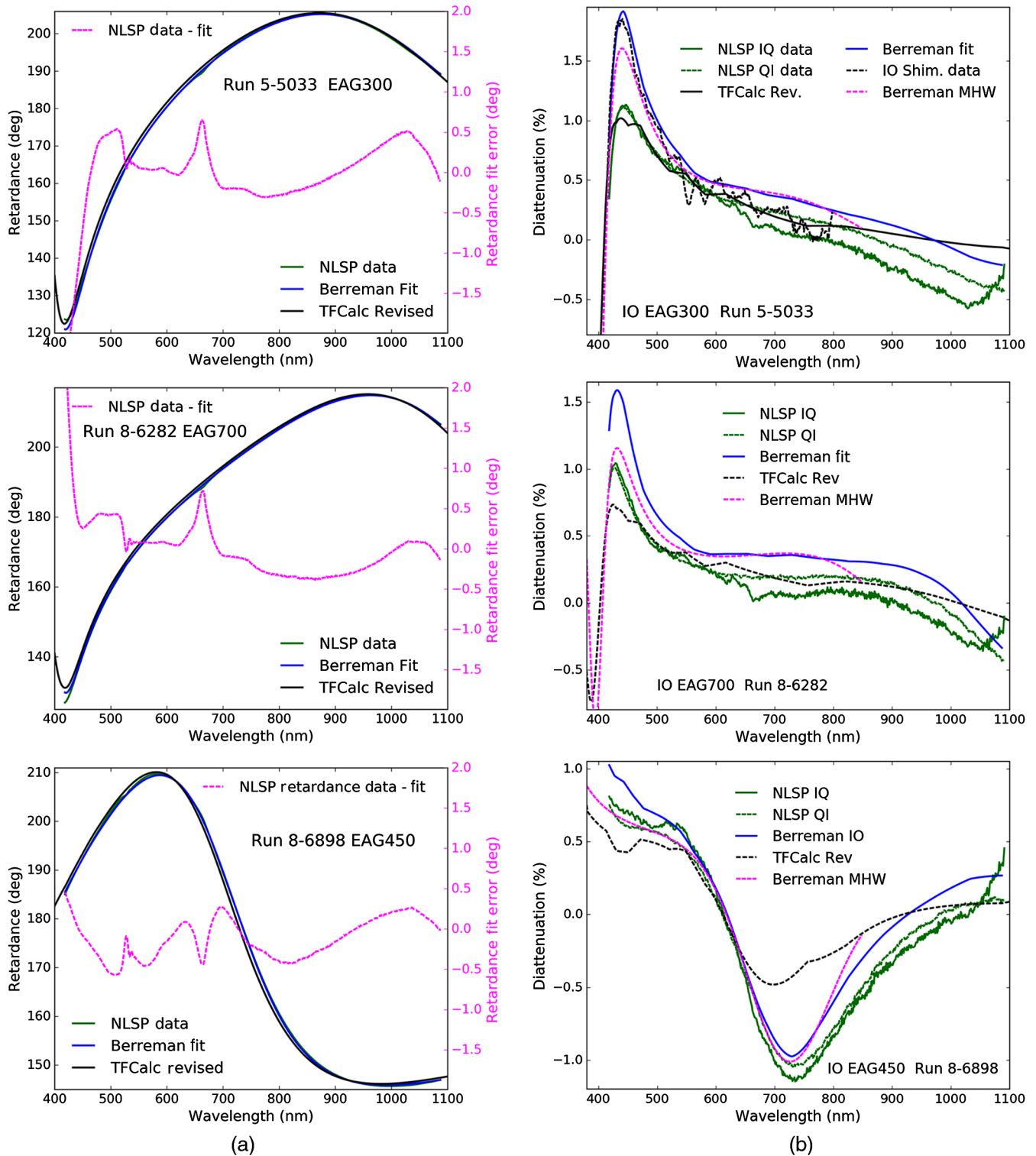


Fig. 8 A comparison of (a) retardance and (b) diattenuation data and models. Each panel has the NLSP data recorded with the IOI mirror sample in reflection at 45-deg incidence shown in green. For the diattenuation data, we have two independent estimates of diattenuation from both the QI and the IQ elements of the NLSP-measured Mueller matrix. The best-fit Berreman model is found via a simple search for dielectric thicknesses in a grid with 1-nm step size. The best-fit Berreman model (to retardance only) is plotted in each panel in blue. The difference in retardance between the NLSP data and the best-fit Berreman model is shown in magenta using the right-hand y-axis of (a). The Berreman model reproduces the data to roughly ± 2 deg in retardance with a very repeatable mismatch function with wavelength. (a) Show agreement between data and models to roughly fraction of a percentage magnitudes, though diattenuation is not included in the fit. The dashed magenta line in the right-hand diattenuation plots shows the model using an alternate refractive index for the silver from MHW.¹⁵ An IOI diattenuation spectra from their Shimadzu system is shown by the dashed black line in the upper right graph.

Table 3 Indices.

Material	Index
ZnS	2.31
TiO ₂ ^t	2.31
TiO ₂ ^b	2.18
TiO ₂	2.04
HfO ₂	1.98
SiO	1.92
Al ₂ O ₃ ^b	1.67
Al ₂ O ₃	1.55
SiO ₂	1.45
MgF ₂	1.37

3.1 Refractive Indices, Materials Parameters, and Coating Model Interpretation

The refractive index values used in various software modeling packages vary. In common software packages such as TFCalc or Zemax, the basic software package provides some default materials and refractive index values as lookup tables or simple equations. This nominal is useful from a modeling perspective as it provides rough guides to actual coating materials. However, there are several factors that impact the actual refractive index of deposited materials in the coating process. These include the coating deposition process, temperature, final material density, varying growth styles, impurity concentrations, and others. Thus, detailed information is required from a vendor about their specific materials and known process before having confidence in modeling coatings using refractive index data. In most cases, we do not need to know and likely will not be told the actual materials and all the proprietary details of a coating. However,

a useful performance model for mirror properties can be created using simple parametric curves from the public materials data as representative of common coating types. We do not need to know specific coating formulation details to estimate the polarization performance of the system. As a modeling approach for this paper, we simply assume that the refractive index formulas may change substantially, in some cases over 15%. We list examples in Table 3 for a wavelength of 850 nm drawn from TFCalc, Zemax, MHW,¹⁵ and other references. The superscript “b” denotes the Boidin reference and the “t” denotes the TFCalc default. For instance, crystal TiO₂ would have an index of 2.3, while in some coating literature the index is in the range 2.0 to 2.2. Thus, a refractive index curve fit in our study is not indicative of an actual material but of an effective refractive index that may be similar to materials commonly used in the coating process.

Figure 9 shows example curves taken from a common website (RefractiveIndex.info), the default coating file in the software packages TFCalc and Zemax, along with vendor catalog values. On the left side we can see crystal sapphire (Al₂O₃) having an index around 1.75. When used in a coating, TFCalc gives a value slightly above 1.6 constant for all wavelengths as the dashed red curve, while Zemax uses a value slightly below 1.6 that falls with wavelength as the dashed magenta curve. The website RefractiveIndex.info cites Boidin et al.⁶⁸ in the red curve from just above 1.7 falling to 1.65 at long wavelengths. We have internal DKIST engineering reports that also use slightly higher and lower values as seen by the green and purple curves.

Slightly better agreement is seen between values for a common coating material, MgF₂. The right-hand graphic of Fig. 9 shows the CVI Laser Optics & Melles Griot catalog equation for crystalline MgF₂ as the solid and dashed magenta lines. The magenta dot-dashed line represents the weighted average of an amorphous version simply computed as twice the ordinary and once the extraordinary equations combined. Zemax provides a point-wise linearly interpolated version seen as the dashed blue line in Fig. 9 that essentially tracks the CVI catalog equation for the ordinary index of crystal MgF₂. The TFCalc software package uses a wavelength independent value of 1.38.

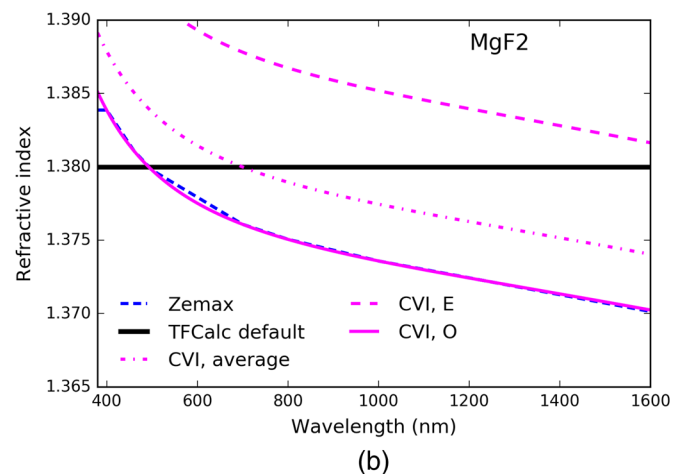
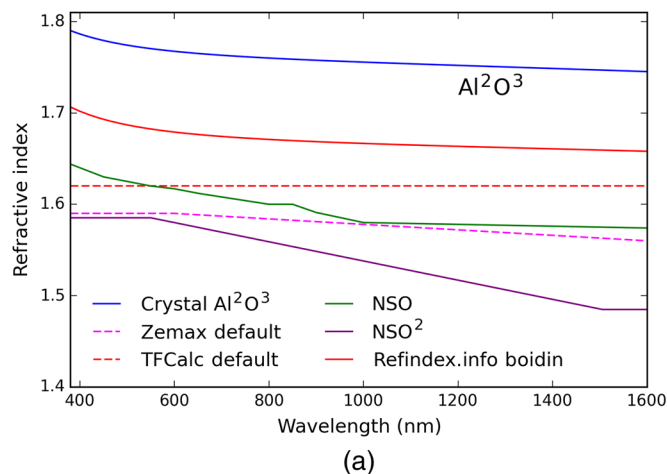


Fig. 9 The refractive indices published for common coating materials. The RefractiveIndex.info website data are shown along with data from the Zemax coating file provided with version 16.5, 2016 and the TFCalc default material files where applicable. (a) Shows Al₂O₃ and (b) shows MgF₂ crystal and coating values. The CVI Melles Griot catalog equation is used for crystal MgF₂. The difference in refractive index between amorphous coated materials and crystalline materials can be several percent, giving strong changes in predicted coating performance.

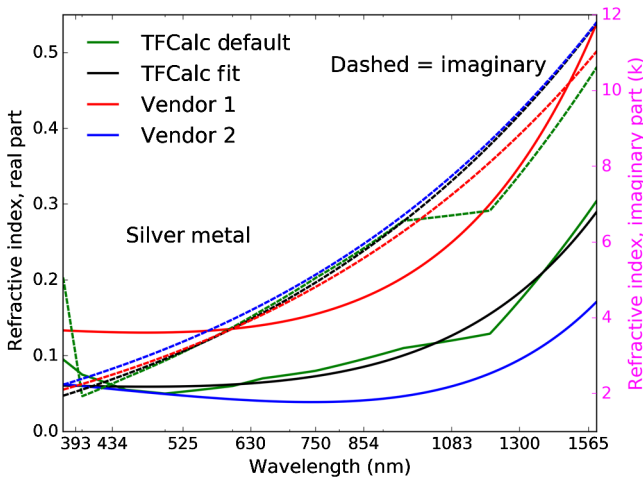


Fig. 10 The real and imaginary refractive index components of silver. The real component (n) is shown as the solid lines on the left-hand y axis with values ranging from 0.05 to 0.5. The green lines show the default TFCalc refractive indices. Note some discontinuities at 400- and 1000-nm wavelengths. Different colors show simple polynomial model fits to TFCalc default values and models provided by vendors in various example coatings. The dashed lines show the imaginary component (k) in exponential form ($n-ki$) on the right-hand y axis. The values of k reflect orders of magnitude change in the wave penetration depth into the metal.

The refractive index of the silver metal has a strong influence on polarization properties of the coatings. Literature and vendor values vary widely. Figure 10 shows an example of linearly interpolated TFCalc default values in green with limited data points and some strong changes in spectral behavior around 400- and 1000-nm wavelength. We also show simple functional fits to the real and imaginary components of silver metal used in various coating models. The solid lines show simple polynomial models for the real part of the refractive index (n) with values ranging from 0.05 to 0.5.

The imaginary part (k) is shown as dashed lines in Fig. 10 using a Zemax-style convention where the index is modeled as ($n-ki$). This imaginary index is exponential in behavior and the electromagnetic wave does not penetrate more than a few nanometers into the metal layer when the complex index is >2 or 3 . For the silver metal coating model in Fig. 10, we see values of roughly 3 at blue wavelengths rising linearly to 11 or 12 at wavelengths of 1600 nm. Often the vendor curves are discontinuous as the green line of Fig. 10 shows for the default TFCalc values.

In prior works,^{11,67} we only allowed the thickness of one or two dielectric coating layers to vary as a simple two variable optimization problem. However, the metal layer thickness and refractive index both have large polarimetric impact. We show retardance and diattenuation changes in Fig. 11 when using two different formulations for the silver metal indices. In both models we use 10 nm of ZnS with indices from RefractiveIndex.info coated over 105 nm of Al₂O₃ with refractive indices using the Boidin et al.⁶⁸ values in RefractiveIndex.info. We change only the refractive index of the silver to show the impact.

The black curve with the left-hand Y axis shows that retardance can change by over 2-deg peak to peak for a coating with 20 deg to 40 deg, a 10% effect. Much larger changes are seen in diattenuation. The diattenuation change shown in blue using the right-hand Y axis is up to 4% at short wavelengths and roughly half a percent in the visible-to-NIR wavelengths. The

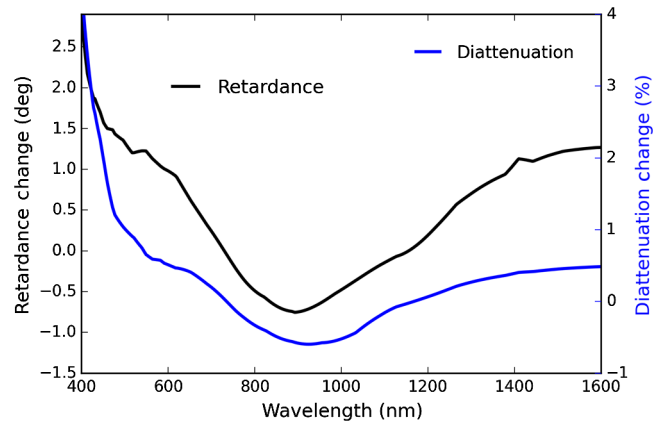


Fig. 11 The difference between retardance and diattenuation parameters computed using two different refractive index values for silver metal in the coating for a reflection off a DKIST-enhanced protected silver mirror formula at 45-deg incidence.

diattenuation for this coating is only 1.5% magnitude peak to peak. This metal index difference changes the diattenuation over 300%. The silver metal properties can dominate the fit of diattenuation. Vendors sometimes provide coating performance predictions. Infrequently, this may be accompanied by names of materials used, such as coating X is SiO₂ protecting the Ag. Usually, the layer thickness is not disclosed and the refractive index values for the as-coated material differ significantly from literature values. The retardance is much more sensitive to the dielectric material thicknesses as well as refractive indices. The diattenuation is very sensitive to the real and imaginary refractive index components of the metal as well as the dielectrics.

In Fig. 12, we show the reflectance predicted for this same coating model but we use a few different variations of the silver metal complex refractive index. The reflectivity data show clear discontinuities where TFCalc, as well as our Berreman code, performs a linear interpolation between points in a table of refractive index values. Solid lines shows the S-polarization

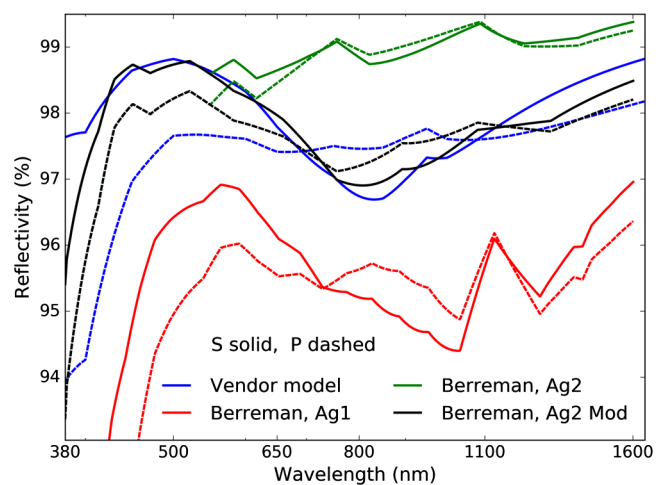


Fig. 12 The reflectivity variation when linearly interpolating tabulated data for refractive index of the silver metal layer. The dashed lines show parallel polarization state (P), while the solid lines show the perpendicular polarization state (S) at a 45-deg incidence angle. Blue shows a vendor prediction, while black, red, and green show Berreman models using various refractive index curves. Discontinuities come from interpolation between refractive index table values.

state, while dashed lines show the P-polarization state. This particular coating has diattenuation change sign in the 700- to 1050-nm wavelength range. The blue curve shows a vendor-provided TFCalc model. The vendors may have their own internal materials databases, sometimes where refractive indices are adjusted to their results or at other times modified versions of literature values. We expect significant variation among any historical literature values, the vendor models, and actual coatings. This is especially true when our simple models likely do not correspond to actual materials and may not include all the layers in the actual coating. The green curve shows one of our Berreman models of silver refractive indices that overestimates the reflectivity at NIR wavelengths by 1.5%. The red curve shows a separate Berreman prediction using lower real refractive index components for the silver that underestimates the reflectivity by over 2%. The black curve is a by-hand modification of the green curve at infrared wavelengths to show that reflectivity can be met, but the diattenuation prediction is still significantly in error. The various lookup tables of silver refractive indices presented can change the reflectivity by over 3%. As we currently do not perform a simultaneous fit to reflectivity, diattenuation, and retardance, we expect our models to contain errors as presented in this section. This becomes a major limitation of polarization performance modeling, requiring future development for simultaneous fitting of many variables.

3.2 DKIST ViSP: Enhanced Protected Silver Mirrors with 29 Dielectric Layers

We show in this section a significantly more complex enhanced silver mirror coating that was nominally going to be used in DKIST by one of our partner instruments. The ViSP team chose to use a many-layered enhancement on the feed mirrors between the FIDO dichroics and their modulating retarder after the spectrograph entrance slit. This coating is nominally 29 layers of dielectric with an oscillating high-low refractive index design. This represents roughly $3\ \mu\text{m}$ of dielectric coated on top of the silver metal layer. Given the many layers, significant spectral variation is expected along with the presence of narrow spectral

features. Though the team has stripped and recoated their mirrors with an alternate coating, we include this coating metrology here to show the impact of many-layered enhanced designs and consideration of manufacturing issues.

Figure 13 shows the ViSP mirror witness sample polarization properties measured in NLSP at 45-deg incidence. The left-hand graphic shows retardance in black and diattenuation in blue for the full NLSP measurement range. The right-hand graphic shows the shorter visible wavelengths where very rapid but well-measured spectral changes are seen. The retardance changes by over 300 deg in 20-nm wavelength range, giving a spectral gradient up to 60 deg per 1-nm wavelength. This bandpass is comparable to the full spectral range measured across the ViSP sensors. Diattenuation similarly changes from -10% to $+20\%$ in a very narrow bandpass. This kind of mirror coating has impact for DKIST as the modulation matrix must be wavelength-dependent with the assumption of variation at these magnitudes. We note that requirements against strong spectral gradient in retardance and diattenuation are not included in any specifications. Given the metrology results, the ViSP team has already stripped and recoated their mirrors. Behavior for the ViSP feed optics had they kept these coatings will be explored in later sections of this paper. This case is a good example of what happens when many-layered coatings are specified giving rise to complex, large, and spectrally narrow polarization properties.

3.3 Summary of Coating Model Fits to Reflectivity, Diattenuation, and Retardance

We have presented examples of two-layer coating models fit to NLSP retardance measurements in this section. We have shown how the dielectric layer thickness and material refractive index impacts fitting measured retardance curves. In Sec. 3.1, we have shown how the complex refractive index of the metal layer strongly influences the reflectivity and diattenuation. When fitting a coating formula to measured data, the refractive indices of all components need to be assessed. For DKIST, the retardance values are critical as they determine the field dependence of the cross talk and ultimately drive requirements on how DKIST

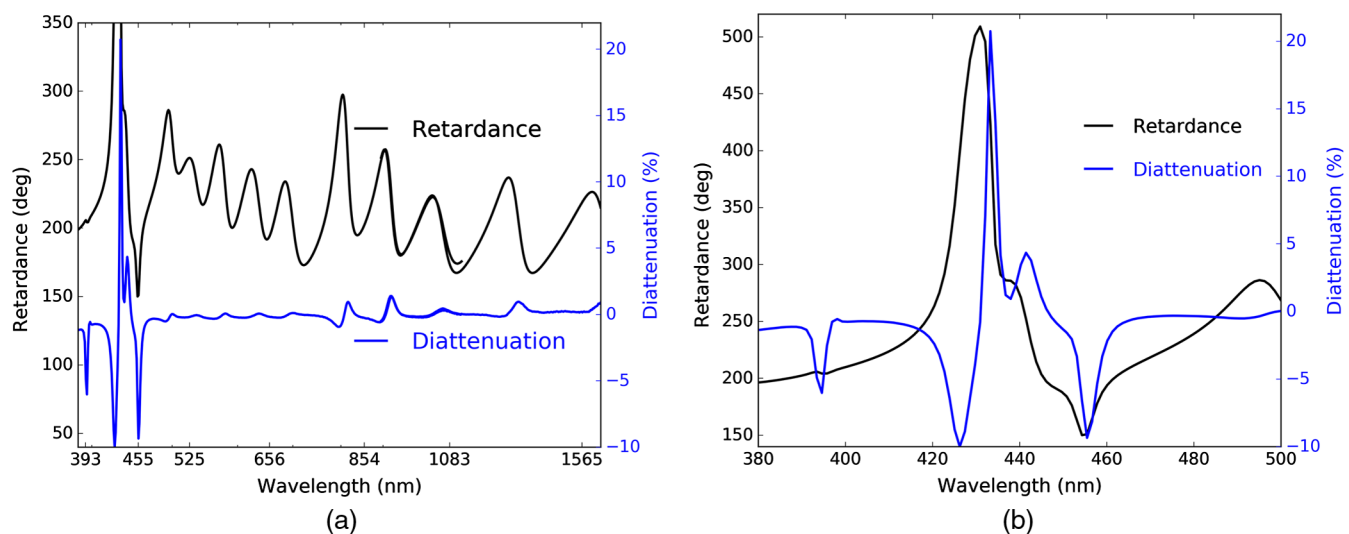


Fig. 13 Retardance in black and diattenuation in blue measured with NLSP for the ViSP feed mirrors coating witness sample at 45-deg incidence. (a) Shows all NLSP wavelengths from 380 to 1650 nm. (b) Shows the 380- to 520-nm wavelength range where the mirrors show a very strong change in retardance of almost a complete wave over 20-nm bandpass.

calibrates instruments and with what model for the mirror retardance. When attempting to fit retardance, diattenuation, and reflectivity simultaneously, all refractive index values become critical. In Sec. 3.1, we have shown how public literature values for refractive indices may roughly approximate coating behavior, but a detailed fit to high accuracy in all performance parameters requires substantially more detailed knowledge of the coating materials properties. Examples of coating model fits and witness sample measurements were provided for three IOI samples where we have much better refractive index information. Measurements of polarization for a more complex mirror coating with 29 dielectric layers over silver initially planned for use in the DKIST ViSP have been shown in Sec. 3.2. In Sec. 10, we show more examples of mirror polarization properties from commercial sources used in DKIST and the GST (formerly the NST) at the BBSO, along with examples of coating models and refractive index variation impacts on predicted behavior. We have samples from the GREGOR solar telescope and DKIST VTF instrument shown in Sec. 10.1. We move on from many-layered dielectric protected mirrors to many-layered dielectric coatings used as antireflection coatings in Secs. 4 and 5. Techniques for fitting properties of such coatings also become more complex.

4 WBBAR1 for DKIST WFS-BS1, FIDO, and Calibration Optics

Antireflection coatings applied to various windows and beam splitters have potential for polarization impact on the DKIST optical train. The nominal suite of visible-light instruments fed by the AO system and dichroics includes paths with between one and four beam splitter transmissions. The behavior of any antireflection coating will thus be multiplied by one to more than five surfaces. As these optics must cover our entire instrument suite, the wavelength range and performance requirements are stringent.

IOI designed a wide wavelength range antireflection coating to cover the 380- to 1800-nm wavelength region. The nominal design includes a thin strippable layer, then 14 layers oscillating between SiO₂ and HfO₂ of roughly 350 nm total physical thickness for each material at very roughly 50 nm per layer. The final outer layer is roughly 130 nm of MgF₂. The coating has 0.86 μm total physical thickness and 16 layers. We call this coating WBBAR1. Several tests to date are listed in Table 4 showing chamber and run number along with the optic coated. This

Table 4 WBBAR1 samples.

Run	Description
7-4246	Prelim test
10-0095	Final test
12-6267	PA&C win S1
12-6268	PA&C win S2
67 & 67	Infrasil S1 and S2
10-0231	WFC-BS1 test
10-0233	WFC-BS1

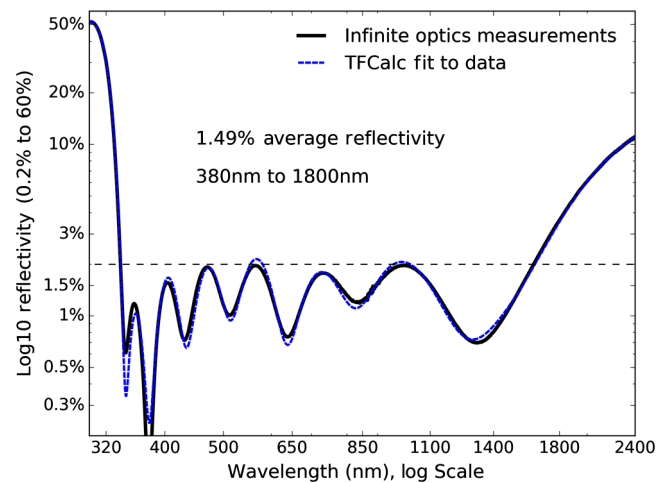


Fig. 14 The Infinite Optics broadband antireflection coating on a Heraeus Infrasil 301 fused silica substrate. Black shows spectrophotometric measurements from Infinite Optics in unpolarized light. The dashed blue curve shows a TFCalc model where all layers are adjusted in thickness to fit the transmission model to the measurements. An incidence angle of 8 deg is used in the model and for the data collection.

WBBAR1 formula is essentially a dichroic coating with high UV reflectance and good visible-to-NIR transmission. We also have a slightly modified design optimized for the 620- to 1800-nm wavelength range called WBBAR2 that will be used on some of the dichroics, which are described later, that work in transmission only at longer wavelength ranges. All instruments post AO are fed in transmission through the WFS beam splitter WFS-BS1 at 15-deg incidence angle. The wedged FIDO dichroic beam splitters also have an antireflection coating on the back surfaces.

Using TFCalc, we can adjust the individual layer thicknesses to fit the spectrophotometric data, allowing us to create an as-built coating design. Figure 14 shows an example. The black curve shows spectrophotometry from Infinite Optics on a coating test run. The baseline TFCalc design model includes four thin layers that are important to achieve performance but increase the design sensitivity to manufacturing tolerances. The dashed blue curve shows a best-fit TFCalc model to the as-built spectrophotometric measurements. Note that in this model we have used refractive index data provided by Infinite Optics. Only the material thickness was allowed to vary in the fit and not the refractive index data for each material.

The TFCalc polarization predictions are compared to NLSP measurements in Fig. 15. The sample from chamber 10, run 0095, is measured with NLSP in transmission through a fused silica witness sample at 0 deg, 15 deg, 30 deg, and 45 deg incidence angle. The retardance data are shown on the left, while diattenuation data are seen on the right. The retardance data are smooth with magnitudes of <1 deg at 15 deg incidence angles, as will be used in the DKIST optics WFS-BS1 and the FIDO beam splitters. This retardance is nearly negligible. Similarly, the diattenuation is <0.6% at 15-deg incidence angles. In the diattenuation data, the step in the measurements occurs when data between the visible (VIS) and near-infrared (NIR) spectrographs is spliced together at 1020-nm wavelength. For the diattenuation data set, we had to account for the additional diattenuation of the Fresnel reflection off the uncoated back surface of the substrate. This adds roughly 4.5% diattenuation at 45-deg incidence angle.

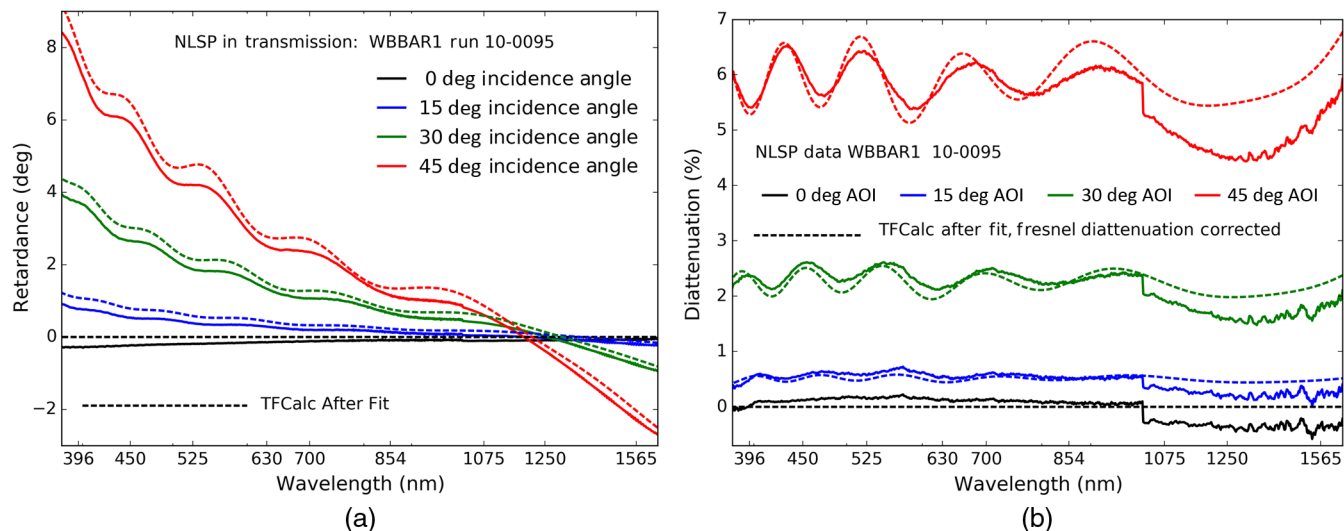


Fig. 15 (a) Transmission retardance and (b) diattenuation of Infinite Optics WBBAR1 sample 10-0095. Measurements are solid lines and are compared to TFCalc model predictions as dashed lines. TFCalc models are created from the nominal design file modified by fitting the IOI unpolarized transmission spectrum at AOI = 8 deg.

4.1 Antireflection and Dichroic Summary: Fitting Many-Layered TFCalc Models

In this section we show how simple antireflection coating designs can be adjusted to fit the as-built layer thicknesses by using unpolarized transmission spectra. With these adjusted models, we are able to then predict transmission, diattenuation, and retardance that closely match our NLSP measurements and vendor metrology. A wide-wavelength range antireflection coating design with 14 layers of SiO₂ and HfO₂ and two additional layers (top and bottom) is fit to unpolarized transmission data. Subsequent predictions are made for NLSP retardance and diattenuation with agreement better than 1-deg retardance and a fraction of a percent diattenuation. Errors increased with higher incidence angles due to the exacerbated optical misalignments in NLSP caused by the tilted glass substrate. In Sec. 11, we show coating repeatability and measurements of one-side and two-side coated samples. These samples are identical in coating design to three DKIST windows within FIDO called Coudé Windows 1, 2, and 3 (e.g., denoted as C-W1). The AO wavefront beam splitter (WFS-BS1) is only back-side coated with WBBAR1 with FIDO C-W2 being delivered similarly. The FIDO C-W1 and C-W3 will be both-side coated similar to the two-side coated windows in the DKIST calibration optic (CalPol2 window). Now that we have successfully shown this example of repeatably manufacturing and fitting relatively simple, thin coatings in transmission, we move on to the much thicker FIDO dichroic coatings working both in transmission and in reflection.

5 Dichroic Coatings: Polarization Performance and Fido Designs

The FIDO contains a set of interchangeable mirrors, dichroic beam splitters, and windows that is used to send various wavelengths to the suite of DKIST post-AO coudé instruments. The optics is mounted in the collimated beam after the AO system and requires a 290-mm clear aperture to accommodate the diverging 2.83 arc min field of view at station CL4 with a tolerance.

The optics can cause noncommon path wavefront errors as they are mounted in a collimated beam after the WFS and near a pupil. The wavefront qualities are critical to delivering diffraction-limited performance for each instrument and stress from coatings is a major design consideration. The substrates are Heraeus Infrasil 302 at 43-mm thickness.

The optical specifications are quite demanding with significant impact on the allowable coatings. Table 5 shows some of the highlights. These are large parts that must be interchangeable without disturbing other optics. As such, the wavefront error in both transmission and reflection must be incredibly flat after coating, including power in the transmitted wavefront. Stress in the coating must be compensated by predishing the Infrasil substrates, so coatings must be both low stress and repeatable in stress and WFE to ensure that each dichroic beam splitter is interchangeable. The wedge angle of each substrate must also be identical to better than 1arc sec for a wedge of half degree. As most coatings are highly reflective at 633 nm, testing must be done for transmission at long wavelengths. The guaranteed intrinsic stress birefringence of <5 nm per cm of optical path at 633-nm wavelength ensures that there is minimal variable

Table 5 Dichroic specs.

Clear aperture 290 mm
Angle of Incidence 15 deg
Coating thk. ±1% spatial var.
Diattenuation <2%
Wedge angle 0.5 deg ±1 arc sec
10.5-nm RMS refl WFE, pwr rem
48-nm RMS refl WFE power
7.5-nm RMS trans WFE

Table 6 Dichroic samples.

Name	Lyr	Thk (μm)	Run number
C-BS-465	25	1.5	TBD
WBBAR1	16	0.9	TBD
C-BS-555	48	3.1	TBD
WBBAR1	16	0.9	TBD
C-BS-643	52	3.5	TBD
WBBAR2	10	0.8	TBD
C-BS-680	52	3.8	TBD
WBBAR2	10	0.8	TBD
C-BS-950	96	8.8	TBD
WBBAR2	10	0.8	TBD
Dich. A	61	4.1	8-5652
Dich. B	84	6.9	7-2802
Dich. C	21	1.0	lpw1-400

wavefront error and retardance. As the optics is near a pupil plane, birefringence will spatially average significantly and the resulting mild depolarization is not a concern.

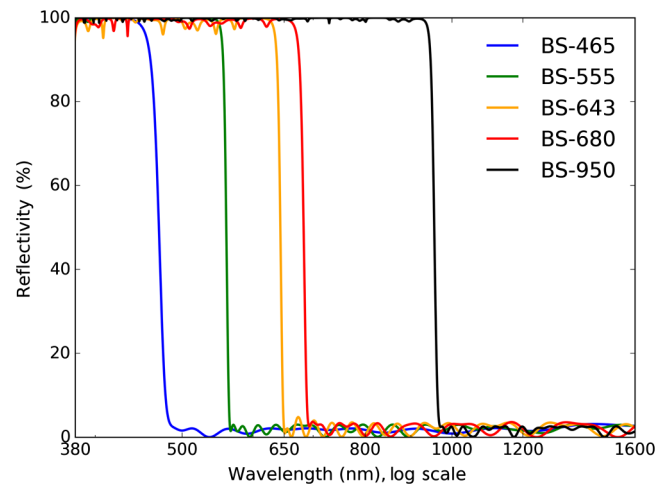
The optics is at 15-deg incidence angle which does create polarization through the complex dichroic coatings on the front surfaces and also the broadband antireflection coatings on the back surfaces. We modeled polarization fringes in two recent papers^{13,69} and do not expect to observe significant fringing, given the 0.5 deg wedge angle in each of the FIDO beam splitters.

There are presently five dichroics planned for fabrication, as shown in Table 6. The naming convention denotes the wavelength where the beam splitter switches from reflective to transmissive with a 50% value. As an example, the Coudé Beam Splitter reflecting wavelengths short of 465 nm while transmitting wavelengths longer than 465 nm is denoted as C-BS-465. The dichroic suite is thus 465, 555, 643, 680, and 950. We also show the appropriate antireflection coating intended for the back surface in Table 6. This will either be WBBAR1 described above or the related coating WBBAR2.

We are in the process of verifying the coating performance, repeatability, spatial uniformity, stress, and wavefront error so we list TBD in Table 6. We also list three dichroic samples used in early evaluation and design from Infinite Optics that we label Dichroics A, B, and C.

We show example reflectivity curves of the planned dichroic coatings at 15-deg incidence angle in Fig. 16. The designs have fairly sharp transitions with most coatings switching from 80% reflective to 80% transmissive in <10-nm wavelength. We chose this style of coating as they are low-stress evaporative coatings with reasonable repeatability and achievable 1% physical thickness uniformity across the entire aperture.

The retardance of the reflected beam at 15-deg incidence angle is shown in the right-hand graphic of Fig. 17. The thickest coating is C-BS-950 with 96 layers and an 8.8 μm physical

**Fig. 16** Design reflectivity for the FIDO optics.

thickness. There are strong spectral variations expected in retardance curves for dichroics with tens of layers. The theoretical retardance derivative has several bandpasses with gradients of 10 deg per nanometer wavelength with a few specific narrow features up to magnitudes of 100-deg retardance per nanometer wavelength. We show in this section that these rapid swings in retardance are observable and can also be mitigated by design. Similarly, these narrow spectral features in dichroic coatings are also coincident with significant diattenuation as well as strong changes in transmission. All of these narrow spectral features of dichroics have impact for DKIST calibration, as we can possibly anticipate strong spectral changes across the $\sim\text{nm}$ instrument bandpasses in the modulation matrix through retardance and diattenuation, in addition to substantial throughput changes. Through designing coatings with minimal diattenuation, we have been able to achieve retardance values as in Fig. 17 without many waves wrapping and excessively sharp spectral features.

Though the retardance curves appear to have many spikes, there are no multiple-wave wrapping wavelengths, reflectivity is above 96% for all wavelengths in the reflection band, and the reflected diattenuation values are all below 2% for any wavelength in reflection. We show diattenuation for the reflected beam in each design in the left-hand graphic of Fig. 17. Values are always well below 2% magnitude though there are some narrow spectral features that are sensitive to coating manufacturing tolerances.

The FIDO beam splitter coating designs are currently undergoing a significant uniformity, stress, and polarization testing processes. As part of the DKIST systems engineering, we need to verify the spectral predictions of TFCalc against polarization measurements for various coating samples simultaneous with repeatability of coating stress, wavefront error, and other relevant performance parameters. Here we present testing of Infinite Optics dichroic samples as well as some preliminary design predictions for DKIST.

5.1 FIDO Dichroic C-BS-465: Coating Spatial Uniformity and Model Fitting

In this section, we make a detailed analysis of the thinnest FIDO dichroic coating. We assess two separate coating shots for spatial uniformity, spectral performance, and variability of the individual coating layers. This BS-465 design uses 24 layers,

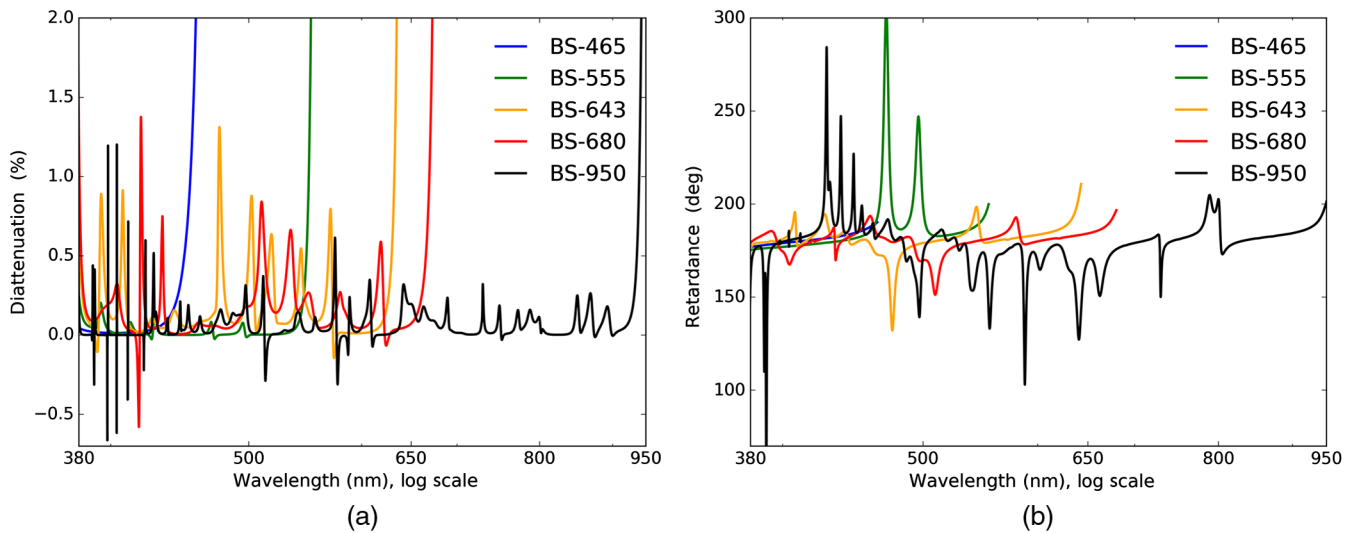


Fig. 17 (a) The diattenuation and (b) retardance for the FIDO optics from the TFCalc design for the beam reflected at 15-deg incidence angle. Designs were constrained to have diattenuation below 2%.

Table 7 Dichroic coating 465 testing.

Name	Run	Meas
Test1	10-0150	S&P 15 deg, Unif 0 deg 9 samp.
Test2	10-0153	S&P 15 deg, Unif 0 deg 9 samp.
Filter1	10-0154	%T 0 deg Design: (HL) ³ 2H (LH) ³
Filter2	10-0156	%T 0 deg Design: (HL) ³ 2H (LH) ³

has a 1502-nm physical thickness with the thinnest layer at 17.0 nm in the design. The coating follows a common design with a strippable layer as the base then alternating SiO₂ and TiO₂ layers. A thicker SiO₂ outer layer is the air interface.

Table 7 shows the test runs for this dichroic coating. We received uniformity measurements at 15-deg incidence angle on nine samples coated in run 10-0153 around April 21, 2018. The transmission and reflection measured by IOI with their spectrograph is shown in the left-hand graphic of Fig. 18 as the solid lines. We then used this spectral data and selected wavelengths from 350 to 1200 nm to perform coating model fitting in TFCalc.

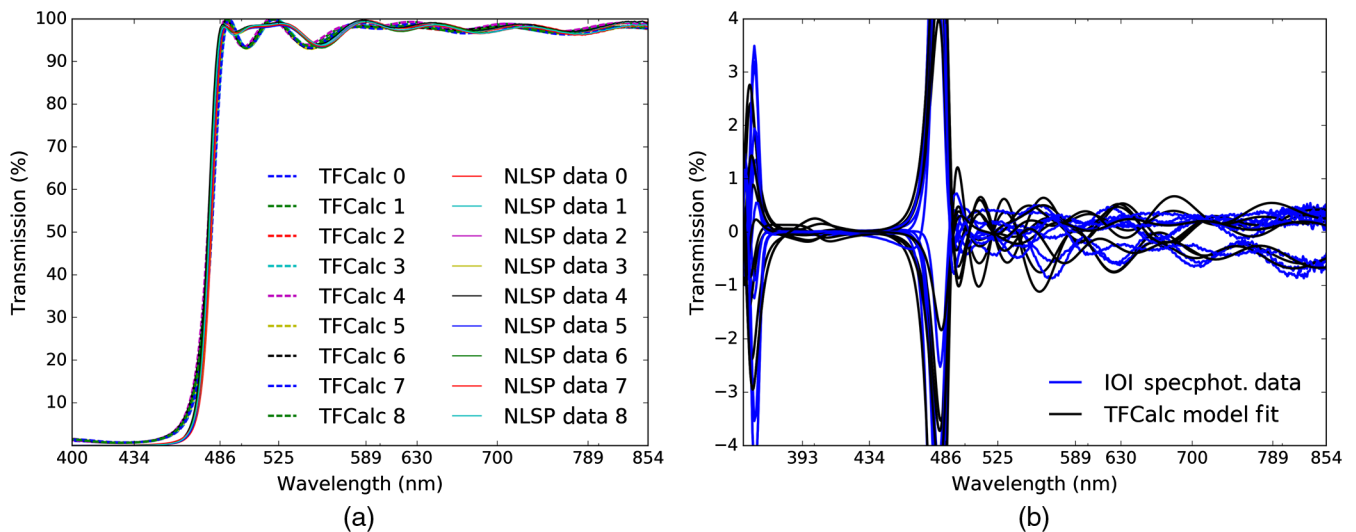


Fig. 18 (a) Shows TFCalc models after fitting the IOI measurements, along with the uniformity sample measurements. (b) Shows the differences between the average and each individual curve to highlight spatial variation. Blue shows spatial variation in measurements, while black shows spatial variation derived from the TFCalc models. Dichroic 465 test run 10-1053 had transmission measured on nine witness samples at AOI = 0 deg. Transmission curves are adjusted for a theoretical ~3.8% reflection loss from the uncoated sample back surface.

After this uniformity testing, additional tests of the chamber for spatial uniformity and refractive index of the deposited materials were done. The tests used a standard 13-layer narrow band filter design (HL)³ 2H (LH)³. Table 7 shows these two tests in the same chamber (10) but with coating shot 0154 immediately after the dichroic and another test 6 days later in shot 0156. With the nominal wavelength set around 480 nm for this test, the quarter-wave optical thickness is 82 nm for the low-index material SiO₂ and 55 nm for the high-index material TiO₂. The variance of the filter central wavelength was used as a statistical measure of the layer-by-layer variation, showing that we did indeed pass a 1% variation of the physical thickness across the aperture. With these updated refractive indices in hand, we could fit the TFCalc models to the C-BS-465 dichroic sample data. The left-hand graphic of Fig. 18 shows the best-fit TFCalc models as dashed lines. Some of the spectral oscillations are not well fit, but the transition wavelengths and general behavior are reproduced. We can expect spatial variation in both reflection and transmission across the beam following the magnitudes shown in Fig. 18.

The right-hand graphic of Fig. 18 shows the variation between the mean and the nine individual spatial samples. The TFCalc model variation is shown in black and measurement residual errors are shown in blue. As expected, there are larger errors near wavelengths where spectral gradients are strongest. We also do not reproduce a somewhat larger spectral oscillation around 475-nm wavelength with a depth of a few percent. Note that we have adjusted the transmission to account for the ~3.8% Fresnel reflection loss from the uncoated sample back surface using the Fresnel equations and the refractive index data for Heraeus Infrasil provided by the manufacturer.

The statistics of layer variation in these coatings show that we pass a 1% physical coating thickness variation across the clear aperture, and that the variations essentially follow Gaussian statistics across the aperture. In the left-hand graphic of Fig. 19, we show the variation between layers in the TFCalc fitting process. The baseline design thickness is shown as the blue curve with each layer of alternating SiO₂ and TiO₂ having

thicknesses between roughly 30 and 80 nm. Each of the nine colored curves shows a fit to the individual spectra.

In the right-hand graphic of Fig. 19, we show the statistics of the variation between layers. The cumulative distribution of errors in each individual layer against the nominal design is shown as the solid black line. We did not see any evidence of any layer being particularly thicker or thinner as a function of aperture radius or layer depth. A few layers show more variation than others, but the statistics are essentially the same as other layers with radius and depth. The crosses show 1-sigma 68% and 2-sigma 95% errors for a Gaussian distribution fit to the histogram. More than 68% of the layers are within 1.15-nm layer thickness of the average. For 95% of the points, the layer variation is <2.9 nm.

Figure 20 shows the transmission and reflection data in the appropriate bandpass intended for feeding the DKIST instruments. Reflectivity is over 99% for the range 380 to 450 nm. Similarly, after compensating for the Fresnel reflection, the transmission is over 96% for all wavelengths between 480 nm and the long wavelength cutoff of the metrology, except for a small bandpass around 550 nm. The mean transmission is over 97% for this coating. The actual FIDO dichroic will have the WBBAR1 coating on the back side, minimizing the back surface reflection losses.

Figure 21 shows the IOI transmission data around the transition wavelength at normal incidence (0 deg) corrected for the back surface Fresnel losses. The transition wavelength between reflection and transmission is slightly longer than the nominal 50% transmission at 465-nm wavelength. For this design there is also roughly 5-nm wavelength shift to the blue when used at the nominal 15-deg FIDO orientation. The transition wavelength is noted by the straight black line of 479.3 nm along with a spread of ± 1.3 -nm wavelength at 50% transmission across the aperture. This 20% transmission spatial variation across the aperture would raise calibration concerns if using this optic at the transition wavelength. However, the nominal dichroic coating specification of reflectivity of >90% for wavelengths short of 440 nm and >90% transmissive for wavelengths longer than 490 nm is easily met with this test. The design is also easily

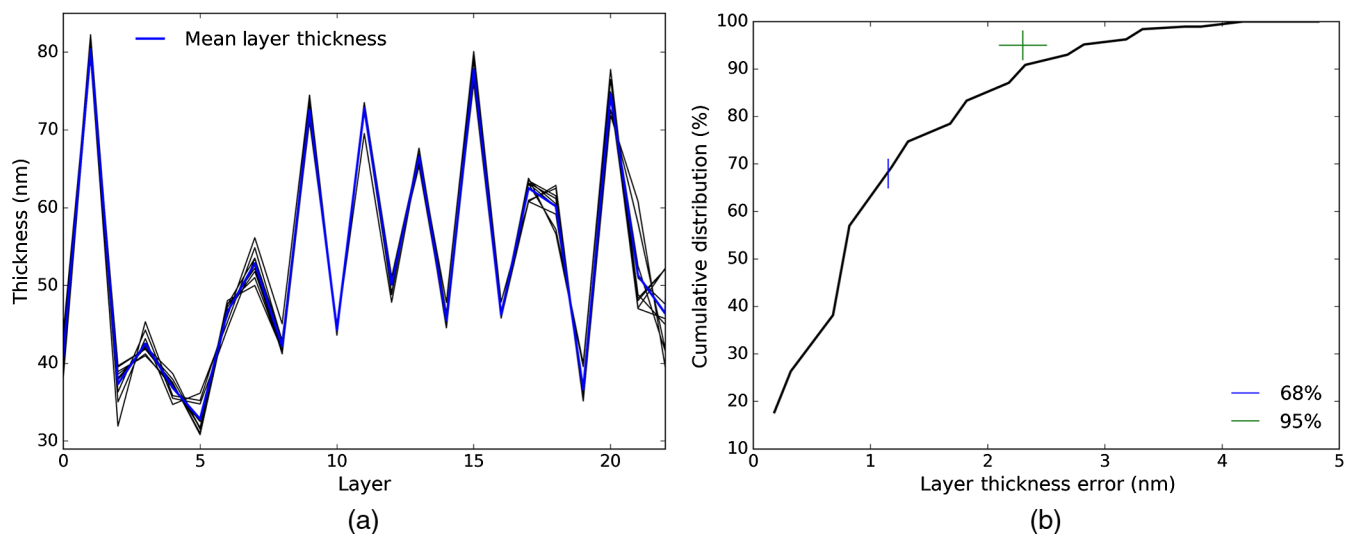


Fig. 19 TFCalc fits to the nine uniformity sample measurements for dichroic 465 test run 10-1053. (a) Shows all nine of the TFCalc models. Some layers are computed to vary more than others, especially the outer layer. (b) Shows the cumulative distribution of errors for each layer in each model with respect to the average.

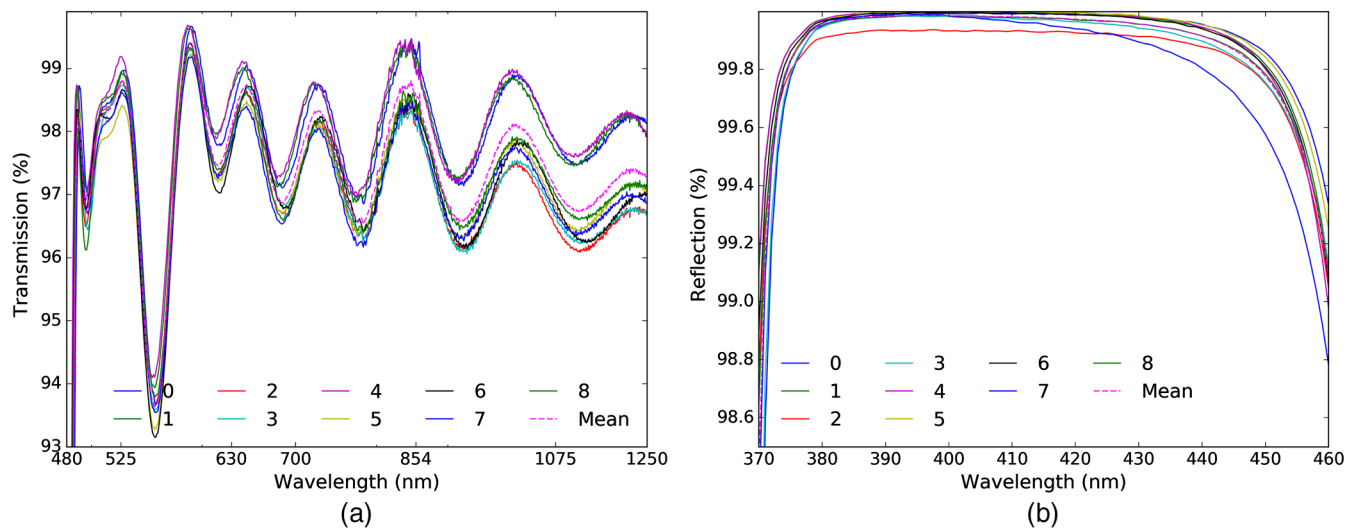


Fig. 20 (a) The transmission bandpass and (b) reflection bandpasses for IOI measurements of the nine samples throughout the chamber for the C-BS-465 dichroic coating uniformity test run 10-1053 at AOI = 0 deg.

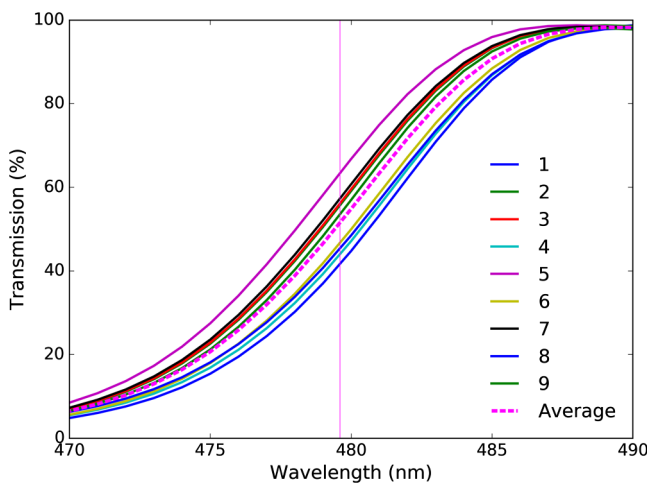


Fig. 21 Transmission measurements at AOI = 0 deg of the nine uniformity samples for C-BS-465 dichroic run 10-1053.

adjusted to slightly shorter transition wavelength following these test results.

We received all nine samples and performed testing in NLSP for polarization. Figure 22 shows the NLSP-measured retardance and diattenuation as a function of incidence angle. We tilted the sample between 0 deg and 45 deg. The retardance has strong spectral gradients near the transition wavelengths, as expected. Diattenuation is spectrally stable in transmission with mild oscillation in the transition band. For the beam at 15-deg incidence, the diattenuation is <1%.

We note that the NLSP reflective arm currently only measures samples at 45-deg incidence so we do not have a direct measurement of polarization performance at the FIDO incidence angle of 15 deg. The TFCalc models closely match the predictions, and this dichroic has essentially negligible polarization impact in the reflection band for the reflected beam. Retardance is <5 deg across the entire 380- to 460-nm wavelength range. Diattenuation is <0.2% across that same range. The IOI measurements of reflected diattenuation in this region are also

consistent with zero, given their measurement uncertainty. This will of course not be true for the more complex dichroics discussed later, but we conclude here that we have a valid model supported by several data sets for this simple FIDO dichroic.

5.2 Infinite Optics Dichroic A: Reflection 380 to 580 nm

When fitting significantly more complex coating designs, there is significant degeneracy. A completely free fit could adjust the thickness of every layer and the refractive index of each material to match the data. Fitting every individual spectral oscillation is usually quite difficult, resulting in unrealistic layer thickness and fits that are not close to the actual deposited coating. Often there are direct measurements and estimates of layer thicknesses recorded during the coating process providing the ability to constrain the fit. We demonstrate some constrained fitting here.

We received an Infinite Optics sample from run number 8-5652, which we labeled as Dichroic A. This dichroic reflects wavelengths shorter than roughly 580-nm wavelength. This design was not optimized for polarization or for use at high incidence angles and is expected to have strong polarization artifacts. The design uses 61 layers for a total 4.00- μm thickness. Most of the layers are alternating SiO_2 and TiO_2 at roughly quarter-wave thickness for a 510-nm reference wavelength (87 nm/59 nm per layer). We can compare the theoretical TFCalc design files with our NLSP measurements in transmission. Figure 23 shows the measured II Mueller matrix element from NLSP along with the TFCalc predictions at the appropriate AOI. The two NLSP measurements are shown in black with normal incidence as the solid line and 45-deg incidence as the dashed line. The blue and green curves show the TFCalc design files for incidence angles 0 deg and 45 deg, respectively.

We took the TFCalc design and adjusted the transmission to account for the Fresnel reflection off the uncoated back surface. Note that we had lower resolving power of the NLSP setup for these measurements. A 9-nm FWHM instrument profile reduced the magnitude of some of the narrow, low magnitude spectral transmission features seen in the lower left reflection band. It also mildly reduces some of the spectral ripple magnitudes

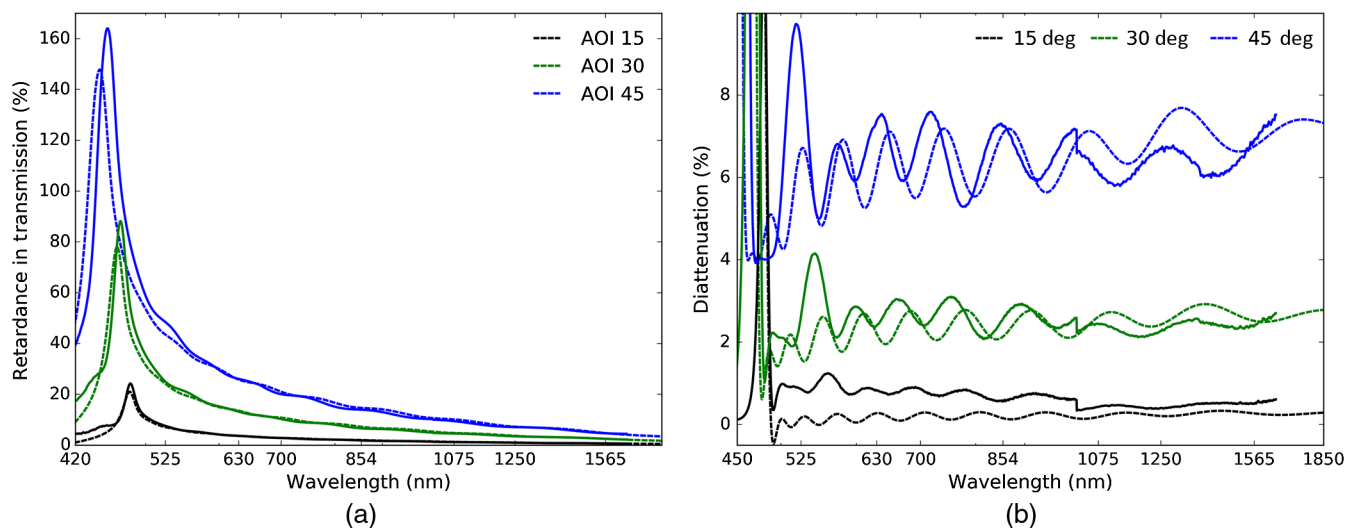


Fig. 22 (a) Transmission retardance and (b) diattenuation measured with NLSF at various incidence angles for the C-BS-465 dichroic samples. The solid lines show the data and dashed lines allow comparison with the best-fit TFCalc model predictions.

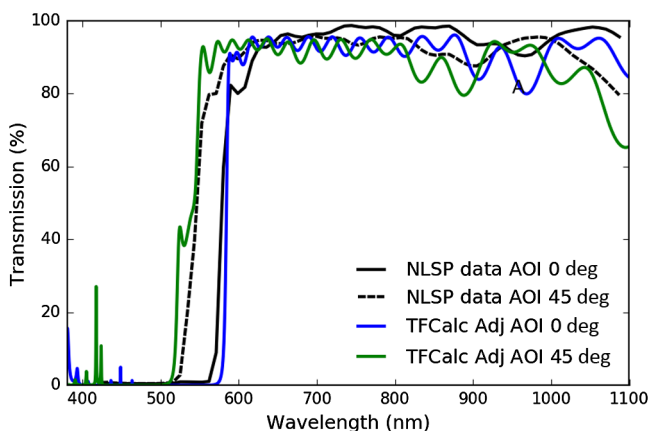


Fig. 23 NLSF transmission spectra are shown in black along with TFCalc design predictions as blue and green for IOI Dichroic A run number 8-5652.

at the shortest wavelengths. But there are significant amplitude differences and the instrument profile does not reduce the spectral ripple significantly. As seen in Fig. 23, the rough shape of the measured transmission curve is matched by the nominal design as is the 50/50 transition wavelength, but the stack up of thickness variation in 61 coating layers combined with variations in refractive indices can cause the detailed spectral dependence to change significantly in spectral ripple as well as transition wavelength. Fortunately, we can use TFCalc to constrain a fit of the design to the NLSF measured transmission, diattenuation, and retardance. Depending on the limits set for the allowable variation of each layer and on the refractive index values chosen, matching all spectral oscillations in a single transmission spectrum can drive the coating model far away from the actual layer thicknesses estimated by other means.

An example of the fitting process is shown in Fig. 24 for the transmitted beam at an incidence angle of 45 deg. The left graphic shows the measured transmission function along with various fits. The right-hand graphic shows retardance in green and measured diattenuation in blue as well as the same series of

constrained fits. Each of the individual fitted models is computed with ever wider range allowed for the variation of each layer thickness against the design. The fits improve to this single spectrum, but some layer thickness become quite different from the estimates derived during the coating process. The retardance is nearly a full wave in the transition band from short wavelength reflection to long wavelength transmission. The diattenuation is similarly close to 100%. In the transmission band, the retardance smoothly decays from a full wave around 600-nm wavelength to under 0.1 waves (36 deg) for long wavelengths. The diattenuation, however, has a more complex spectral pattern. This filter has been nominally designed to have high transmission of only around 700-nm wavelength. Diattenuation contains many spectral oscillations of a few percent in the high transmission bandpass but up to 20% at NIR wavelengths.

5.3 Infinite Optics Dichroic B: Reflection <680 nm on High Refractive Index Glass

We received another Infinite Optics sample from run number 7-2802, which we labeled as Dichroic B. This dichroic reflects wavelengths shorter than roughly 680-nm wavelength and is coated on a high refractive index SF11 glass substrate. This design was not optimized for polarization or for use at high incidence angles and is expected to have strong polarization artifacts and spectrally narrow features. The design uses 84 layers for a total 6.59- μm thickness. Most of the layers are alternating SiO_2 and TiO_2 , the same as the DKIST FIDO dichroic designs. In Fig. 25, we show the polarization properties of Dichroic B in transmission at 45-deg incidence derived from the NLSF-measured Mueller matrix. The retardance is shown in black using the left-hand y axis running from 0 deg to just over 300 deg. The blue curve shows diattenuation using the right-hand y axis running from 0% to 100%. As this dichroic is highly reflective for wavelengths shorter than 680 nm, the transmitted flux is very low. However, we do reproduce stable polarization measurements with NLSF even with transmission <1%. We have typical signal-to-noise ratios (SNRs) over 10,000 for a transmissive optic, so we still can achieve SNRs in the range of 1000 with 1% transmission. There are narrow spectral features in

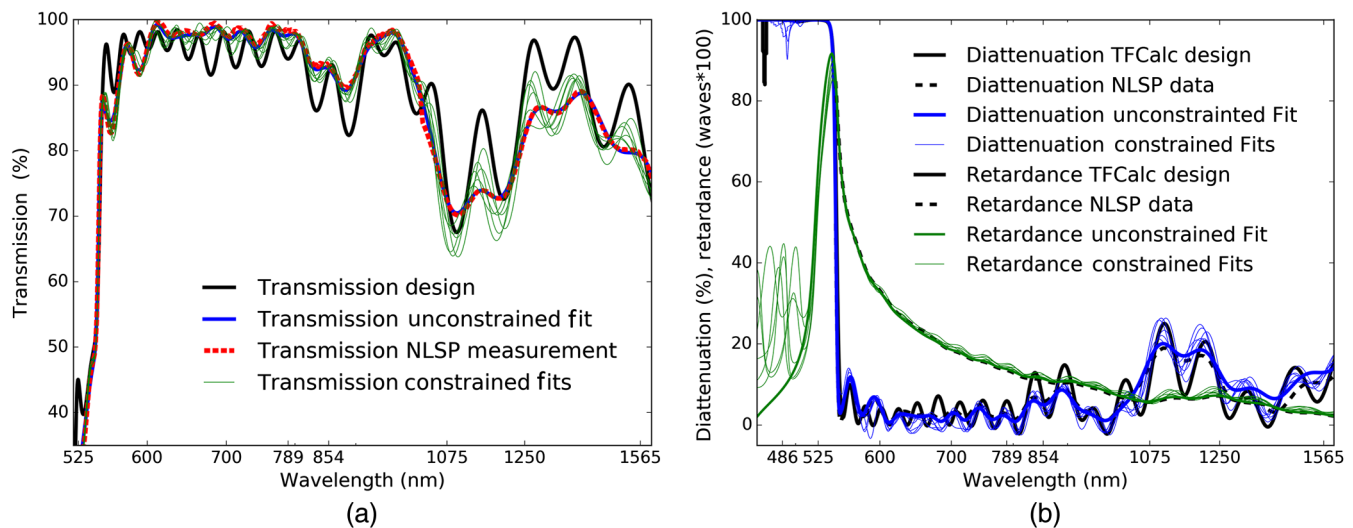


Fig. 24 (a) Shows the NLSF-measured transmission for the Dichroic A, IO run number 8-5652, as dashed red. The TFCalc design is solid black, the TFCalc unconstrained fit is solid blue (matching the NLSF data well), and the constrained TFCalc fits are thin green lines. (b) Shows the NLSF-measured retardance and diattenuation in transmission as black dashed lines with the TFCalc designs as solid lines. The Y axis is both percentage diattenuation and retardance in 100ths of waves. The various blue lines show TFCalc diattenuation models and green lines show retardance models.

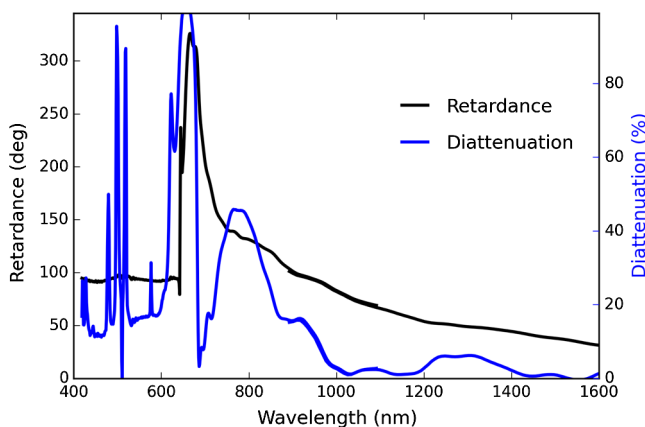


Fig. 25 The NLSF-measured polarization properties in transmission for the Infinite Optics Dichroic B sample at 45-deg incidence with run number 7-2802. Black shows retardance on the left-hand y axis. Blue shows diattenuation on the right-hand y axis.

diattenuation of the transmitted beam that are entirely real, as we detail in the next section. As this coating was not optimized for transmission, strong diattenuation is seen for the transmitted beam even in the transmission bandpass.

This coating has been designed only for high reflectivity at low incidence angles. For coatings designed without specification of polarization, the coating can have very strong rates of spectral change in addition to large magnitudes of both retardance and diattenuation. In Fig. 26, we show the NLSF-measured retardance and diattenuation of Dichroic B in reflection at an incidence angle of 45 deg.

The retardance is shown in black with multiple wavelength regions showing strong spectral changes wrapping through several waves of retardance. The diattenuation is shown in blue with large antisymmetric swings in the same wavelength regions where retardance changes quickly. Spectral changes are over $\pm 10\%$ in just a few nanometers wavelength, comparable to

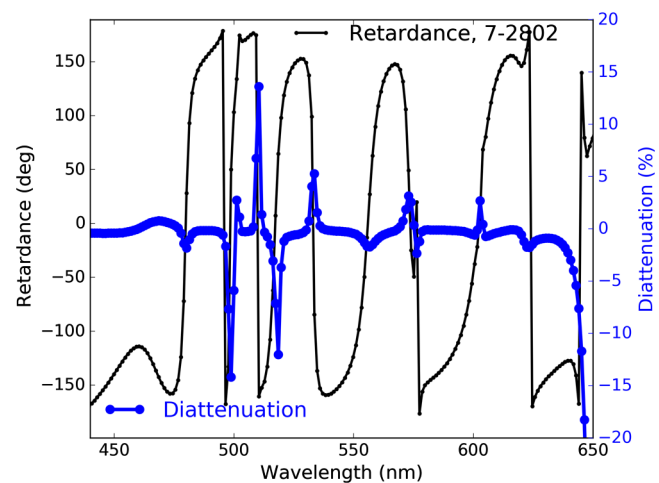


Fig. 26 The NLSF-measured retardance in black and diattenuation in blue for the Infinite Optics Dichroic B sample run 7-2802 at 45-deg incidence in reflection. The 440- to 655-nm wavelength region is selected as the efficient reflection bandpass.

the spectral resolving power of NLSF. We show this dichroic as an example of how optimizing a design for only reflectivity can create narrow spectral regions where the transmission and polarization performance pose calibration challenges.

5.4 Narrow Spectral Features: Spectral Calibration with Many-Layered Coatings

Coating models predict narrower spectral features and stronger wavelength gradients as the number of layers and coating thickness increase. Features in common astronomical dichroics can exist where the reflectivity can drop over 10% from the $>99.9\%$ nominal performance along with strong polarization-dependent response.

As an example, Fig. 27 shows the constrained fit TFCalc models to the NLSF data sets from above. Blue shows the

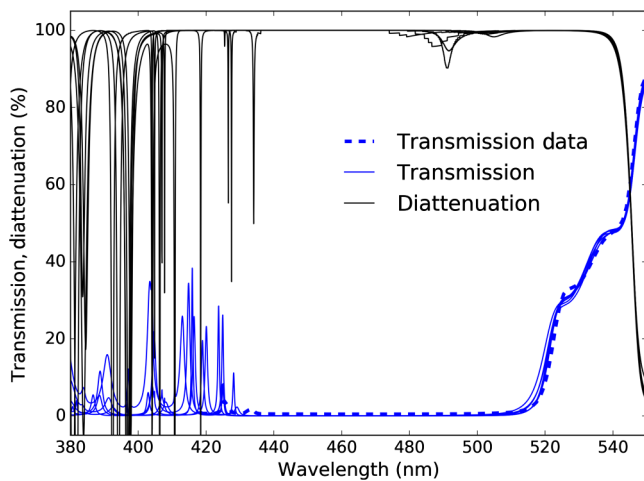


Fig. 27 The TFCalc models of Dichroic A run 8-5652 from a constrained fit to the NLSP data. Narrow, strong features are predicted at short wavelengths with high sensitivity to the specific constraints applied. Blue shows transmission and black shows diattenuation. The thick dashed blue line is the NLSP-measured transmission spectrum.

transmission spectrum and black shows the diattenuation for a 45 deg incidence angle. We note that in the reflection band around 450 to 500 nm, this design shows almost no narrow spectral features and minimal sensitivity to the varying fit constraints. However, at shorter wavelengths of 380 to 440 nm, there are transmission features predicted at amplitudes of 5% to almost 40% depending on the model. As NLSP does not have significant signal for this dichroic at short wavelengths, we can only plot the measured transmission spectrum as the thick blue line of Fig. 27.

We measured the transmission spectra for Infinite Optics Dichroics A, run 8-5652, and B, run 7-2802, over the 370- to 600-nm wavelength range at 4 pm per step with the Meadowlark Spex instrument we previously described.⁶⁹ In the Meadowlark Spex system, their double-grating CT spectrograph used a 30- μm wide slit setting and a photomultiplier as the sensor. Spex had an instrument profile of roughly 25 pm optical FWHM over

visible wavelengths. Sampling was 4 pm wavelength per step or about six samples per optical FWHM. Spectral resolving power is thus roughly 20,000 sampled at one part in 120,000.⁶⁹

Figure 28 shows examples of the narrow spectral features measured in the Infinite Optics Dichroics A and B. The left-hand graphic shows a 25-nm bandpass measuring transmission for Dichroic A run 8-5652 in the wavelength region where this optic is highly reflective. The nominal reflectivity is over 99.9% as designed but there are narrow spectral features that reach up to 7% transmission. In the right-hand graphic of Fig. 28, we collected several spectral features from both Dichroics A and B. We have centered them on a relative scale by the central wavelength seen in the legend. We then normalized them by the peak transmission. The wavelength-dependent profile of each feature is complex, but the widths are roughly 1 to 2 nm FWHM.

5.5 Summary of Dichroic Coatings: Spectral Features and Optimization

In Sec. 5, we have shown the nominal DKIST designs for the FIDO. The FIDO dichroic coating designs are shown using 25 to 96 layers and thicknesses from 1.5 to 8.8 μm . These designs are compared with as-built samples of many-layered coatings. We have shown NLSP spectropolarimetric data, the nominal thin film models and fits of those models to our as-built data. The first example dichroic (A, run 8-5652), shown in Sec. 5.2, has 61 layers and shows spectrally smooth behavior in both reflection and transmission with high reflectivity and a sharp transition. An alternate dichroic (B, run 7-2802) example, shown in Sec. 5.3, has very high reflectivity but spectrally narrow bands of high diattenuation along with retardance oscillations of over five waves in the reflection bandpass of 420 to 680 nm. We have then shown these very narrow features are quite real, measurable, and expected in various designs, in Sec. 5.4. We have presented spectrophotometric measurements with a resolving power of 20,000 on the Meadowlark SPEX system and example TFCalc design files showing how different dichroic designs can be quite sensitive to manufacturing errors and create these narrow but quite strong spectral features.

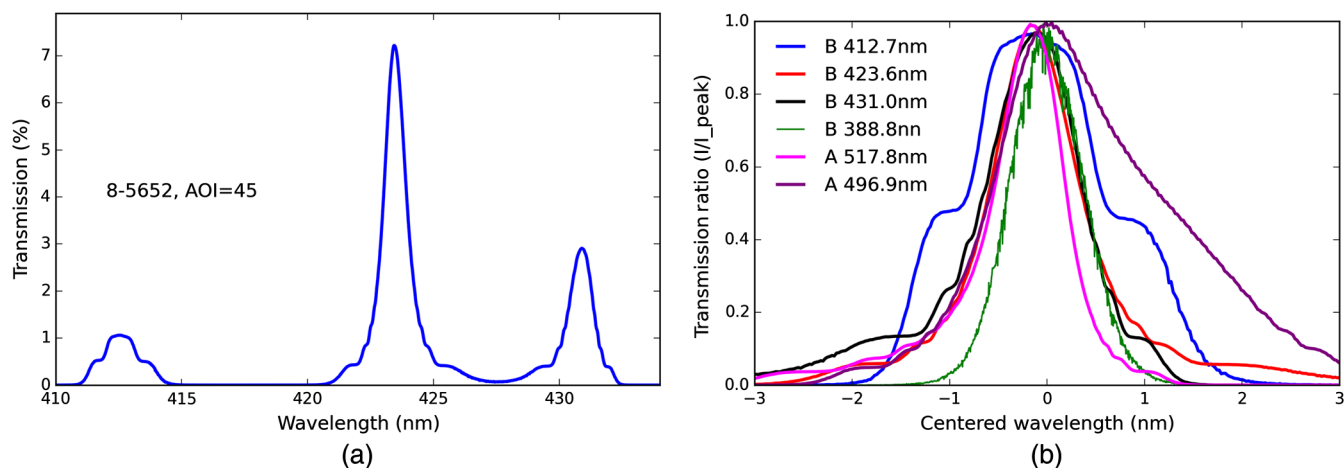


Fig. 28 Transmission measurements of Infinite Optics dichroics in the reflection bandpass. (a) Shows transmission for the run 8-5652 Dichroic A. Three narrow features at amplitudes of 1% to 7% transmission are seen in this bandpass and are predicted in the TFCalc model. (b) Shows a compilation of several narrow features in both run 7-2802 Dichroic B and run 8-5652 Dichroic A. Some features are Gaussian in spectral profile while others are complex. Amplitudes range from a fraction of a percentage to 7%.

Given these measurements of several dichroic styles, DKIST optimized our designs not only for high reflectivity but also for low diattenuation and spectrally smooth retardance while also being constrained by the minimum stress and wavefront error requirements. The C-BS-950 design presents challenges, given the nominal 96 layers, but the sensitivity was minimized and the retardance should maintain spectral gradients of <10 deg per nanometer of bandpass for almost all of the required bandpass with particular emphasis on key DKIST spectral wavelengths. We are presently performing a thorough coating design verification and repeatability study to ensure that DKIST achieves the required optical performance on the FIDO optics.

We have shown how the thin film design tools such as TFCalc can be used to verify that dichroic coatings fall within tolerances and also to predict the presence and magnitude of narrow spectral features. Many astronomical instruments are now observing simultaneously with other instruments often covering narrow bandpass at high spectral resolving power. To ensure success in designing and calibrating these instruments, the properties of all the many-layered coatings in the system must be known. By controlling the design, benign performance can be assured. For DKIST, we have shown mirrors, broadband antireflection coatings, and dichroics in the above sections. We now combine the optics into their appropriate groups and create a system-level model for DKIST with all coatings on all optics.

6 DKIST System Model for Polarization and Throughput

We now use the coating analysis and metrology to predict the mirror Mueller matrix and group model parameters for every optic ahead of each instrument modulator. With this group model, we can predict the polarization response of the system at any azimuth, elevation, or coude table angle.¹¹ We can also

make estimates of expected uncertainties in coating performance and show how a tolerance analysis could be done to inform mirror coating choices. In the system calibration process, we fit the group model parameters of diattenuation and retardance for every mirror group. These terms also combine with the derivation of a modulation matrix across the field of view of each instrument. Given our spectral smoothness requirements on the coatings, we can ensure that subnanometer wavelength variation between instrument bandpasses does not degrade the calibration of the telescope between instruments. Depending on the calibration fitting recipes used, a wide value search space can lead to degeneracies and unphysical results in the fit-to-mirror properties. By showing this tolerance analysis and our fitting errors, we show that we can significantly restrict the range allowed for fitting the telescope mirror group parameters. We also gain speed in computation when we can use simple gradient-minimization techniques as opposed to wide area search techniques (such as differential evolution). For DKIST with many simultaneous wavelengths and a 24-h calibration time requirement, the computational gains are expected to be significant. With our Berreman code we can make assumptions about the range of coating properties and directly compute the reflectivity, diattenuation, and retardance of the mirrors under several kinds of model perturbations. Knowing the range of expected polarization properties also helps in validating any DKIST-derived calibrations when using our custom retarders that we have mapped spatially and assessed for thermal instabilities.^{13,16,17}

In September 2018, we had acquired witness samples for every telescope mirror in the DKIST path that has been coated to date. This includes the optics M2 through M10. We received samples from M8 and M9 in late 2018 (as detailed in Sec. 10.9). In several cases, we received multiple witness samples from different spatial positions in the coating chamber. Figure 29

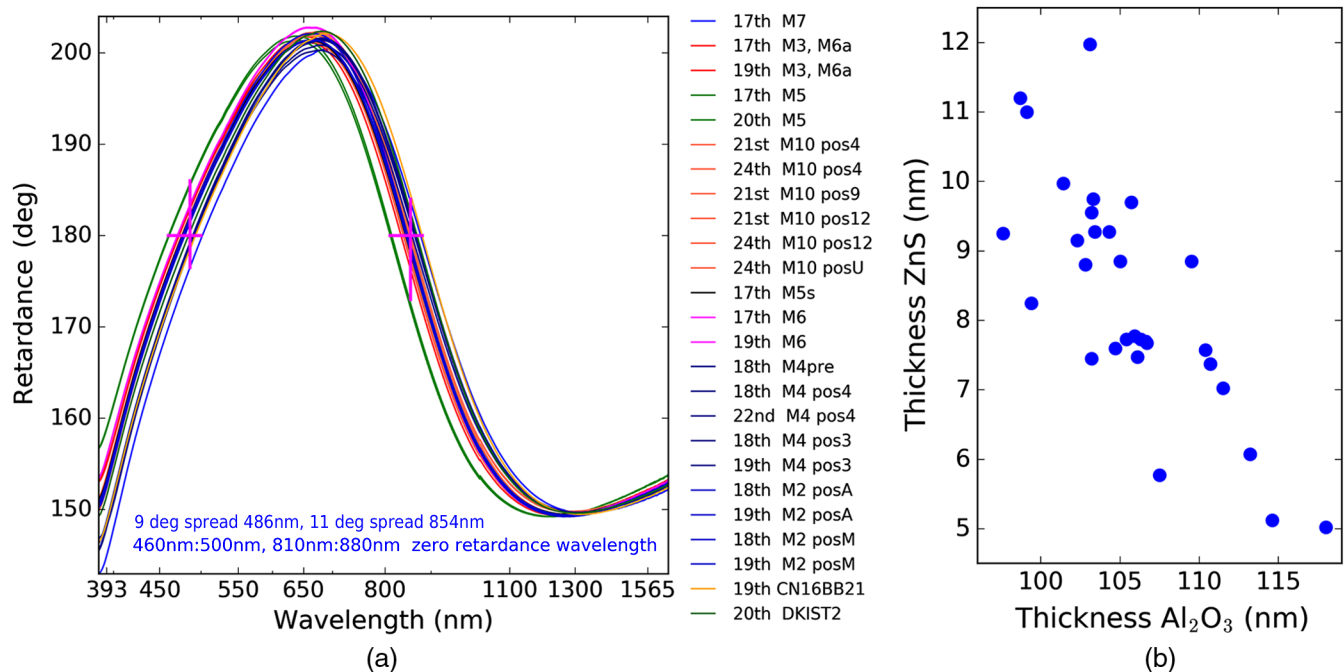


Fig. 29 (a) Shows the retardance derived from NLSP Mueller matrix measurements in September 2018 for the DKIST telescope mirrors along with comparison to some instrument partner witness samples. (b) Shows the best-fit thickness of the simple two-layer ZnS over Al₂O₃ model using the direct search brute-force method.

shows the retardance measurements from this September 2018 campaign in the left-hand graphic. In several cases, we remounted and remeasured samples to assess our procedures over timescales of >1 year. The repeatability and an assessment of the errors are included in Sec. 9. As noted in the figure, there is a spread of up to ~ 10 deg retardance at individual wavelengths. There is also a significant wavelength variation where the retardance spectrum crosses the theoretical net-zero-induced retardance value of 180 deg. The right-hand graphic of Fig. 29 shows the resulting thicknesses from our simple two-layer retardance fitting technique. There is significant scatter with a strong anticorrelation between thinner top layer and thicker bottom layer. The bottom layer varies in thickness by ± 10.2 nm, representing a roughly 10% thickness variation. The top layer fit varies by ± 3.5 nm but this represents a 40% variation. Of course, our simple two-layer model does not necessarily reflect the complexity in a coating that could contain many more layers than we are modeling. But this variation is representative of the variation in retardance measured for many samples. We can take this measured range of parameters and show the uncertainties in the DKIST system model, given this possible range of coating behaviors. We also can provide a more accurate system model, given that we can use these measured values to put a more representative coating specific to each mirror into the system model.

In Table 8, we show the two-layer model fits and the incidence angle assumed for a simple mirror group model. We use the brute-force method of fitting for minimum retardance difference between measurements and model using a model grid with a step size of 0.025 nm in ZnS and 0.1 nm in Al_2O_3 running from 0- to 250-nm thickness. The first column shows the chief ray incidence angle in degrees for each mirror. The second column shows the tilt axis in the local coordinates of the beam propagating to the mirror in the Zemax optical model. This column is meant to show that mirror groups do not necessarily share a plane of incidence and thus the Mueller matrix for each mirror group may not follow the simple equation for a single mirror.

In the DKIST system, the mirrors are crossed at many telescope pointings when the tilt axes are 90 deg away from each

other. In this case, the diattenuation and retardance subtracts, leading to a lower net magnitude in particular for the case of M7 and M8 through M10. We replace M8 and M9 values with other DKIST silver-coated mirrors as these optics (along with M7 and M10) are part of the modulation matrix combined with FIDO optics and instrument relay optics. The third column of Table 8 shows the brute-force fit thickness of the top ZnS layer using the RefractiveIndex.info refractive index. The fourth column shows the brute-force fit thickness of the Al_2O_3 layer when using the Boidin reference from RefractiveIndex.info for the refractive index. The last column shows notes on the selection of the fit parameters. We include the DKIST primary mirror (M1) in this table as the first row, as the bare aluminum metal coating does form an oxide layer (Al_2O_3). We show an example fit to M1 coating samples in Sec. 10.11. We also have several samples from different spatial positions in the chamber as well as repeat measurements on multiple days. We show the data set used for the fit as well as spatial position of the sample when available.

These models are representative of the measured range of variation as expected with normal coating manufacturing tolerances. As an example of the expected range of system performance, we can take our DKIST silver two-layer model and vary the thickness of each layer independently for each coating shot following our procurement schedule. We can make a grid of coating layer thickness models where the top ZnS layer is varied from 6 to 12 nm in steps of 2-nm thickness while the bottom Al_2O_3 layer varies from 95 to 110 nm in steps of 5-nm thickness. These thickness choices follow our layer thickness fits to retardance measurements of the many witness samples in the DKIST silver coating shots as well as the DL-NIRSP and Cryo-NIRSP shots from the same vendor with the same coating formula.

The mirrors that are coated in the same coating chamber shot will be assumed to have the same coating formula. However, each coating shot will vary independently from every other shot. Spatial variation is certainly present and measured in our samples through various vendors, but it is outside the scope of this paper. For the sake of simplicity with reasonable model accuracy, we will use the silver refractive indices that represent reflectivity at visible wavelengths in the reflectivity calculations. We use the silver refractive indices that better match retardance for calculating retardance and diattenuation. We note that the diattenuation in this model does not match the measurements to better than a fraction of a percent. Diattenuation was not included in the fit error metric, nor were the refractive indices of the silver fit. This gives model simplicity, and the range of polarization variation is similar for a variety of refractive index choices.

In Fig. 30, we show reflectivity ranges for the various DKIST mirrors as functions of incidence angle in the left-hand graphic computed with our Berreman package. The right-hand graphic shows the retardance ranges predicted for the individual DKIST mirrors downstream of the calibration unit. The primary and secondary mirrors form their own group which is static in time and fit separately as modeled in HS17.¹¹ The different colors represent different incidence angles for the various mirrors denoted in the legend.

Continuing the tolerance analysis, we combine mirrors into groups and compute polarization performance by multiplying the appropriate mirror Mueller matrices at the appropriate incidence angles. The simulated layer thickness variations on any

Table 8 DKIST telescope mirror model.

Optic	AOI (deg)	Ax	ZnS	Al_2O_3	Note
M1	14.0	X	—	4.0	Al_2O_3 over Al
M2	11.7	X	7.700	106.6	posA, 18th
M3	45.0	X	8.800	102.8	19th
M4	1.8	Y	6.075	113.2	pos3, 18th
M5	15.0	Y	8.250	99.4	20th
M6	30.0	Y	11.000	99.1	17th
M7	45.0	Y	5.025	118.0	17th
M8	5.3	X	8.850	109.5	Use CN16BB21
M9	10.0	X	11.975	103.1	Use CN PW1
M10	15.0	X	9.550	103.2	DM, posU 24th

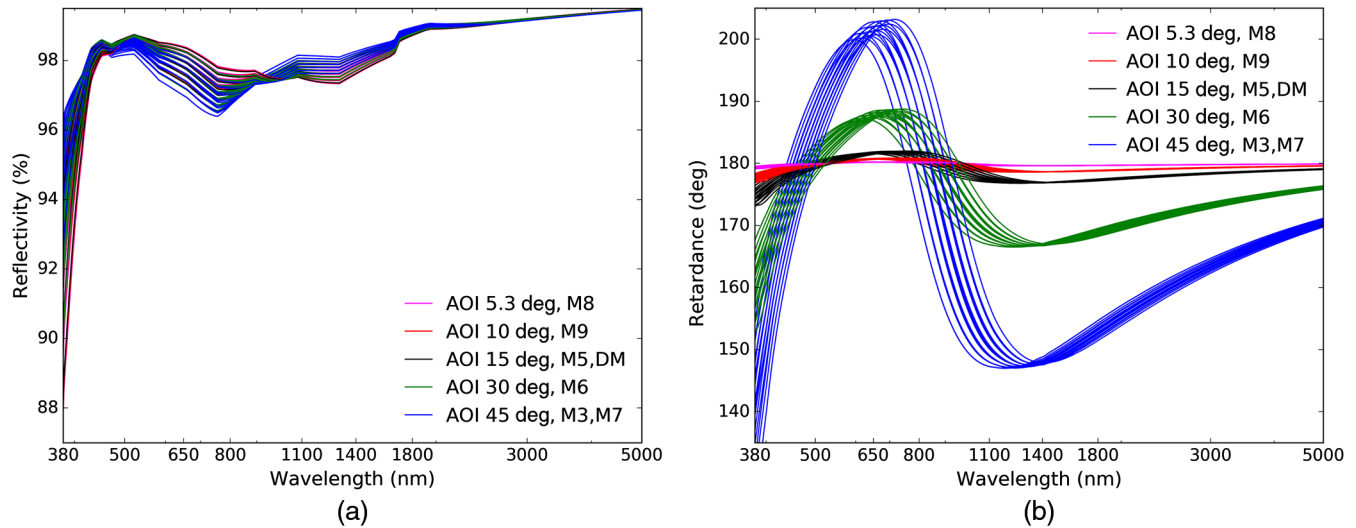


Fig. 30 Reflectivity and retardance tolerance analysis on the individual DKIST mirrors M1 through M10 at the appropriate incidence angles. (a) Shows reflectivity ranges at incidence angles noted in the legend. As we do not fit reflectivity, this range is representative but can be less accurate. (b) Shows the retardance model and these curves follow the measured retardance variation shown above.

one mirror are compounded with variations on every other mirror to evaluate the worst-case possibilities. Figure 31 shows this group model and the tolerance analysis. The left-hand graphic shows the retardance for the three mirror groups. The M5:M6 group is shown in green with relatively low retardance but significant variation in the tolerances because both mirrors are at significant incidence angles (15 deg, 30 deg). The M3:M4 group is shown in black with moderate retardance dominated by the 45 deg incidence of M3.

The M7 through M10 group is shown in blue. This group of mirrors is fixed on the coude table and will become part of the instrument modulation matrix. We group the mirrors independently for now here as they impact the expected variation of the instrument modulation matrix. The mirrors also impart some variation with instrument field of view on the polarization calibrations as the pupil is demagnified by a factor of 20 \times giving

rise to incidence angle variation of roughly 1 deg when observing over the 5 arc min field of view. Figure 31 shows how typical manufacturing tolerances can create variability in the expected polarization properties of the telescope optical path.

This M7:M10 group will impart significant complexity to the azimuth-elevation-dependent behavior of the telescope diattenuation and polarizance. M7 has significant retardance at a 45-deg incidence angle and there will be differences imparted to the first row and columns of the Mueller matrix. Equation (10) shows the theoretical form of the Mueller matrix for two mirrors that do not share a plane of incidence. The first mirror is tilted along the vertical plane becoming a Q diattenuator with retardance between U and V components. The second mirror is tilted along the 45-deg plane which creates U diattenuation and retardance between Q and V components. The resulting Mueller matrix has polarizance in the first column that is not equal to

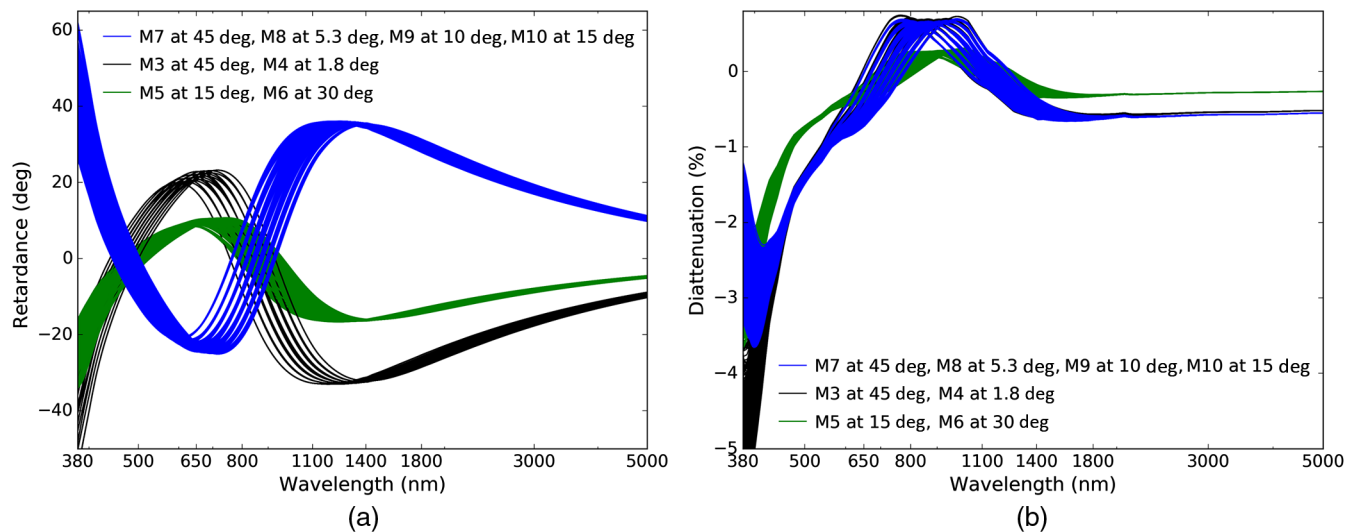


Fig. 31 (a) Group model retardance and (b) diattenuation tolerance analysis. The mirrors are grouped appropriately and model Mueller matrices are multiplied. Black shows the M3:M4 group. Green shows the M5:M6 group. Blue shows the M7:M9:M9:M10 group where M10 is the AO system deformable mirror.

the diattenuation in the first row. With the elevation and azimuth axes providing such rotations to each group of mirrors, we expect significant differences for DKIST in the first row and column of the Mueller matrix.

$$\mathbf{M}_{\text{toFIDO}} = \mathbf{M}_{10}\mathbf{M}_9\mathbf{M}_8\mathbf{M}_7 \quad \mathbb{R}(-Az - TA)$$

$$\mathbf{M}_6\mathbf{M}_5\mathbb{R}(-El)\mathbf{M}_4\mathbf{M}_3\mathbf{M}_2\mathbf{M}_1 \quad \mathbb{R}(El) \quad \mathbb{R}(Az + TA), \quad (9)$$

$$\mathbb{M}_{ij} = \begin{pmatrix} T_1 & D_1 & 0 & 0 \\ D_1 & T_1 & 0 & 0 \\ 0 & 0 & c_\gamma & s_\gamma \\ 0 & 0 & -s_\gamma & c_\gamma \end{pmatrix} \begin{pmatrix} T_2 & 0 & D_2 & 0 \\ 0 & c_\beta & 0 & s_\beta \\ D_2 & 0 & T_2 & 0 \\ 0 & -s_\beta & 0 & c_\beta \end{pmatrix}$$

$$= \begin{pmatrix} T_1T_2 & D_1c_\beta & T_1D_2 & D_1s_\beta \\ T_2D_1 & T_1c_\beta & D_1D_2 & T_1s_\beta \\ D_2c_\gamma & -s_\gamma s_\beta & T_2c_\gamma & s_\gamma c_\beta \\ -D_2s_\gamma & -c_\gamma s_\beta & -T_2s_\gamma & c_\gamma c_\beta \end{pmatrix}. \quad (10)$$

We can implement the group model by combining the Mueller matrices derived for each mirror. We get the diattenuation and retardance using the Berreman calculus with the coating layer thicknesses in Table 8 and the theoretical equation for a flat fold mirror at a single incidence angle from Eq. (13). We then apply the geometrical rotations between the groups of mirrors as the telescope rotates in azimuth, elevation, and CL table angles. In Eq. (9), we explicitly show the positive and negative rotation matrices as required to rotate the groups of mirrors into the appropriate frame. We combine the azimuth and CL table angle as the laboratory freely rotates to arbitrary orientation.

Figure 32 shows an example of such a group model calculation. We have normalized all elements by the [0, 0] element except the [0, 0] element itself as in Eq. (8). As we have shown

in Eq. (10) for two mirrors at 45-deg relative rotation between incidence planes, the dominant impact of the geometry is to create oscillations in azimuth and elevation as the mirror properties add when sharing planes of incidence and subtract when having orthogonal planes of incidence. We run this calculation over a full 360 deg of azimuth + table angle to show the symmetry of the combined optical system. We also run the calculation from 0 deg to 180 deg in elevation axis to show a complete cycle of parallel and perpendicular mirror pair incidence planes. The telescope mount structure is not capable of this articulation, but this simulation shows the symmetry of the underlying coating model behavior as well as the geometric QU rotation with azimuth and elevation.

We note that there are very slight changes in system transmission seen in the [0,0] matrix element. The color scale labels in Fig. 32 round to three decimal places for clarity. The transmission ranges from 89.26684% to 89.26595% or a range of only about 9 parts per million. This tiny effect is easily ignored. The IV and VI elements are roughly a factor of 2 different. We now have the telescope mirrors M1 through M10 modeled with as-built coating formulas and the associated azimuth-elevation-table-angle behavior modeled. Next we consider the dichroics and feed optics of individual instruments to show the polarization behavior of the rest of the optical train to instrument modulators.

6.1 Instrument Feed Optics: ViSP Reflectivity and Polarization with Many Layers

The ViSP has three enhanced protected silver mirrors between the last FIDO optic reflection and the spectrograph entrance slit. The original specification had very high reflectivity mirrors using 29 dielectric layers and a physical thicknesses of 3 microns. Thick, many-layer designs can have very narrow spectral features that impact polarization calibration and heightened

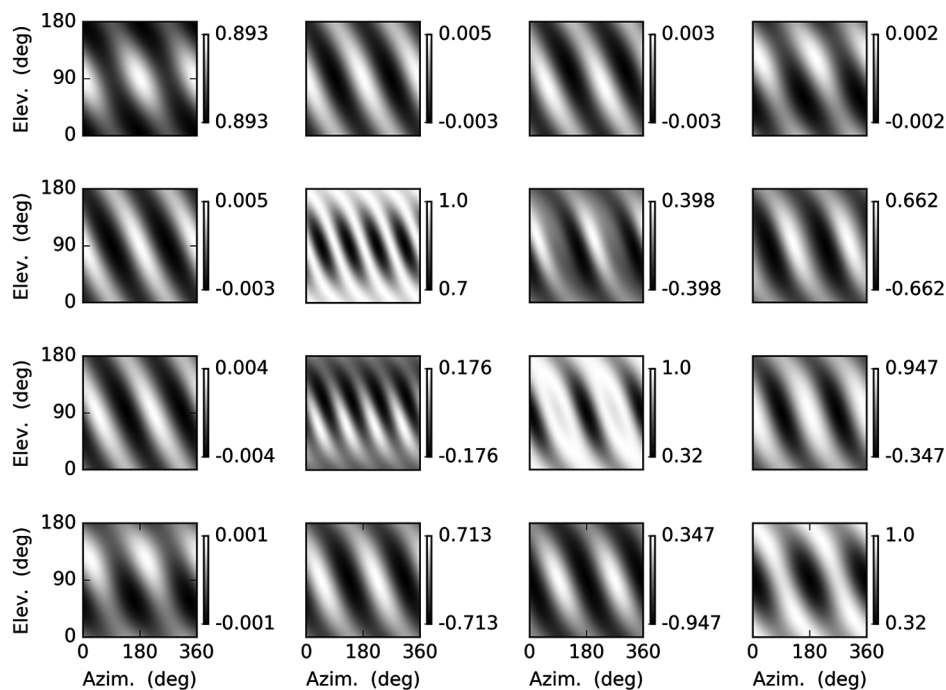


Fig. 32 The Mueller matrix for the combined optics of M1 through M10 as combined in the system group model at 1565-nm wavelength. Each element shows azimuth from 0 deg to 360 deg and elevation angle from 0 deg to 180 deg.

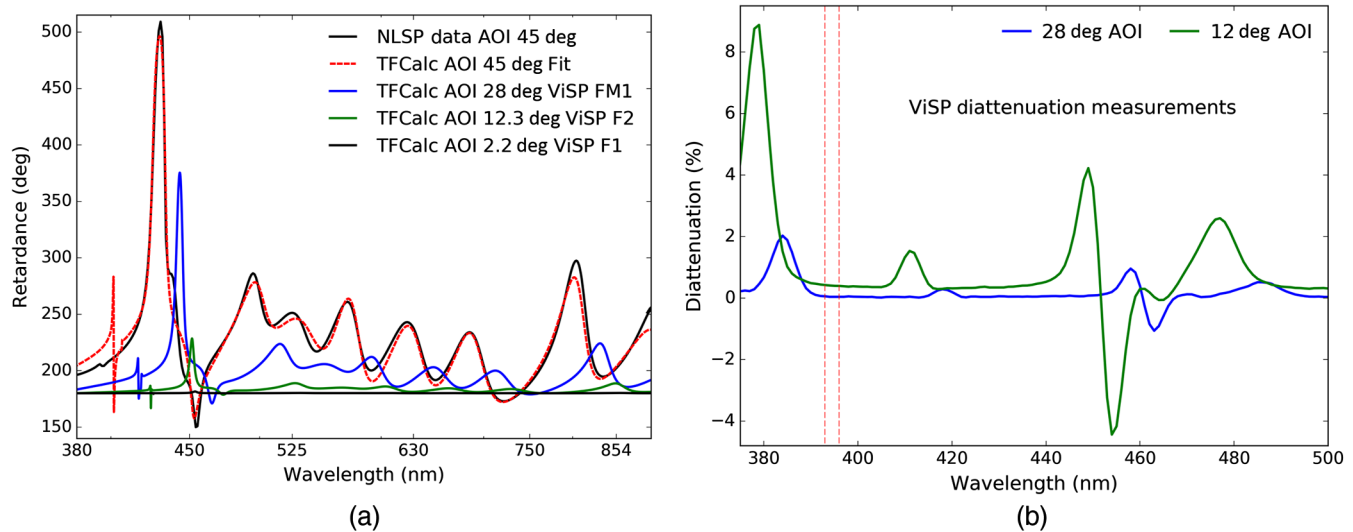


Fig. 33 (a) Shows retardance measured with NLSP for the ViSP feed mirror coating witness sample at 45-deg incidence from 380 to 900 nm as the oscillating black curve. The TFCalc model fit to that NLSP retardance is shown as the dashed red line. With this successful TFCalc fit, we then predict the retardance for the ViSP mirrors FM1, F1, and F2 at the appropriate incidence angles. (b) Shows vendor-measured reflected diattenuation at the appropriate ViSP incidence angles in the 380- to 520-nm bandpass where the mirrors show very strong changes.

sensitivity to various manufacturing and environmental conditions. Though the ViSP team has stripped and recoated their optics, we consider what would have been the polarization properties of these feed optics.

For the baseline ViSP feed mirrors coatings, we were given a coating design file for the coating with roughly 29 layers of dielectric material over silver. Figure 33 shows the NLSP measurements of a witness sample retardance measurement at 45-deg incidence along with the TFCalc model fit to that data set in the left-hand graphic. With this TFCalc model fit to retardance at 45 deg over wavelengths 380 to 800 nm, we can then predict performance for the baseline ViSP mirrors before stripping at appropriate incidence angles outlined in Table 9. ViSP FM1 at 28-deg incidence is shown in blue. The ViSP-powered optic F1 is shown in black at 2.2-deg incidence. The ViSP-powered optic F2 is shown in green at 12.3-deg incidence.

The polarization introduced by these three mirrors combine with the diattenuation and retardance introduced by the tilted broadband antireflection-coated glass substrate of the slit mask to create static elements of the ViSP system modulation matrix. The modulator is mounted behind the slit mask. Table 9 shows the three ViSP feed optics between the FIDO and the ViSP modulator. The ViSP slit masks are deposited on a glass

Table 9 ViSP feed.

Optic	AOI (deg)	Run
FM1	28	ViSP1
F1	2.2	ViSP1
F2	12.3	ViSP1
Slit _r	5.4	ECI
Slit _b	5.4	ECI

substrate mounted at 5.4-deg incidence angle to the beam. Both sides of this substrate are coated with a broadband antireflection coating with reflectivity averaging 1.0% over the 380- to 900-nm bandpass. Each side has slightly different coating behavior with both coatings having spectral oscillations ranging from 0.2% to 1.5% across the bandpass from shot-to-shot variation. Given the low incidence angle and high transmission, the retardance and diattenuation contributions are very small from this optic.

Figure 34 shows the parallel (P) and perpendicular (S) polarization state reflectivity of the ViSP fold mirrors measured at the appropriate incidence angles for the ViSP fold mirrors in the left-hand graphic, measured several months after applying the original (now stripped) coating. The ViSP FM1 is at 28-deg incidence plotted as the solid lines. The ViSP F2 mirror is at 12.3-deg incidence and is shown as the dashed lines. As expected, when the incidence angle increases, the complex spectral pattern generally shifts to the blue and changes morphology. The DKIST-enhanced silver mirror coating is shown as a comparison using black lines. Solid line shows a model while a dashed line shows reflectivity data for one of the DKIST mirrors (M10). Two dashed vertical lines show the Ca II spectral lines of interest for ViSP at 393.4 and 396.9 nm, which drove the coating design.

We note that the band of reflectivity at 80% to 90% was not present in the original test coating metrology. A manufacturing error gave rise to the actual mirror coatings behaving differently than the preliminary test coatings. The TFCalc models fit to vendor data on the ViSP-enhanced silver coating failed to reproduce the relatively low reflectivity curves measured by the vendor in the 450- to 490-nm bandpasses. However, the model does show that the wavelength shift from incidence angles of 12.3 deg to 2.2 deg are very small. We do not have vendor reflectivity data at 2.2-deg incidence, but we can approximate the F1 mirror as the average of S and P reflectivity curves at 12.3 deg with zero diattenuation and zero retardance. Using this assumption, we can make a reflectivity model of the three combined ViSP

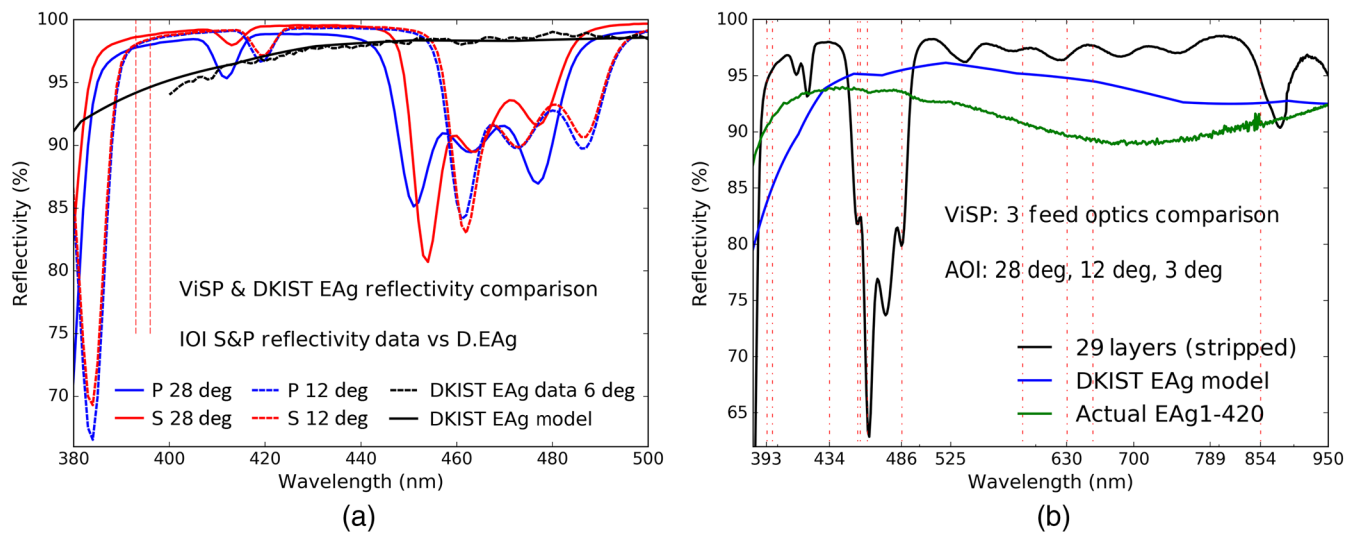


Fig. 34 (a) Shows the *S* and *P* reflectivity measured by the vendor for a witness sample from the single coating shot covering all three ViSP fold mirrors. The solid lines show incidence angle 28 deg for ViSP FM1 and dashed lines show 12 deg for ViSP F2. The black lines show both data (dashed) and models (solid) of the DKIST silver for comparison. (b) Shows the reflectivity of the combined ViSP mirrors with each mirror at the appropriate incidence angle. Black shows the highly enhanced coating with the measured reflectivity issue for the three combined optics. Blue shows the nominal DKIST silver formula (D.EAg) modeled for each optic at the appropriate incidence angle. Green shows the stripped and recoated mirrors as measured using the formula EAg1-420, the same as for the FIDO mirrors.

feed mirrors as the black curve shows in the right-hand graphic of Fig. 34. The system throughput would have generally been around 96%. We show common atomic spectral lines in Table 10 intended for ViSP observations that are noted as vertical dashed lines in some figures of this section. However, there is a drop to roughly 70% to 75% throughput that will impact observations of spectral lines, such as Ba II at 455.4 nm, Sr I at 460.7 nm, and H_{β} at 486.1 nm shown as vertical dashed lines. In addition, there is a drop to 90% throughput for the Ca II NIR line at 854.2 nm. Given this metrology result, these mirrors had been stripped and recoated in October 2018.

Table 10 Ex. lines.

λ (nm)	Name
393.4	Ca II K
396.9	Ca II H
434.1	H_{γ}
453.6	Ti I
455.4	Ba II
460.7	Sr I
486.1	H_{β}
587.6	He I
630.2	Fe I
656.3	H_{α}
854.2	Ca II

The new system throughput after stripping and recoating the three ViSP feed mirrors are shown as the green curves in the right-hand graphic of Fig. 34. These curves are generated using spectrophotometry on witness samples for the two appropriate coating shots. The blue curve shows the model prediction for the nominally specified DKIST-enhanced protected silver. As shown above, the as-coated performance for this coating can vary substantially so we only show the nominal modeled performance. Each coating shows a few percent throughput loss at various wavelengths, but the polarization curves are very smooth, following the two-layer coating models shown in previous sections.

Figure 35 shows the polarization model for the three ViSP feed optics combined at the appropriate incidence angles for the older (baselined) 29 layer coatings. The Mueller matrices are created for each optic and multiplied in sequence to create the model. The reflectivity and diattenuation from the vendor data are used while the retardance is predicted from the TFCalc model fit to our NLSP retardance measurements. The left-hand graphic of Fig. 35 shows wavelengths between 380 and 550 nm a different vertical scale than the right graphic covering 500 to 950 nm. Around 450 nm there is a change of retardance of about one full wave over roughly 15-nm bandpass as the retardance goes from zero to over half wave and back. The spectral change in retardance in this bandpass goes over 60-deg retardance per nanometer of bandpass. This instrument would have to be calibrated at high spectral resolving power to account for the rapid spectral changes in this bandpass. Figure 35 also includes vertical lines that denote ViSP spectral lines of interest. Fortunately, the 434.1 nm H_{γ} line and 453.1 nm Ti I line avoid this coating retardance feature. There is a band of relatively high diattenuation at slightly longer wavelengths of 445 to 490 nm with magnitudes of over $\pm 4\%$.

The right-hand graphic of Fig. 35 shows the three mirrors at longer wavelengths. The retardance oscillates between 0 deg

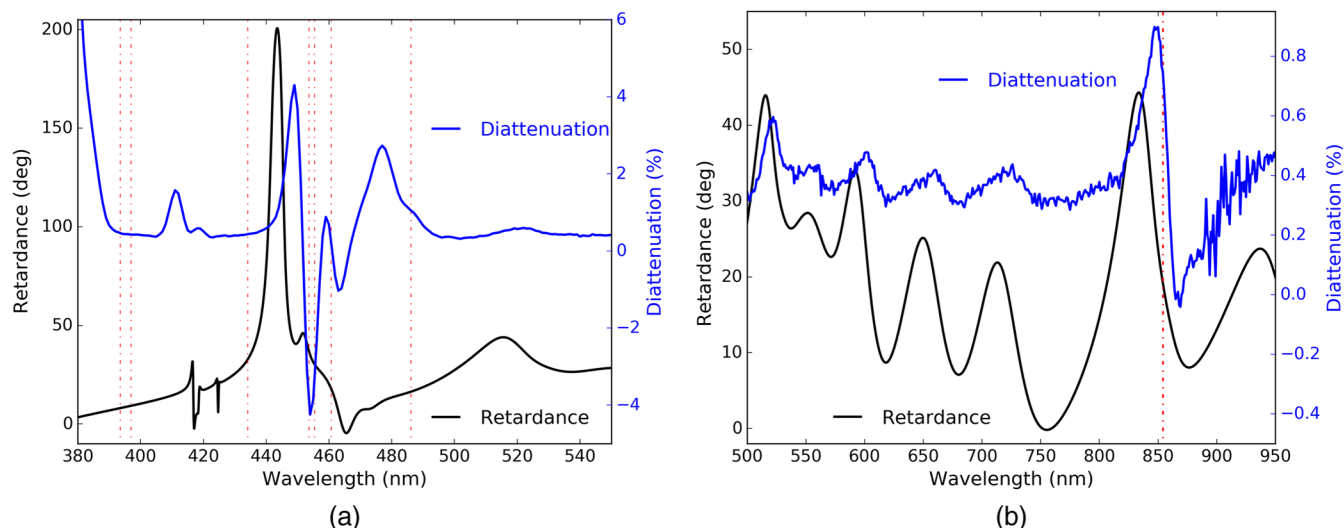


Fig. 35 Retardance and diattenuation from the combination of ViSP feed optics FM1, F1 and F2 before stripping of this 29 layer coating. (a) Shows the 380- to 550-nm wavelength region. Retardance varies by almost 200 deg around 445-nm wavelength as seen by the black curve on the left-hand Y axis. The diattenuation is shown in blue using the right-hand blue Y axis, varying by $\pm 4\%$ across adjacent wavelengths. (b) Shows longer wavelengths on reduced Y scales.

and 45 deg with an oscillation period much larger than the nanometer scale ViSP bandpass. There is a small diattenuation feature around the 854.2 nm Ca II spectral line. Thus, we could have expected some mild continuum polarization gradients in calibrations. We show, in Sec. 10.4, further confirmation of spectrally narrow reflectivity and polarization artifacts using our own NLSM metrology in an image-rotator (K-cell)-type configuration even at incidence angles of 11 deg. Though these coatings may have offered high reflectivity, when high spectral resolving power and polarization are considered, these coatings could have caused substantial calibration complexity.

6.2 DKIST and FIDO Configured for DL-NIRSP On-Disk Observations

In this section we show example calculations of the DL-NIRSP system modulation matrix and group model terms, given the uncertainties in coatings. We use the $F/24$ configuration and describe the impact of incomplete knowledge of coating properties in computing expected Mueller matrices for the optics. In Table 11, we show which beam splitters and mirrors would be installed at which stations. We choose a setup with maximum transmission in the wavelength range from 465 to 1800 nm, allowing DL-NIRSP to cover the full wavelength range within its capabilities. The DL-NIRSP sees high transmission through the windows and the dichroic beam splitter C-BS-465. In the last two stations, CL3 and CL4, we put in a window with antireflection coatings on both sides.

As a demonstration, we chose to install the FIDO window with an uncoated front surface C-W2 in the optical station CL2a. This window would send the $\sim 4\%$ Fresnel surface reflection to VBI-blue so that instrument could perform its function as a context imager at wavelengths from 380 to 465 nm for the ViSP spectrograph slit. The beam transmitted through C-W2 would contain significant flux for wavelengths shorter than 465 nm due to the dichroic reflection off C-BS-465. ViSP can be configured to observe wavelengths shorter than this, subject to the constraint on physical spacing between the camera arms. With the antireflection-coated window C-W1 in station

Table 11 FIDO Config 1.

Station	Optic
CL2	C-BS-465
CL3	C-W1
CL4	C-W3
CL2a	C-W2
Camera	λ (nm)
DL-VIS	530
DL-NIR1	1083
DL-NIR2	1565
ViSP1	393
ViSP2	455
VBI-blue	393

CL3, the beam going to VTF and the VBI-red systems would have very little flux and render these systems undesirable for use in this configuration. In Fig. 36, we show a simplified cartoon of the FIDO setup and the wavelength ranges for the various instruments.

In the lower half of Table 11 we also show an example of some camera configurations possible with this setup. For this particular observing setup, the ViSP and the blue arm of VBI receiving 4% of the flux would both be able to simultaneously observe in a few relevant channels.

We choose two example wavelengths for the Ca II UV line at 393 nm and the Ba II line at 455 nm as a convenient second wavelength. The ViSP is flexibly configured so several alternate choices are possible. We list the three cameras in DL-NIRSP

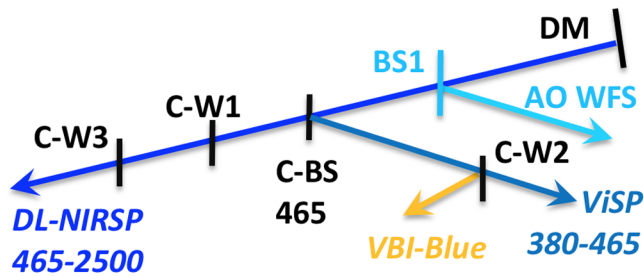


Fig. 36 The FIDO layout for configuration 1.

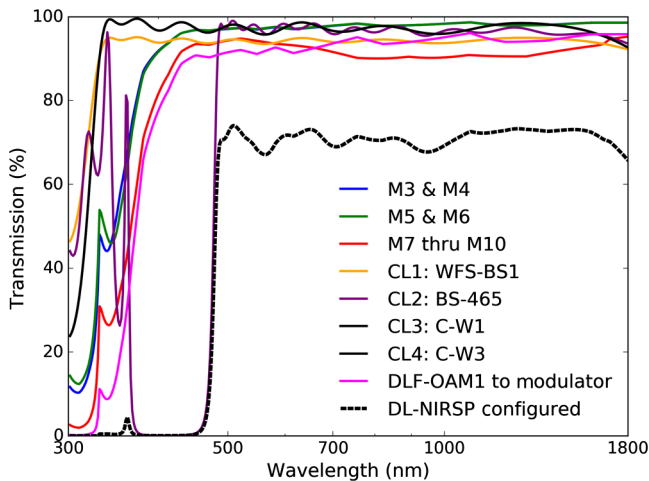


Fig. 37 The DL-NIRSP system transmission in this configuration for all mirror groups beyond M1 and M2: DKIST M3 to M10, BS1, FIDO optics, and instrument feed mirrors.

with three example wavelengths. We had chosen the shortest wavelength presently planned for the visible channel at 530 nm. We note that alternates include 587, 630, 789, and 854 nm, which can be easily observed in this FIDO configuration. Similarly, the two NIR cameras could also observe 1075, 1080, or 1430 nm.

In Fig. 37, we show the transmission functions of all mirror groups and also all coude optics. We use the silver refractive indices that are closer to the measured mirror reflection values for this calculation. The WFS-BS1 optic is assumed to have a bare fused silica front surface reflection computed directly from the Fresnel equations. The back surface is coated with WBBAR1, as described in Sec. 4. We perform the same calculation for the FIDO windows C-W1 and C-W3 where both surfaces are coated with WBBAR1. The FIDO dichroic C-BS-465 utilizes the transmission from our best-fit TFCalc model on the front surface and the WBBAR1 coating on the back surface.

We show in Fig. 38 the retardance and diattenuation for propagation through the FIDO optics in configuration 1 as well as the WFS-BS1. The diattenuation is a relatively small 1% to 2% across the wavelength range transmitted to DL-NIRSP. The retardance is 10 deg at 530-nm wavelength caused almost entirely by the front surface dichroic coating of C-BS-465.

The diattenuation in the DL-NIRSP modulation matrix is a roughly equal combination of the transmissive optics in FIDO and the WFS from Fig. 38, along with the three high incidence angle fold mirrors within the instrument relay optics. For the retardance, the three high incidence mirrors in the DL-NIRSP optics dominate with magnitudes up to 100 deg varying strongly

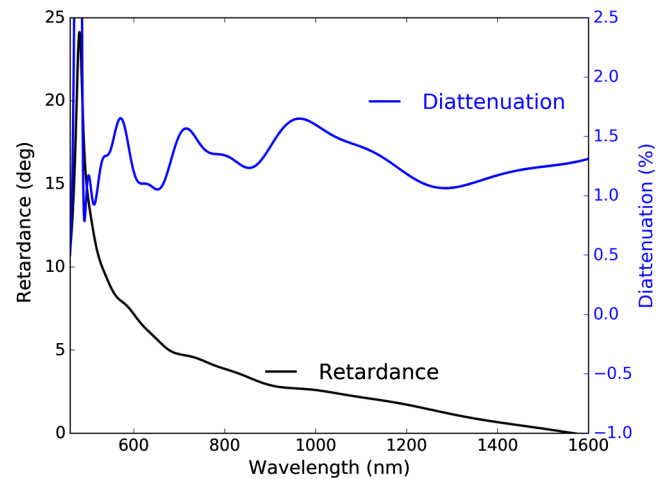


Fig. 38 The retardance in black and diattenuation in blue caused by the transmissive optics WFS-BS1, C-BS-465, C-W1, and C-W3 combined as installed for FIDO configuration 1.

across the visible and NIR wavelength region. The FIDO optics is <10 deg at most wavelengths and are a very small portion of the system retardance. The DKIST telescope mirror retardance from Fig. 31 is also significant at roughly one-third this magnitude and are also time-dependent. Diattenuation of the DKIST mirror groups has a magnitude similar to the combined FIDO optics and DL-NIRSP feed optics before the modulator.

In summary, the telescope, FIDO optics, and DL-NIRSP feed mirrors give roughly 70% throughput from 525 to 1600 nm wavelength. The DL-NIRSP feed optics is the dominant source of retardance at magnitudes up to 100 deg. The diattenuation is roughly equal combinations of feed mirrors and FIDO optics in this configuration but with combined magnitudes less than several percent.

6.3 DKIST and FIDO Configured for Multi-Instrument Spectropolarimetry

We consider in this section a configuration for the FIDO optics that operates all cameras in all three AO-assisted DKIST polarimetric instruments.

In Fig. 39, we show a schematic for which FIDO dichroic beam splitters and windows will be installed in which stations. The WFS-BS1 sends the 4% Fresnel reflection from the uncoated fused silica window to the AO system. In station CL2, we mount dichroic C-BS-555 where we reflect wavelengths shorter than 555 nm toward ViSP and VBI-blue. In station CL3, we mount dichroic C-BS-680 to reflect wavelengths between 555 and 680 nm toward VTF and VBI-red. The final station CL4 has the window C-W3 with broadband antireflection coefficients on all surfaces for high transmission. We show the beam splitters and stations in Table 12.

In station CL2a, we install the window C-W2 which sends the 4% Fresnel reflection from the uncoated front surface toward VBI-blue. This camera operates as a context imager for ViSP with limited flux. ViSP can be configured to operate three cameras over a diverse range of spectral lines. In Table 13, we arbitrarily choose the three ViSP camera wavelengths to cover the Ca II H and K lines at 393 nm, the H_{β} line at 486 nm, and the photospheric Fe I line at 525nm. In station CL3a, we install the dichroic C-BS-643 which would transmit 643 to 680 nm toward the VBI-red camera. The reflected beam would allow

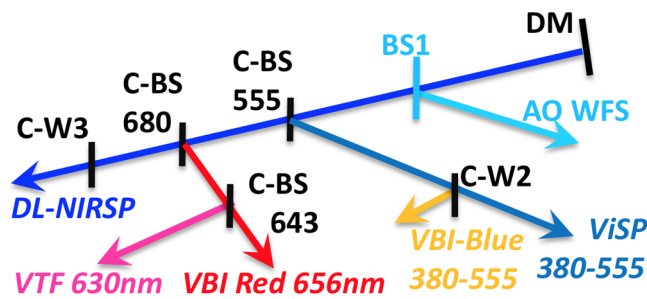


Fig. 39 The FIDO layout for a configuration where all polarimetric cameras are operated simultaneously.

Table 12 FIDO Config 2.

Station	Optic
CL2	C-BS-555
CL3	C-BS-680
CL4	C-W3
CL2a	C-W2
CL3a	C-BS-643

VTF to observe in the 555 to 643 nm wavelength range. It has one filter for the H_{α} line at 656 nm in this wavelength range.

In Table 13, we list the VTF as observing this 630-nm line. We note that VTF technically operates three separate cameras. Two cameras are synchronized and are operated as a dual-beam spectropolarimeter as the etalons scan the spectral line in steps of a few picometers. These two cameras can be compared to the spectrograph instrument calibrations as these cameras scan in wavelength to sample the spectral line. The third camera is also synchronized with the two polarimetric cameras. This third camera is set to observe continuum wavelengths adjacent to the spectral line. These three cameras all operate at wavelengths very close to 630 nm and are treated as one wavelength range, similar to spectrograph calibrations for our purposes here.

Table 13 Cameras: 2.

Camera	λ (nm)
ViSP1	393
ViSP2	486
ViSP3	525
VTF	630
DL-VIS	854
DL-NIR1	1083
DL-NIR2	1565
VBI-blue	393
VBI-Red	656

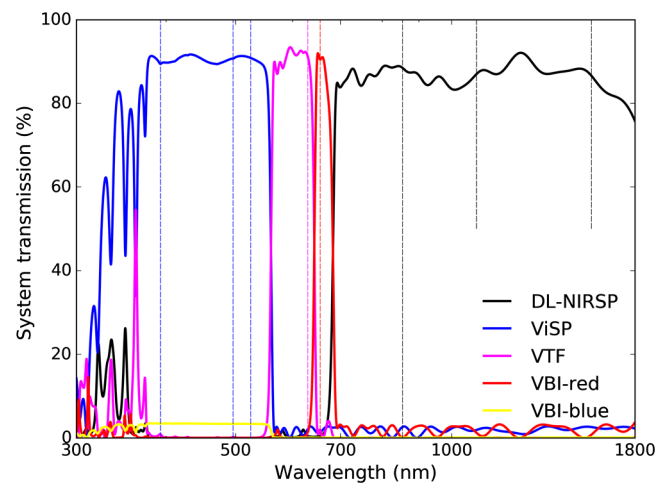


Fig. 40 The flux through combined optics from BS1 the last FIDO element as combined and installed for FIDO configuration 3. The optical throughput delivered to the first feed optic of each subsystem is shown in different colors.

A highly transparent FIDO window C-W3 is installed in station CL4. The DL-NIRSP would thus receive all wavelengths from 680 nm to the cutoff of the Infrasil transmission near 3000-nm wavelength. The antireflection coatings and dichroics all become fairly reflective for wavelengths longer than 1800 nm. We configure DL-NIRSP in Table 13 for observation at 854 nm using the visible wavelengths camera. We set the two NIR cameras to 1083 and 1565 nm.

Figure 40 shows the BS1 and FIDO optics throughput to the first instrument optic. We show throughput in the UV bandpass as this is important for calculating the optical degradation in polymer optics and the oils used in the crystal modulators. The ViSP feed is shown in blue, receiving roughly 90% of the flux from 390- to 540-nm wavelength. The VBI blue channel is shown in yellow, receiving only a few percent of the flux over a similar bandpass. The VTF feed is shown in magenta with roughly 90% of the flux in the 565- to 630-nm wavelength. The VBI red system is shown in red and receives 90% of the flux at 656 nm wavelength to observe the H_{α} line. The DL-NIRSP is shown in black receiving light at wavelengths longer than 690 nm. From Fig. 40, we can also see that no instrument sees more than a few percent of the flux at longer wavelengths outside the intended bandpass. The VTF, DL-NIRSP, and VBI-red channels do receive some UV flux at varying wavelengths depending on the imperfect UV reflectivity of the combined optics.

Figure 41 shows the retardance and diattenuation in the beam propagated through BS1 and the FIDO optics as configured for this use case. The left graphic shows the appropriate wavelength range for the beam to the first lens of the VTF. In this configuration, the VTF would only be observing the 630-nm spectral line. The right-hand graphic shows the beam sent to the DL-NIRSP first-fold mirror DL-FM1. We listed three wavelengths of 854, 1083, and 1565 nm. However, this configuration could easily support other DL-NIRSP configurations for any wavelength longer than 690 nm.

The VTF mirrors have not yet been coated but the nominal specified coating is the same as the GREGOR telescope mirrors. We show our NLSP measurements and two-layer model fits to this GREGOR coating in Sec. 10.1. The VTF feed mirror polarization response will essentially come from the two combined

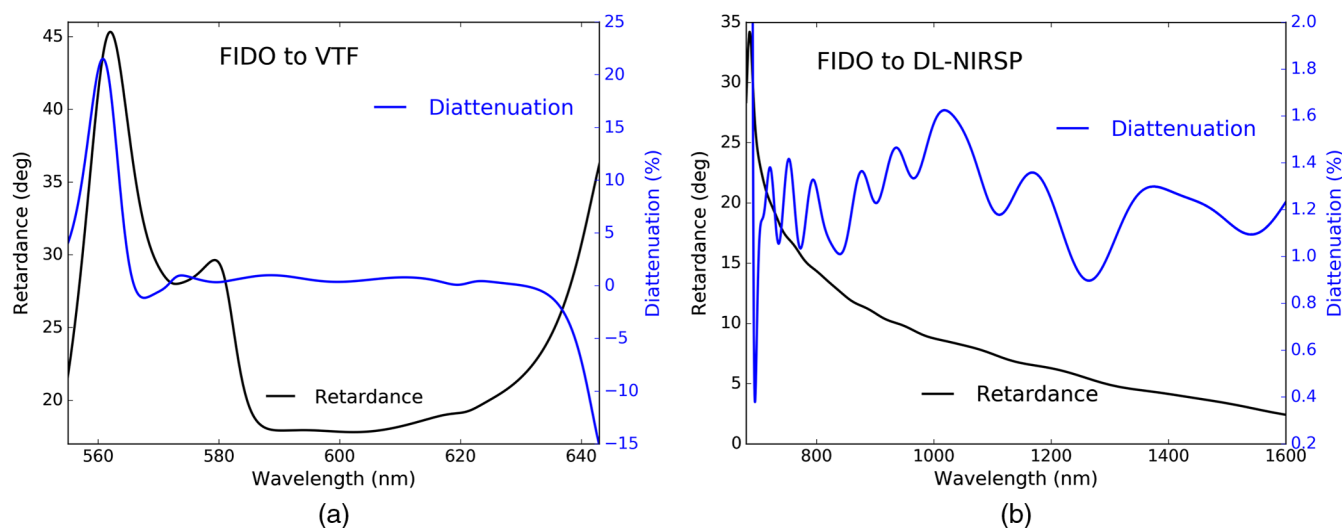


Fig. 41 The retardance in black and diattenuation in blue for the beam through WFS-BS1 and FIDO optics C-BS-555, C-BS-643, C-BS-680, and windows C-W2 and C-W3 as combined for FIDO configuration 3. (a) Shows the combined polarization response of the beam to VTF in the band for observation at 630 nm. (b) Shows the full wavelength range available to DL-NIRSP in this configuration from 700 to 1600 nm.

fold mirrors at 45-deg incidence. The ~ 20 deg retardance and zero diattenuation from FIDO in Fig. 41 will likely be only a small contribution to the modulation matrix properties. For DL-NIRSP, we draw the same conclusions as in Sec. 6.2.

6.4 Summary: Mueller Matrices of DKIST Instruments: FIDO and Coudé Optics

In Sec. 6, we have presented models of the DKIST mirrors grouped together between rotation axes for the on-axis beam. We have shown how typical manufacturing tolerance errors can impact reflectivity, retardance, and diattenuation. Variation directly follows the layer thickness variation derived from two-layer model fits to our NLSP measurements. We have then shown examples of the additional polarization effects from mirror combinations in two DKIST instruments: ViSP and DL-NIRSP. In the case of DL-NIRSP, the nominal DKIST silver formula coated on several high incidence angle mirrors creates significant variability in the expected polarization properties in response to manufacturing variability even though all mirrors have been coated in the same run. In addition, this instrument did not choose the nominal DKIST silver coating for some of their mirrors, complicating the modeling of the entire system. However, the DL-NIRSP mirrors measured in Sec. 10.7 showed that their alternate coating is broadly similar to the DKIST silver in magnitude and spectral smoothness of polarization properties. For the ViSP instrument optics of Sec. 6.1, the original specification of a highly enhanced 29-layer coating on the feed mirrors would have significantly complicated the spectral behavior. We have estimated the reflectivity, diattenuation, and retardance using a combination of vendor reflectivity and diattenuation, vendor modeling, and NLSP retardance measurements. We were able to predict the Mueller matrix of these combined optics had they not been stripped and recoated with one of our nominal FIDO-enhanced protected silver coatings. We note that the Cryo-NIRSP uses an all-reflective feed by inserting a mirror (M9a) in front of the AO deformable mirror (DM) at a low incidence angle of 9 deg and with this same FIDO EA coating.

The two other Cryo-NIRSP feed mirrors are at very low incidence angles of 4 deg and 1 deg. Thus, the polarization properties of the Cryo-NIRSP feed optics are substantially simplified compared to DL-NIRSP. In addition, the VTF feed mirrors are essentially twofold mirrors around 45 deg. They are clocked with respect to the coudé floor, introducing both QV and UV retardance in the frame of their analyzer. But this is similar to DL-NIRSP, predictable with witness sample data, and easily calibrated. With this information, and a few more coating samples delivered in the near future, we have the Mueller matrix of every metal-coated optic in the telescope and on the coudé floor.

We then showed examples of how the dichroics of the FIDO could be configured for two use cases. The first configuration of Sec. 6.2 shows maximum transmission to DL-NIRSP with relatively simple and spectrally smooth Mueller matrices. In Sec. 6.3, we add the complexity of operating polarimeters in all AO-assisted instruments simultaneously. FIDO is configured for ViSP from 380 to 555 nm, the VTF at 630 nm and DL-NIRSP from 680 to 1800 nm. The predicted throughput from the combined reflections and transmissions are shown along with the retardance and diattenuation expected for each system. This process can be used for all DKIST instruments and updated in the future to reflect the as-built coating performance once the FIDO dichroics are procured and we have measured those as-coated witness samples in the near future.

7 Summary

The DKIST project must deliver a stable, polarization-calibrated beam to instruments in the CL. The optical properties of coatings on each optic must be well known in order to predict performance as a function of field angle, telescope configuration, and wavelength at DKIST spectral resolving powers of roughly 100,000. The altitude and azimuth articulations of the telescope, CL table rotation, AO beam splitter along with the windows, mirrors, and dichroics of the FIDO all require measurement and modeling at spectral resolving powers above 10,000 to detect narrow spectral features in many-layered coatings.

Dichroics and highly enhanced mirrors can have complex behavior over the <1 -nm bandpasses of DKIST instrument suite, as we have shown above. The internal optics to each DKIST polarimeter also contribute significantly to the expected polarization performance of the system. We have explored here the metrology tools and system models for DKIST and several instruments using coating witness samples, vendor models, and vendor data. We have measured at least one sample for every mirror within the telescope and coude relay optics and have presented several examples of instrument partner mirrors, beam splitter dichroics, and window antireflection coatings. We have extensively used our NLSP that simultaneously covers visible and NIR wavelengths outlined in Sec. 2. For this paper, we consider only the on-axis beam properties for DKIST, noting that the field dependence for the telescope is as we assessed previously.¹¹ In this prior work, we only used a single nominal silver and aluminum metal coating prescription. With this new work, we can now identify realistic coatings for all mirrors, antireflection coatings, and dichroics that can easily be exported to optical modeling tools for use in predicting performance on powered optics and in articulated systems, as we showed in 2017.¹¹ We have presented an assessment of mirror polarization data from many samples measured with NLSP, in Sec. 3. We achieve statistical SNRs over 10,000 at spectral resolving power of a few hundred along with very high temporal stability over months. The reflective configuration is highly stable. Retardance measurement stability is better than 1 deg retardance after remounting of reflective samples over a year timespan with a complete optical realignment.

We have adapted the Berreman calculus^{14,15} for predicting and fitting a wide variety of polarization behavior of coatings. Here we have presented adaptation of the scripts to fit NLSP Mueller matrix elements for diattenuation and retardance for enhanced protected metallic mirror coatings. We show refractive index curves and associated materials thicknesses used to model diattenuation and retardance with high-quality fits across visible and NIR wavelengths. This lab spectropolarimeter will also be critical for the DKIST project when assessing our upcoming FIDO dichroic and antireflection coatings. We have assessed polarization performance on several DKIST antireflection coating witness samples, in Sec. 4. We have also compared our results with vendor-provided models and reflectivity data from Infinite Optics. The data and model matches are quite good when vendor-provided materials and refractive index data are used in the models.

We then assessed antireflection coatings and dichroic coatings that use many dielectric layers to create wavelength ranges of high reflection and high transmission, in Sec. 5. We have presented here example dichroic formulas and witness-sample measurements from Infinite Optics. We have measured several witness samples with NLSP and compared the results to designs in the industry-standard TFCalc software package as well as verified the output in our Berreman calculus scripts. The measurements of transmission, retardance, and diattenuation agree quite well with the measurements. Fitting for the as-built coating layer thicknesses using transmission data is demonstrated with TFCalc. Polarization predictions using these revised coating designs gives good matches to our NLSP measurements. We have shown examples of polarization properties and reflectivity changing over wavelength ranges smaller than a nanometer. These narrow features are a property of many-layered coatings and were highlighted in Sec. 5.4 and measured with spectral

resolving power of $>20,000$. These narrow features can be significantly mitigated through design. We have presented FIDO coating designs that follow this strategy for DKIST.

System-level models for the DKIST telescope group model and some FIDO configurations are shown in Sec. 6. The impact of manufacturing tolerances is assessed to show that metrology of witness samples is critical for accurate prediction of system performance. The polarization properties of several DKIST instruments are also assessed to create predictions of the instrument Mueller matrices. An example of a 29-layer protected silver mirror is shown for ViSP along with the spectral consequences for using such a coating in the instrument feed optics, in Sec. 6.1. Spectral features as narrow as the nanometer scale instrument bandpasses are present in this coating. These metrology efforts result in stripping and recoating of the ViSP feed mirrors with a new, slightly less reflective but polarimetrically smooth coating presented in Sec. 10.9.

In Sec. 8, we show the current coating status of every surface between the primary mirror and the instrument modulators. Many dichroics are not yet coated, but essentially all mirrors except the instrument VTF are now complete. In Sec. 10, we show data on several commercial mirrors and witness samples used in DKIST along with fits to a range of two-layer coating material models. These largely fell into two groups of high-index over low-index and low-index over high-index, as is in standard coating recipe textbooks. Our models ignore several aspects of real coatings, including use of strippable layers, fabrication processes, textured growth, and refractive index variation with depth and layer. However, the simple polarization models presented here for coating performance with wavelength and incidence angle can be quite useful for simulating system polarization performance. Using thin film modeling software such as TFCalc or optical modeling in Zemax or other ray-tracing programs can give predictions and assess manufacturing tolerances, even if the materials modeled do not correspond to those of the actual coating.

There are several opportunities for extension of this work. We only present NLSP data at 45-deg incidence angles but are not limited to this single configuration. Adding variable incidence angles as well as common image rotator (K -cell, K -mirror)-type reflectivity configurations, as shown in Sec. 10, provides a straightforward path for future work on fitting additional coating properties. We have identified several variables with large impact such as metal layer complex refractive index and modified refractive index spectral behavior as well as assessing coating polarization model fidelity over a wide range of incidence angles (Secs. 3.1 and 10). Future work includes expanding the spatial variation of coatings described in Sec. 5.1 and the field-of-view dependence in our prior publication HS17¹⁶ to predict the polarization calibration limits of the system across the diverse wide-field scanning techniques intended for use at DKIST.

8 Appendix A: DKIST Coating Status: Mirrors, Dichroics, and Windows

Tables 14 and 15 show the current status of DKIST mirrors and coatings in the DKIST optics and within the initial polarimetric instruments. We show the name of the various optics in column one. Column two shows their incidence angle, or a range of angles for powered optics. The third column shows the focal ratio ($F/\#$) for the beam at that optic. Optics denoted (OA) are off-axis mirrors. The fourth column shows the coating name.

Table 14 DKIST mirrors, incidence angles, and coating status.

Optic	AOI	Power	Coating	Provider	Run	Sample?
M1	7.13 to 20.56	<i>F/2</i> OA	Al	AFRL		Yes (2)
M1 spare	7.13 to 20.56	<i>F/2</i> OA	Al	AFRL		Yes (2)
M2	6.03 to 17.27	<i>F/13</i> OA	D.EAG	—	13BE18	Yes (2)
M3	42.81 to 47.19	Flat	D.EAG	—	14BE04	Yes
M4	0.93 to 2.57	<i>F/53</i> OA	D.EAG	—	15BA35	Yes (2 + 1)
M5	14.47 to 15.53	Flat	D.EAG	—	12BD18	Yes
M5 spare	14.47 to 15.53	Flat	D.EAG	—	12BD19	Yes
M6	29.47 to 30.53	Flat	D.EAG	—	14BE05	Yes
M6 spare	29.47 to 30.53	Flat	D.EAG	—	14BE04	Yes
M7	44.47 to 45.53	Flat	D.EAG	—	16BD16	Yes
M8	5.06 to 5.60	<i>F/53</i> OA	bAG99	EMF	Unlabeled	Yes (3)
M9	10	Flat	EAg1-450	IOI	9-3095	Yes (3)
M10 DM	15	Flat	D.EAG	—	15BA23	Yes (4)
WFS-BS1-f	15	Flat	none	—		Uncoated
WFS-BS1-b	14.5	Flat	WBBAR1	IOI	10-0233	Coming
FIDO	Mirror					
C-M1	15	Flat	EAg1-420	IOI	6-7766	Yes, 3
C-M2	15	Flat	EAg1-450	IOI		Not yet coated
FIDO	Dichroic					
C-BS-465-f	15	Flat	Dich465	IOI		Not yet coated
C-BS-465-b	14.5	Flat	WBBAR1	IOI		Not yet coated
C-BS-555-f	15	Flat	Dich555	IOI		Not yet coated
C-BS-555-b	14.5	Flat	WBBAR1	IOI		Not yet coated
C-BS-643-f	15	Flat	Dich643	IOI		Not yet coated
C-BS-643-b	14.5	Flat	WBBAR2	IOI		Not yet coated
C-BS-680-f	15	Flat	Dich680	IOI		Not yet coated
C-BS-680-b	14.5	Flat	WBBAR2	IOI		Not yet coated
C-BS-950-f	15	Flat	Dich950	IOI		Not yet coated
C-BS-950-b	14.5	Flat	WBBAR2	IOI		Not yet coated
FIDO	Window					
C-BS-W1-f	15	Flat	WBBAR1	IOI		Not yet coated
C-BS-W1-b	14.5	Flat	WBBAR1	IOI		Not yet coated
C-BS-W2-f	15	Flat	None			Uncoated
C-BS-W2-b	14.5	Flat	WBBAR1	IOI		Not yet coated
C-BS-W3-f	15	Flat	WBBAR1	IOI		Not yet coated
C-BS-W3-b	14.5	Flat	WBBAR1	IOI		Not yet coated

Table 15 DKIST instrument mirrors, incidence angles, and coatings.

Optic	AOI	Power	Coating	Provider	Run	Sample?
ViSP						
V-FoldM1	28	Sph	EAg1-420	IOI	6-7767	Yes, 3
V-Feed1	2.2	Sph	EAg1-420	IOI	6-7766	Yes, 3
V-Feed2	12.3	Sph	EAg1-420	IOI	6-7767	Yes, 3
Slit glass-f	5.4	Flat	BBAR	ECI	Unknown	No, graphed
Slit glass-b	5.4	Flat	BBAR	ECI	Unknown	No, graphed
V-FoldM2	47.7	Flat	EAg	RMI	Y31071216	No
Modulator	0	Flat	MgF ₂	MLO		Yes
V-FoldM3	45	Flat	EAg	RMI	Y31121216	No
V-FoldM4	45	Flat	EAg	RMI	Y31121216	No
ViSP	Old	Stripped	29 layer			Yes, 2
Cryo-NIRSP						
M9a	9	Flat	EAg	Zygo	G4194725	Yes, 5 (Unif)
Scan	4	Flat	D.EAG	—	16BB07	Yes, FM1, CN-OPT-0001
Foc	1.13	OAP	D.EAG	—	16BB21	Yes, FM2, CN-OPT-0002
Modulator	0	Flat	None	MLO	—	—
Slit						
Filter						
SM2 Fold1	5.5	F/18 Flat	D.EAG	—	16BB07	Yes, CN-OPT-0003
SM3 Col	5.5	F/18 OAH	D.EAG	—	16BB21	Yes, CN-OPT-0004
SM4 Fold2	7	Flat	D.EAG	—	16BB07	Yes, CN-OPT-0005
Grating	Var	Flat	Al	Newport	—	
SM5 Cam	7.7	F/8 OAE	D.EAG	—	16BD15?	Yes, CN-OPT-0006
DL-NIRSP						
DL-FM1	45	Flat	EAg	Zygo	G4194726	Yes, 1 (& 5 test -28)
DLF-OAM1	7	OAh	D.EAG	—	16BE17	Yes, F00-102, 400mm
DLF-FM2	45	Flat	D.EAG	—	16BB22	No but verify DL-207
DLF-FM3	45	Flat	D.EAG	—	16BB22	No but verify DL-207
DLF-FSM	3.8	Sph	D.EAG	—	Unknown	No F00-105, 220 mm
F/ 24 & F/ 8						
DLF-MF24	4.4	OAe	D.EAG	—	16BE16	Yes, F00-106, 250 mm
DLF-M4	49.7	Flat	D.EAG	—	16BB22	No but verify DL-207
Modulator	0	Flat	BBAR	IOI	12-6523	Yes
F/62						
DLF-MF62-1	3.3	OAe	EAg	Unkn	Unknown	No , F00-108, 230 mm
DLF-MF62-2	4.9	OAe	D.EAG	—	16BE17	Yes, F00-109
DLF-M4	45.9	Flat	D.EAG	—	16BB22	No but verify DL-207
Modulator	0	Flat	BBAR	IOI	12-6523	Yes
VTF	SAMP		EAG	Tafelmaier		Yes

Column five names the coating vendor where available. Column six shows the coating run number as many optics were combined into single coating shots. The seventh column shows current status of witness samples and the quantity we have from each run. D.EAG denotes the specified enhanced protected silver within the DKIST project. Otherwise, EAg is shorthand for Enhanced protected silver (Ag). Vendors include IOI, Zygo Corporation, and Dynasil's EMF. The AFRL has a coating chamber adjacent to DKIST on the summit of Haleakala used for the DKIST primary mirror. We also have samples from Tafelmaier used by the GREGOR solar telescope with the intended formula to be applied to optics not yet coated within the DKIST VTF instrument. In some cases, we did not receive sufficient documentation to specifically attribute a coating run to a specific optic. For DL-NIRSP, we are able to test some of the small flat mirrors directly in NLSP. For the beam splitters in FIDO and the AO system, we show front side and back side coatings as $-f$ and $-b$, respectively. We do not list the three FIDO windows described in Sec. 4 that will be coated with WBBAR1 or left uncoated. We also do not list the five dichroic coatings of FIDO described in Sec. 5 as they also have not yet been coated. We have currently completed several coating stress, uniformity, and repeatability tests for the dichroic coating formulas and anticipate a more thorough study in the coming year.

9 Appendix B: NLSP Calibration and Optical Stability

The NLSP measured Mueller matrix using the visible spectrograph for four samples are shown in Fig. 42. A DKIST silver witness sample from one coating of the telescope feed optics is shown in red. Witness samples from Infinite Optics tested as part of the FIDO mirror process are also shown in black, green, and blue. These witness samples use a few different materials and are provided for polarization comparison between NLSP, the Infinite Optics metrology equipment, and theoretical calculations. We note that we use the industry-standard TFCalc, the Zemax optical design software, as well as our Python-based Berreman calculus scripts, which all agree to numerical precision when we have checked against known coatings and crystals.^{11,16,66}

The NLSP reflective setup gives retardance results consistent within roughly 1 deg when perturbed by remounting samples over days to a year. We frequently remount samples to repeat measurements using various calibrations as a test of our systematic error levels. As an example, Fig. 43 shows retardance measurements made after unmounting and remounting the sample 24 h later. The left-hand graphic shows the difference between the fit retardance values. Different curves show the changes

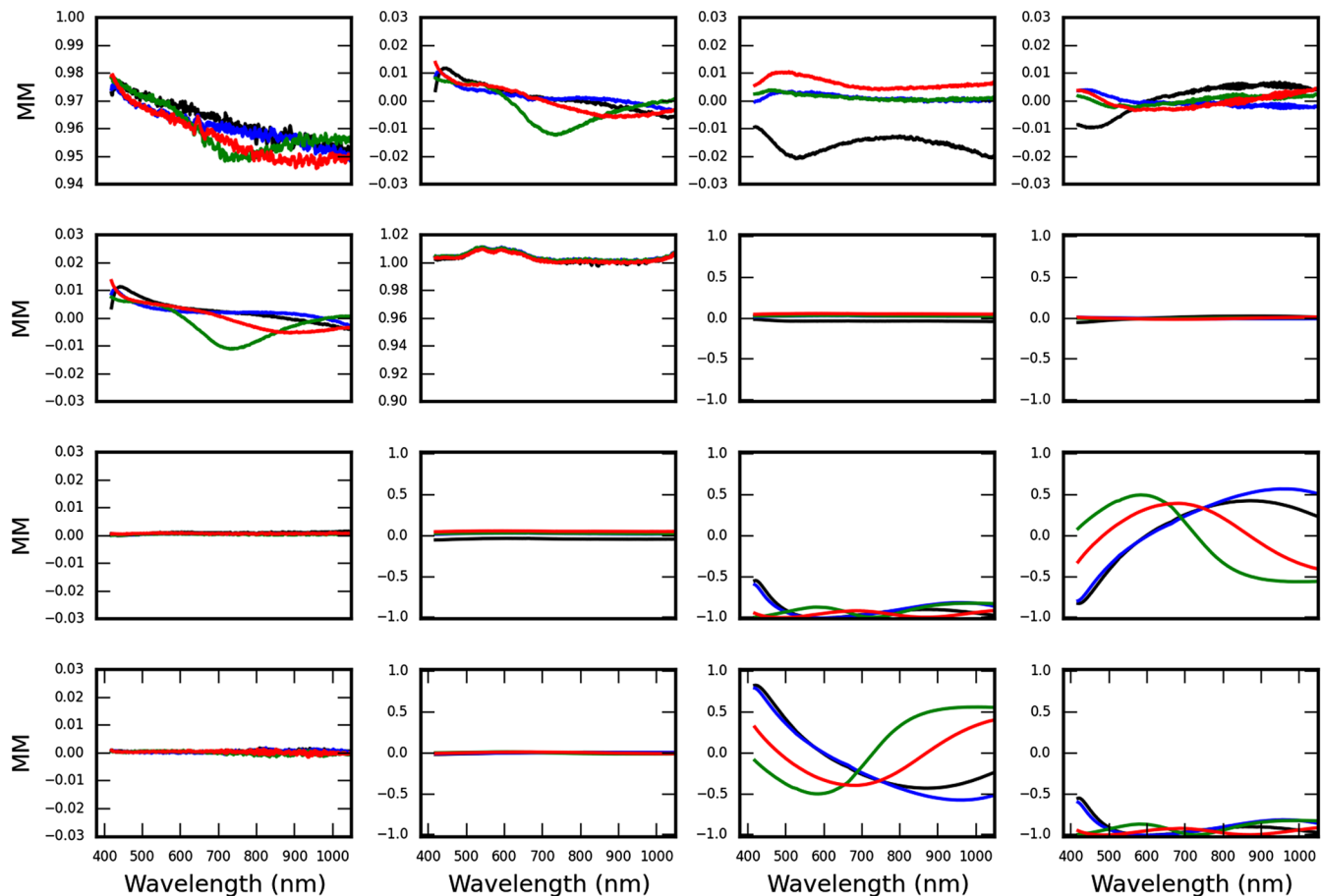


Fig. 42 The NLSP-measured Mueller matrix for a DKIST-enhanced protected silver mirror sample as well as the three Infinite Optics mirror samples tested for the DKIST FIDO optics. Reflection is at 45-deg incidence angle and we show only visible spectrograph data here for clarity. Red shows the DKIST-enhanced protected silver mirror. Black shows the IO EAG300 5-5033 sample. Green shows the IO EAG700 8-6282 sample. Blue shows the IO EAG450 8-6898 sample. The data have been normalized as in Eq. (8).

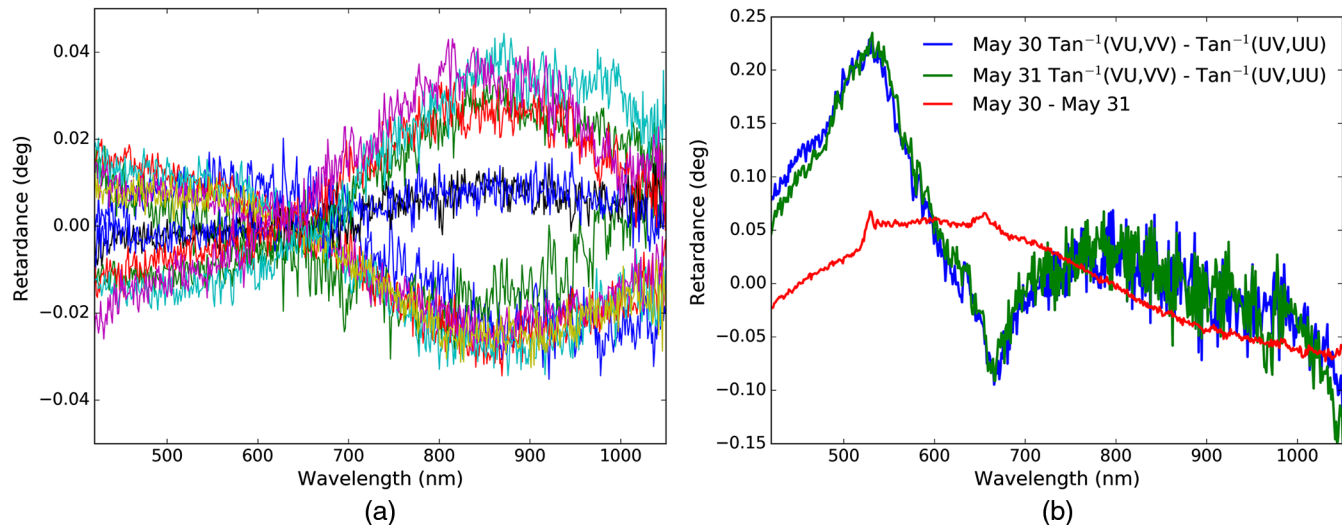


Fig. 43 (a) Shows retardance changes between data sets taken on the same day. Variation is <0.05 deg retardance. (b) Shows a comparison of retardance measurements taken on May 30 and May 31. The change between days is shown as the red curve and is <0.06 deg peak to peak. However, the biggest systematic difference is in the Mueller matrix being not entirely physical. For retardance, the UU, UV, VU, VV elements should all be sin or cos of the retardance magnitude. As such, any estimate computed as an inverse tangent of the appropriate Mueller matrix elements should give an identical retardance value. The retardance values estimated using $\arctan(VU, VV)$ does not agree with $\arctan(UV, UU)$ at amplitudes of up to 0.2-deg retardance. This is a small disagreement but it does show that systematic errors are a few times larger than repeatability errors.

between various inverse tangent methods of computing retardance from the Mueller matrix. The beam footprints are not identical on the optic nor are the optical alignments guaranteed to be exact. The individual estimates of retardance agree between subsequent remounting at levels of 0.05 deg or below. In the right-hand plot, we see the difference between the retardance estimates using different Mueller matrix elements in an inverse tangent computation. The theoretical Eq. (13) says the various inverse tangents of the various UV elements should produce identical retardance values. However, we see variation at amplitudes of ± 0.15 deg retardance with an offset of roughly 0.05 deg on average as the green and blue curves in the right-hand graphic of Fig. 43. We also include in that graphic the difference between May 30 and May 31 measurements as the red curve, which is a factor of a few less than the error between the different inverse tangent estimates. The alignment procedures produce highly repeatable measurements at levels less than one-tenth of a degree.

Strong arguments can be made about requiring any data-derived Mueller matrix to be physical by imposing a process to relate the measured matrix to be the nearest physical Mueller matrix using an appropriate distance metric.^{64,70,71–80} Our matrix measurements are stable and produce retardance measurements that vary by <0.2 deg when comparing different inverse tangent estimates of the UV, VU, VV , and UU elements. For the sake of simplicity, we choose the average of the inverse tangent estimates of retardance and proceed with the analysis. As seen in the right graphic of Fig. 43, the two estimates we chose sample all four U and V Mueller matrix cross talk elements. We average the two retardance estimates as a very straightforward, simple procedure.

Retardance and diattenuation measurements are very stable over months with statistical SNRs over 10,000. Figure 44 shows an example measurement of retardance and diattenuation for an enhanced protected silver mirror coating witness sample in

May 2017 in the left graphic. The retardance and diattenuation are derived from the NLSP-measured Mueller matrix of a DKIST-enhanced protected silver witness sample reflecting at 45-deg incidence angle. A slight discontinuity can be seen at 1020-nm wavelength as well as a change in the statistical noise properties. This is the wavelength we have chosen to switch from visible-to-NIR data sets. The black curve shows the retardance in the range of 150 deg to over 200 deg where a retardance free mirror would give a phase change of 180 deg. The blue curve shows the diattenuation in the range from -1.4% to $+0.5\%$.

The right-hand graph of Fig. 44 shows the difference between retardance and diattenuation when internal calibrations are used from May to calibrate a July data set, compared with calibrations taken within 24 h of measurement in July. The input retardance ranges over 50 deg over this bandpass but the results are repeatable to better than 0.002 deg peak to peak. Diattenuation results vary more but are still stable. We see -1% to $+0.5\%$ diattenuation in this sample, but using different calibrations the results are offset by roughly 0.15% and range spectrally from this offset by 0.2%.

Though the NLSP reflective system calibrations are stable, a larger effect is seen when mounting the same sample in a different mount after an optical realignment of the system. The left-hand graphic of Fig. 45 shows the difference between retardance measurements when samples were remounted with a day or few in September 2018. The optical realignment procedure has been performed and data analysis done with identical calibration files. The difference in retardance is always below 1 deg with most values within ± 0.5 deg. The right-hand graphic of Fig. 45 shows how the retardance varies between summer 2017 and September 2018 for samples from various telescopes and vendors. In this case, we observe variations up to 1.5 deg magnitude. The optical alignment and derived retardance results are stable to degree magnitude over timescales of days to years.

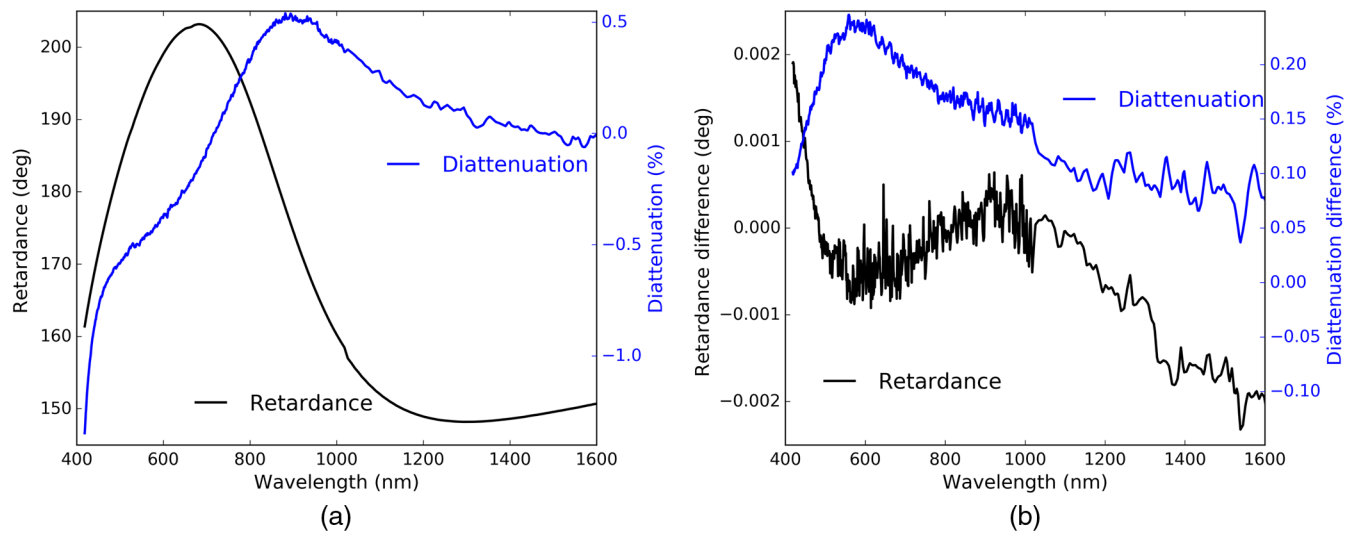


Fig. 44 (a) Shows NLSP-processed retardance and diattenuation measured at 45-deg incidence angle with both VIS and NIR spectrographs for a DKIST-enhanced protected silver witness sample. NLSP data are recorded from 380 to 1650 nm. The VIS and NIR spectrograph data sets show good overlap and are subsequently stitched together at a crossover wavelength of 1020 nm. (b) Shows the difference between retardance and diattenuation when internal calibrations from three months prior are used instead of same-day calibrations. Retardance is in black on the left-hand y axis. Diattenuation is in blue on the right-hand y axis.

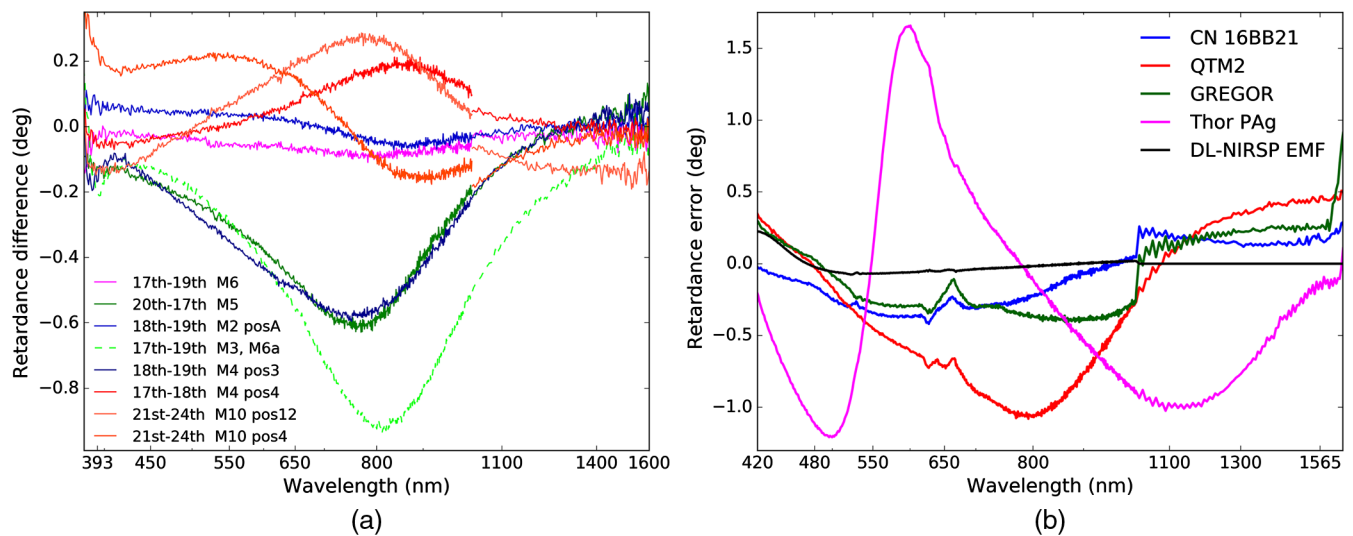


Fig. 45 The difference between retardance measurements over time. (a) Shows retardance changes between several DKIST EAg data sets taken in the September 2018 run. Variation is <1-deg retardance. (b) Shows a similar repeatability test but comparing retardance variation over a year between samples of many different silver coating formulas.

We show an example of the robustness of the NLSP retardance measurements to sample tilt and mounting errors in the left panel of Fig. 46. We compare predictions of the best-fit two-layer coating Berreman models to measurements. The blue curve shows the DL-NIRSP-1 sample retardance measurement that is significantly different from the DKIST sample. The black curves show how the best-fit Berreman model predictions change for tilts ± 1 deg about the nominal 45-deg incidence angle. When new samples are mounted in NLSP, there is some mechanical error in the manual positioning of the sample depending on what kinematic mounts are used. The Berreman models in Fig. 46 change magnitude

at certain wavelengths, but the black curves generally do not shift wavelength. In particular, the wavelength of the theoretical 180-deg retardance is almost completely insensitive to incidence angle errors. We also show example diattenuation differences as well as tilt sensitivity in the right-hand graphic of Fig. 46. We show the same NLSP measurements for the DL-NIRSP-1 sample in blue along with the tilt sensitivity of the best-fit two-layer Berreman model in black. In addition, we show the NLSP measurements for the DKIST evaluation sample in red. Diattenuation is not presently fit in our current coating model so we do not anticipate a high-quality match.

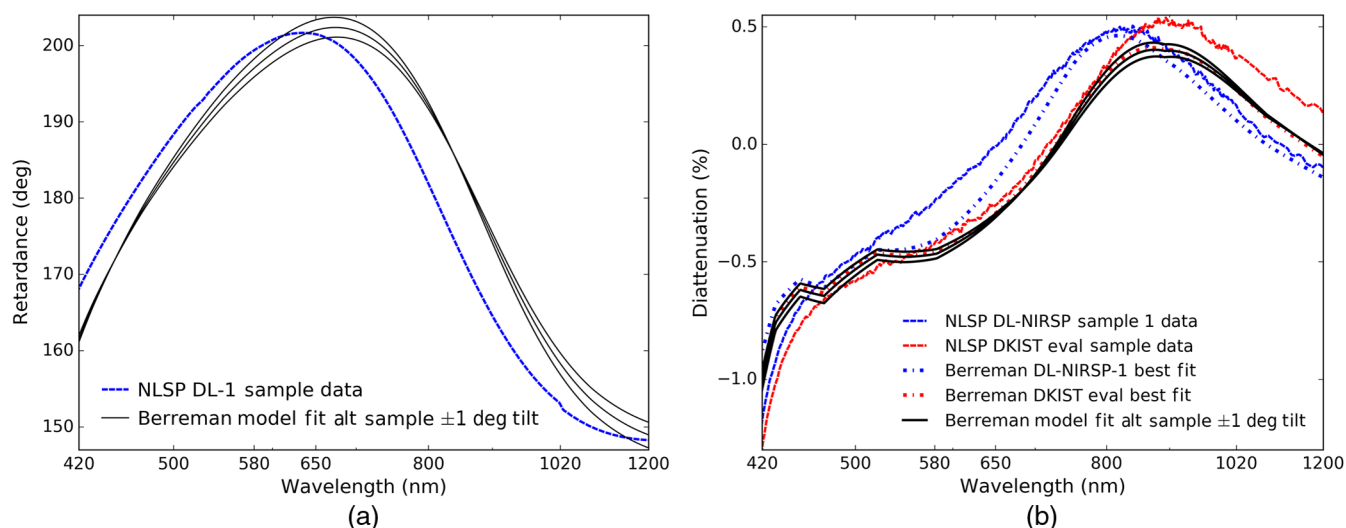


Fig. 46 (a) Shows a comparison of our retardance measurement sensitivity to tilt. Two significantly different retardance curves are selected: a DKIST evaluation sample and the DL-NIRSP 1 sample. The NLSP data for the DL-1 sample are shown in dashed blue. The Berreman models shown in black represent the best-fit coating formula to retardance of the DKIST evaluation sample with change in predicted retardance from a ± 1 deg mounting tilt error. The black curves are significantly displaced in wavelength, showing tilt does not explain the shot-to-shot variations in our measurements. (b) Shows a similar tilt sensitivity analysis for diattenuation.

The diattenuation measurements are not repeatable at the level of roughly 0.2%. In addition to a constant offset of 0.15% there are spectral differences of $\pm 0.1\%$. Thus, we consider the systematic errors on diattenuation to be at magnitudes of at least this level. However, the diattenuation tilt sensitivity of Fig. 46 is much smaller than these magnitudes as seen by the black curves. In addition, the two separate two-layer coating models show that both spectral shifts and magnitude changes are expected. The right-hand plot of Fig. 46 shows the diattenuation models overplotted as the dot-dashed lines. The spectral shifts between blue and red curves are largely explained by thickness variations of the two dielectric layers in our coating model. The diattenuation measurements seem to be more sensitive to the optical alignment of the samples and are the main limiting error at this time. In Fig. 47, we show the diattenuation for several DKIST silver samples recorded in the same campaign shown above in Fig. 5. We also show the nominal diattenuation prediction derived from vendor S and P reflectivity as the dot-dash magenta line. We do expect coatings to vary significantly run to run as shown in our tolerance analysis, but the offsets of some fraction of a percent in Figs. 47 and 44 are significant and so far unpredictable.

To verify that we can predict system-level polarization for DKIST with combinations of multiple mirrors, we have introduced a three-mirror K -cell (image rotator)-type setup into our lab spectropolarimeter. We combine threefold mirrors which nominally preserve the beam translation and tilt to verify the model predictions using the better-calibrated transmission arm of NLSP for testing a combination of DKIST-enhanced silver mirrors. In Fig. 48, we show the K -cell data for three mirrors at incidence angles of roughly 50 deg, 10 deg, and 50 deg. Each mirror has different properties that are included in the model. We take the nominal retardance-only two-layer coating model fits as the starting point. The first mirror is 11.975 nm ZnS over 103.1 nm Al_2O_3 . The second mirror is 8.925 nm ZnS over 109.4 Al_2O_3 . The third mirror is 9.975 nm ZnS over

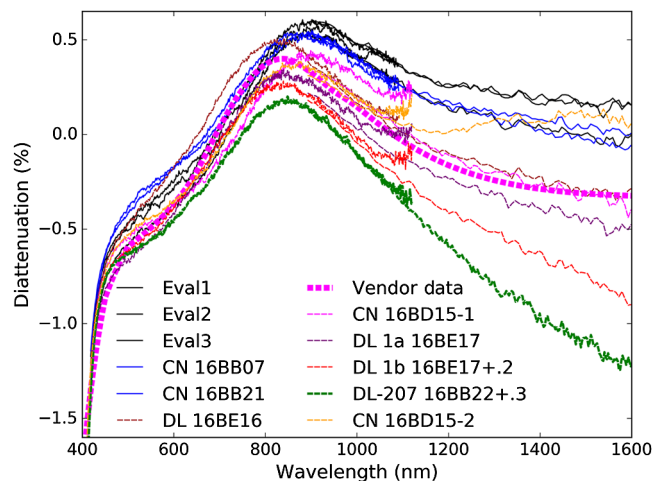


Fig. 47 Diattenuation measured for NLSP samples is strongly rising from -3% at 393-nm wavelengths to $+0.5\%$ around 850 nm, then decreasing toward values of -0.5% to $+0.2\%$ at 1650 nm. Vendor data are shown as thick dashed magenta.

101.4 nm Al_2O_3 . We show the impact of fitting errors by allowing the top layer to vary by ± 0.5 nm and the bottom layer to vary by ± 1.5 nm independently for each mirror in the K -cell. This gives rise to three thicknesses for two layers in three mirrors giving a total of 18 models per K -cell configuration.

We also show the impact of incidence angle by allowing a 5-mm error in measuring the spatial positioning of the beam along with the requirement that the K -cell be aligned geometrically. We measured the long axis of the K -cell to be 83 mm, while the short axis is 26 mm. The equations for a perfectly aligned K -cell give the small interior angle as the arctangent of the two distances. The triangles must all sum to 180-deg interior angles and thus the exterior fold angle is $(90 \text{ deg} + \text{interior angle})/2$. We estimate that the smallest fold angles

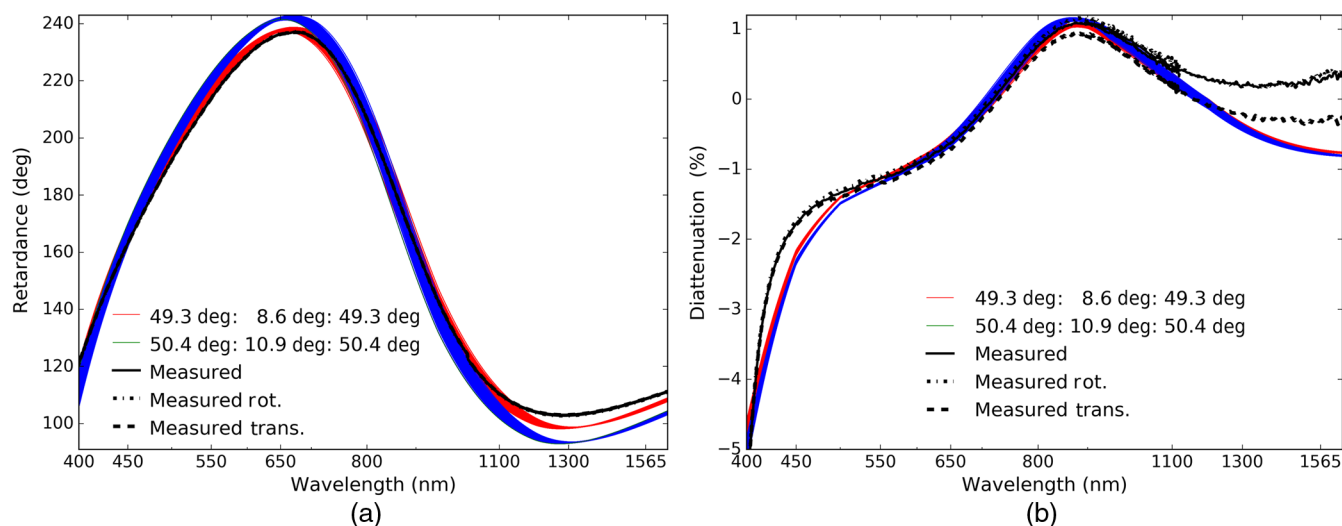


Fig. 48 The K -cell retardance measurements and model for the DKIST-enhanced silver mirrors. Individual colors show families of coating model predictions following the perturbation of ± 0.5 nm in the top layer and ± 1.5 nm in the bottom layer (3^2 models for three mirrors). Different colors represent different incidence angles. The black lines show NLSP measurements with some perturbations in K -cell orientation and spatial position.

would be 49.3 deg:8.6 deg:49.3 deg. The predicted three-mirror retardance is shown by the red curves on the left in Fig. 48. Diattenuation is shown on the right. If we add the 5-mm perturbation to increase the angles, we would get 50.4 deg:10.9 deg:50.4 deg, as shown by the blue curves in Fig. 48.

Each family of colored curves in Fig. 48 shows the range of coating formula layer thicknesses. Clearly, the impact of incidence angle is stronger than the coating layer thickness for this geometric measurement uncertainty. The black curves show the retardance derived from the NLSP Mueller matrix measurements. We tried a few different optical alignment perturbations by rotating and translating the sample. The data match the smaller incidence angle predictions best while slightly underpredicting retardance around 1400-nm wavelength. Given the close match, we have reasonable confidence that we can predict the system model retardance to similar tolerances.

We have shown that NLSP can repeatably measure retardance to values < 0.05 deg when remounting identical samples without a perturbation in the optical alignment. The retardance calculations from the UU , UV , VU , and VV Mueller matrix elements are self-consistent to better than 0.25-deg magnitudes within a single data set. When remounting and recalibrating the same sample on different days with a possibly perturbed optical alignment, we compute the same retardance within roughly 0.5 deg with spectral dependence well above statistical noise limits. The same samples repeatedly measured over a year show magnitude variation of up to ± 1.5 deg depending on the quality of the optical alignment. When using system calibrations taken months apart, the diattenuation changes by 0.15% in absolute offset with some spectral dependence at 0.1% magnitudes.

We also showed examples of reflective polarization measurements for several DKIST-enhanced protected silver samples and how the measurement setup is insensitive to tilt errors in the sample mounting. Measured variation within witness samples is very significant compared to NLSP systematic error limits. The reflective arm of NLSP is very capable of measuring sample retardance and diattenuation.

10 Appendix C: Mirror Examples and Coating Model Fitting

Though common software programs provide some nominal refractive indices for common materials, the data often poorly capture wavelength dependence. The uncertainty in wavelength dependence of material properties is one of the major limitations in predicting polarization performance significantly better than 1 deg retardance. Figure 49 shows example refractive index curves gathered from the common coating modeling tools in TFCalc and Zemax, as well as online references in the RefractiveIndex.info database.

The upper left plot shows zinc sulfide (ZnS) where the RefractiveIndex.info database gives a dispersion formula of Eq. (11) based on two references. The black curve shows the Zemax coating file likely performs a linear interpolation of this curve with wavelengths of 400, 460, 500, 700, 800, 1000, and 2000 nm. The TFCalc software package gives only a single refractive index of 2.3 at a wavelength of 550 nm

$$n^2 = 8.393 + \frac{0.14383}{\lambda^2 - 0.2421^2} + \frac{4430.99}{\lambda^2 - 36.71^2}, \quad (11)$$

$$n^2 - 1 = \frac{0.6961663\lambda^2}{\lambda^2 - 0.0684043^2} + \frac{0.4079426\lambda^2}{\lambda^2 - 0.1162414^2} + \frac{0.8974794\lambda^2}{\lambda^2 - 9.896161^2}. \quad (12)$$

The upper right graphic shows SiO_2 for the RefractiveIndex.info database in solid blue as well as the TFCalc coating properties in dashed red with good agreement. Interpolation wavelengths for both curves are 300, 350, 400, 450, 500, 550, 600, 650, 700, 900, 1000, and 2000 nm. Equation (12) is also shown in green, as published in the RefractiveIndex.info database, and is in the CVI Melles Griot catalog. In the lower two graphics, we show common coating materials of HfO_2 and TiO_2 . A technique used in fitting refractive indices is to scale or offset the refractive index equation by some

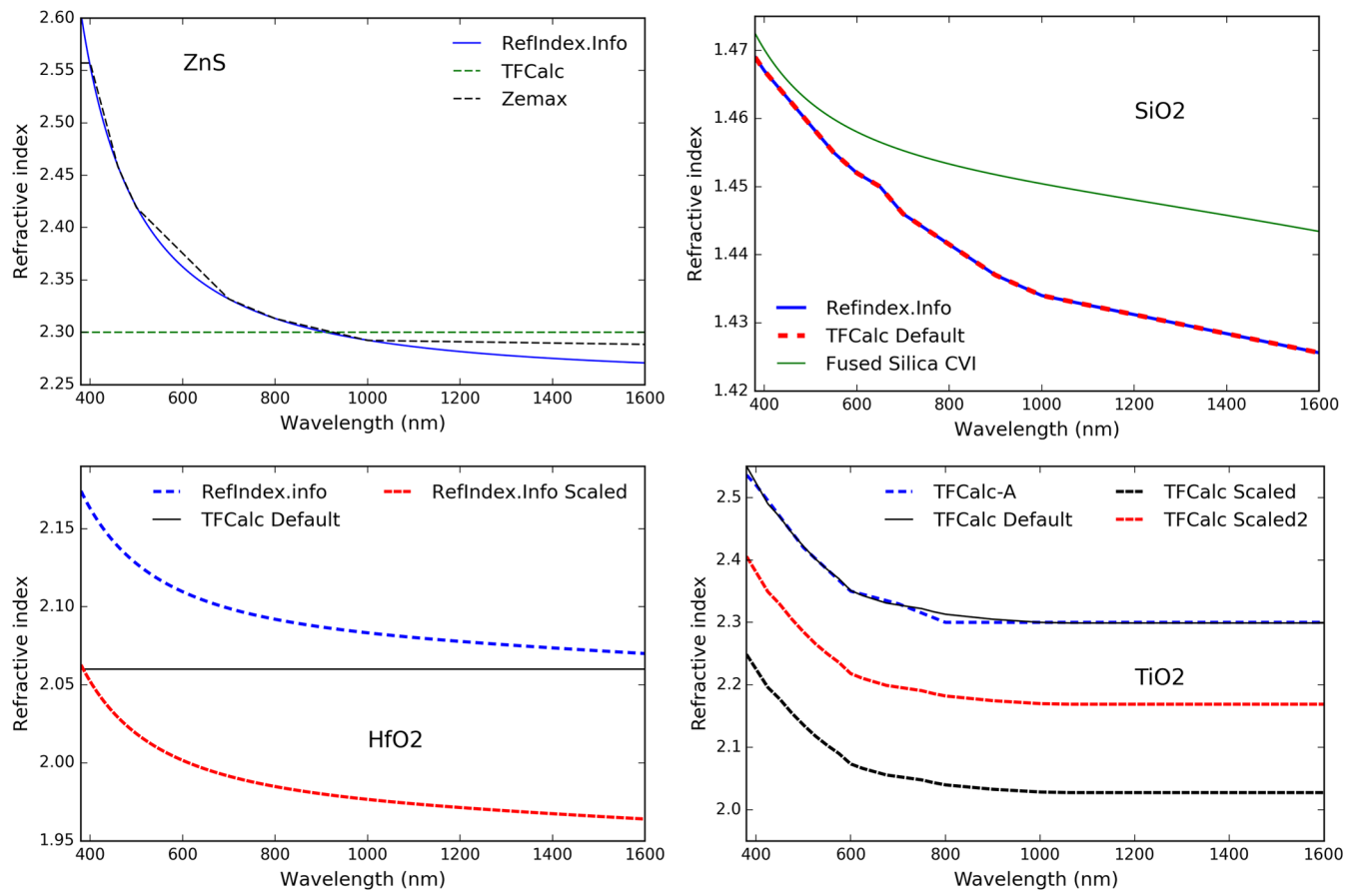


Fig. 49 The refractive indices for common coating materials. Common RefractiveIndex.info website data are shown along with data from the Zemax coating file provided with version 16.5, 2016 and the TFCalc default material files where applicable.

constant. For HfO₂ and TiO₂ we show curves that are scaled by 5% to 20%.

Often vendors for lower cost off-the-shelf parts will only provide limited information about the polarization performance of the mirrors, if any. A common scenario is to be given a theoretical model for reflectivity and possibly diattenuation with coarsely sampled, roughly interpolated spectral data. When attempting to fit coating performance models to these data sets, we have often found that the models are easily reproduced with publicly available refractive index information with additional adjustments or interpolation. As an example, we show here models for a coating, which is described as a single dielectric layer protecting aluminum metal. The coating has been described by the vendor as a quarter wave of silicon monoxide-protecting aluminum. We also had explicit follow-up communications that silicon dioxide was not correct, and that silicon monoxide was the correct model. With nominal refractive indices for SiO and Al, we completely failed to reproduce the mirror performance, both modeled and measured. However, with SiO₂ as the dielectric, and using TFCalc default values we get an exact match to the model provided by the vendor at visible wavelengths. At infrared wavelengths, we model significantly different reflectivity. As is quite common, the measured performance is significantly different from the model, especially in polarization properties.

Figure 50 shows our Berreman calculations alongside the vendor-provided data at a 45-degree incidence angle. In the

left-hand graphic, we see the reflectivity for *S* as red, *P* as blue, and the average polarization as black. Solid lines represent the vendor-provided model and dashed lines show our Berreman model with 175 nm of SiO₂-protecting Al. In the right graphic of Fig. 50, we see the vendor-provided diattenuation in black and our Berreman models in blue. For wavelengths from 380 to 850 nm, the models match almost exactly, including the linear interpolation between coarsely sampled points. However, for wavelengths longer than 850 nm, the model predictions diverge from our Berreman computations. In the diattenuation plot in the right graphic of Fig. 50, the dashed blue lines show a change in coating thickness of 5 nm. We see that the fit is quite accurate at short wavelengths and that these changes in coating thickness do not significantly improve the long wavelength fit while obviously degrading the short wavelength match between models.

Astronomical systems need accurate knowledge of coating performance at all wavelengths of interest for a range of incidence angles. We show examples of a variety of coatings used in DKIST and other solar telescopes in the following subsections.

10.1 DKIST VTF- and GREGOR-Enhanced Protected Silver Commercial Mirrors

The Kiepenheuer Institute for Solar Physics (KIS) provided us GREGOR telescope witness samples for test in summer 2017.

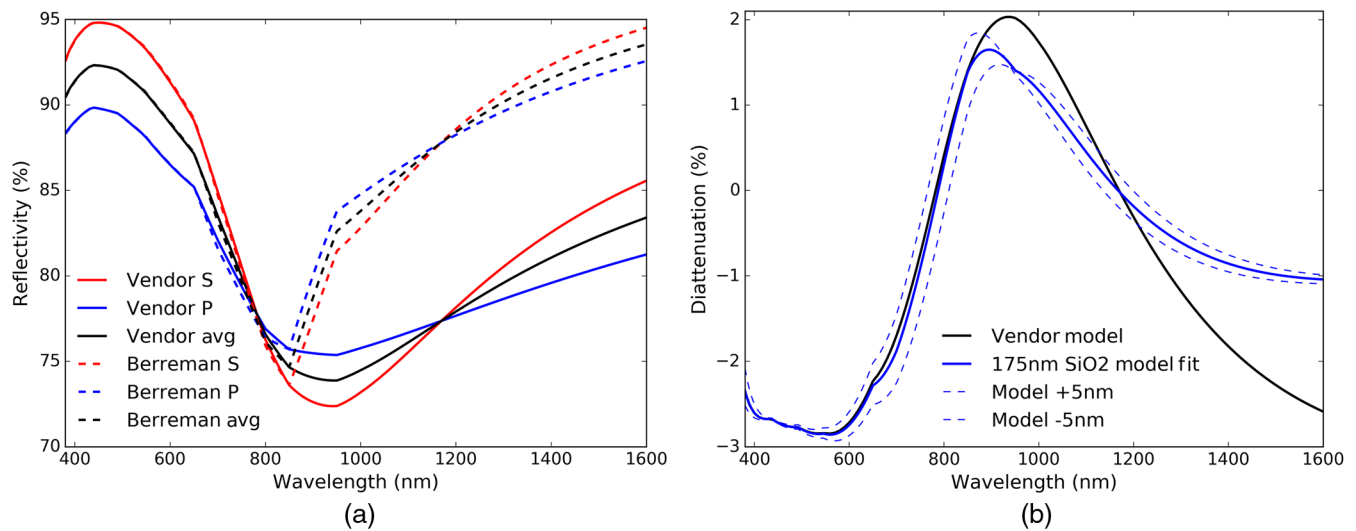


Fig. 50 Commercial mirror models and corresponding Berreman fits. (a) Shows reflectivity fits to protected aluminum mirror and our Berreman model fits using common material formulas. (b) Shows diattenuation. For this mirror, the coating description was a quarter wave of silicon monoxide-protecting aluminum. We find 170 nm of SiO₂ with the CVI formula protecting aluminum using the default TFCalc refractive index values provides an exact numerical match at short wavelengths, including interpolation points.

These witness samples were also the same enhanced protected silver coating formula nominally proposed for the VTF instrument that KIS was constructing for installation on DKIST. The KIS staff was informed that the coating could be modeled as a high-index dielectric layer over a low-index dielectric layer on top of a silver metal layer similar to the models presented here and in our prior work.^{11,67}

Four repeated data sets are collected at 45-deg incidence angle. Figure 51 shows the retardance and diattenuation properties of the Mueller matrix derived from measurements. The IQ/II diattenuation Mueller matrix element is shown in the right-hand graphic. The inverse tangent of the VV and UV elements is used as a proxy for the linear retardance component.

Agreement between visible and NIR spectrographs is quite good as seen by the overlap in the 950- to 1050-nm wavelength range. The extreme edges of each data set are removed for this analysis by stitching together the data sets at 1020-nm wavelength. We ignore longer wavelengths measured by the visible spectrograph and we ignore shorter wavelength data measured by the NIR spectrograph.

We have attempted to fit Berreman models of many material choices in two-layer configurations to the retardance measurements. The three best fits are selected for Fig. 51. All three models represent relatively high refractive index materials on top of a relatively moderate refractive index material. The retardance behavior is similar to the DKIST-enhanced protected silver in

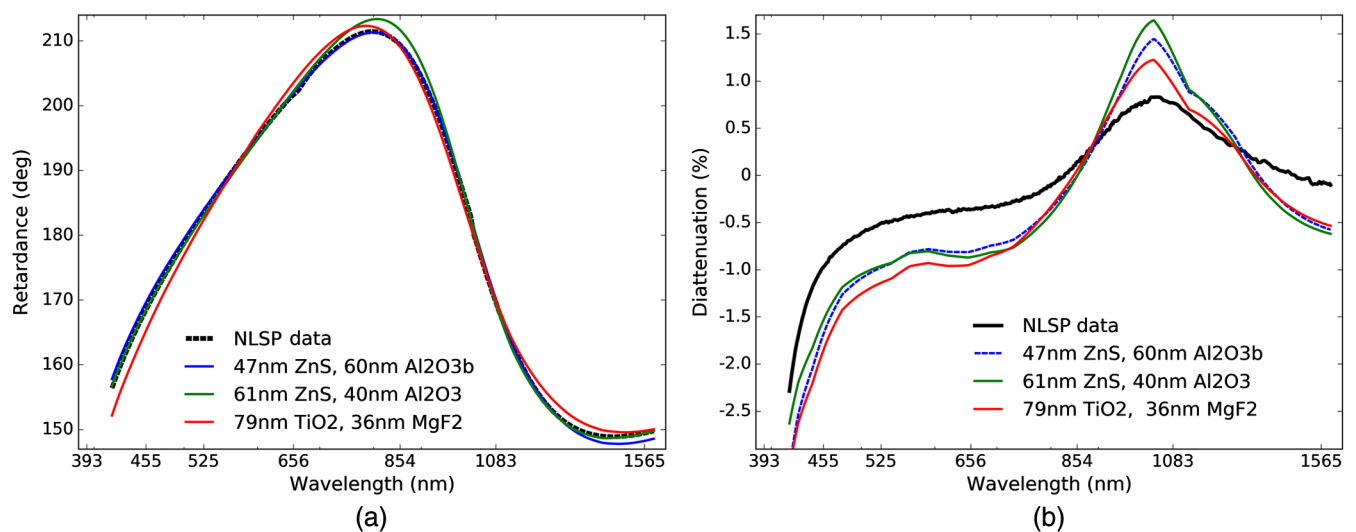


Fig. 51 NLSP measurements and corresponding Berreman model fits. (a) Shows retardance fits to an enhanced protected silver mirror used at the GREGOR solar telescope along with some model fits using common materials. (b) Shows diattenuation along with predictions for the retardance-fit Berreman models. Three different material combinations are shown that are more successful at fitting retardance than several other material combinations.

that there are two wavelengths around blue and NIR where the retardance is zero. If only the visible-wavelength data set is used, the best-fit model layer thickness changes slightly. As an example, the best-fit layer thicknesses are (62 and 60 nm) when using only VIS spectrograph data as opposed to (65 and 56nm) when using the full VIS+NIR range for a HfO_2 over Al_2O_3 formula model.

10.2 Commercial Mirror Samples: Big Bear Solar Observatory and Newport PAG

We also aim to help create a telescope model comparison for the BBSO. Many observatories use commercial off-the-shelf (COTS) optics. It is straightforward to create polarization performance models. We were given witness samples from the BBSO aluminum-coated mirrors as well as a COTS-protected metal-coated mirror from Newport used at BBSO. This Newport coating has been used on several mirrors as part of the BBSO optical train. The BBSO uses several other commercial mirrors in their optical train and knowledge of each coating is required to create a detailed polarization model.

We measure the Mueller matrix of the Newport mirror at 45-degree incidence angle with NLSP. The linear retardance in the UV plane as well as the IQ diattenuation is derived using the Mueller matrix. The resulting stitched data sets and Berreman models are shown in Fig. 52. There are two models that fit the Newport coating equally well. The first fit is 137-nm thickness of the SiO_2 model coated over 14-nm thickness of the Al_2O_3 model using the Boidin et al.⁶⁸ refractive index formula using index 1.67 at 850-nm wavelength. A similarly good model fit is seen for 77-nm thickness of the SiO_2 model coated over 71-nm thickness of the Al_2O_3 model with refractive index of 1.55 at 850-nm wavelength. Both SiO_2 models have refractive index of 1.55 at 850-nm wavelength. The 0.5-degree retardance step barely visible at 1020 nm is the stitching wavelength where VIS spectrograph data are concatenated with NIR spectrograph data.

For each vendor the BBSO used, we requested information on the coating prescription. As expected, only limited and incomplete information could be obtained, if any was even available. This is clearly insufficient for creating polarization models of reasonable fidelity at observatories with powered optics at varying incidence angles.

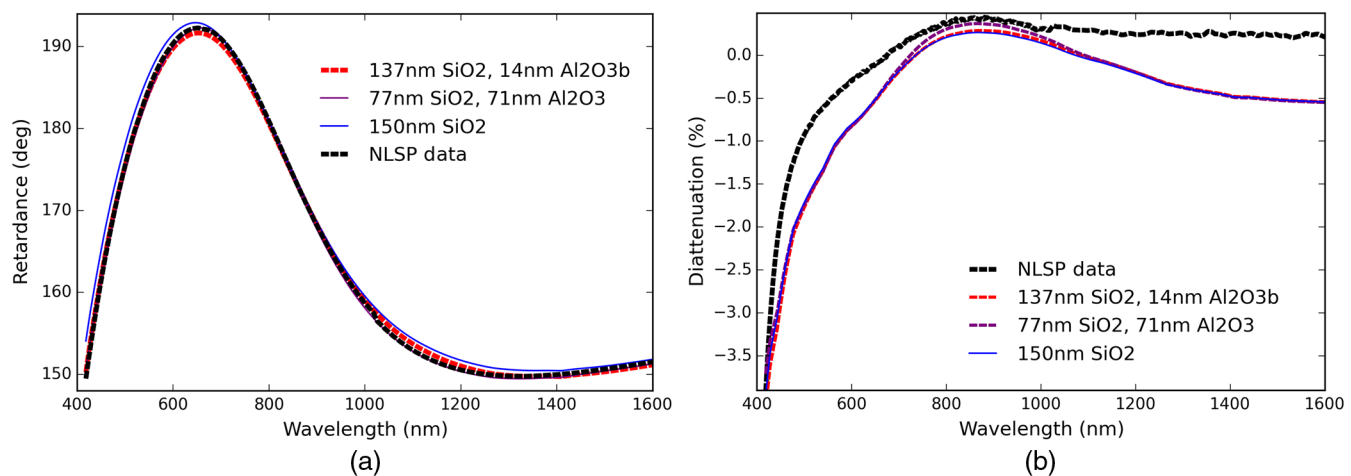


Fig. 52 Commercial Newport-enhanced protected silver. (a) Shows retardance fits and some model fits using common materials. (b) Shows measured diattenuation along with the Berreman models for diattenuation (not fit).

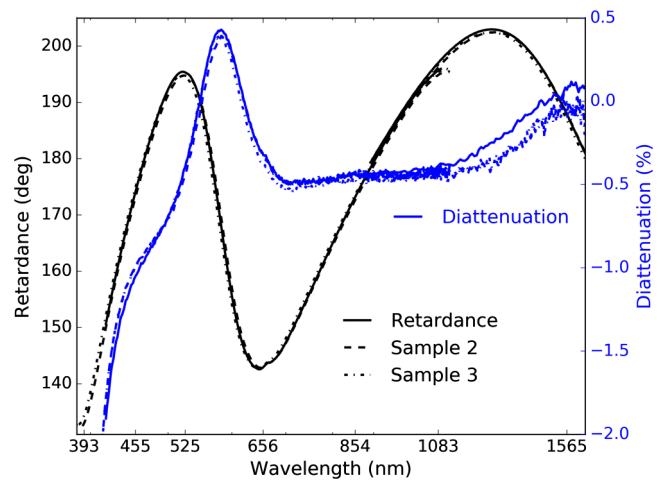


Fig. 53 NLSP measurements of three Thorlabs-protected silver mirrors. Black shows retardance using the left-hand Y axis. Blue shows diattenuation on the right-hand Y axis. The first sample is measured 7 months before the second two, and the diattenuation is shifted by 0.25% for the curves to match.

10.3 Commercial Mirror Samples: DKIST and A Thorlabs-Protected Silver K-Cell

We tested three Thorlabs-protected silver mirrors we use in our DKIST laboratory. These Thorlabs mirrors have a different wavelength dependence of retardance and diattenuation than several of the previous samples reported in the main paper. This difference is likely caused by substantially thicker coating layers as suggested below by our fitting process outlined above. In Fig. 53, we show the retardance in black and diattenuation in blue using the right-hand Y axis measured with NLSP in the reflective configuration for each of the three samples. The retardance curves cross 180 deg at four wavelengths over the DKIST instrument wavelength range. The diattenuation for this sample has a somewhat strong peak near 600 nm. One mirror was measured in July 2017, while the other two mirrors was measured in February 2018.

The three mirror samples were all procured at the same time. While it is possible that they were all coated in the same shot,

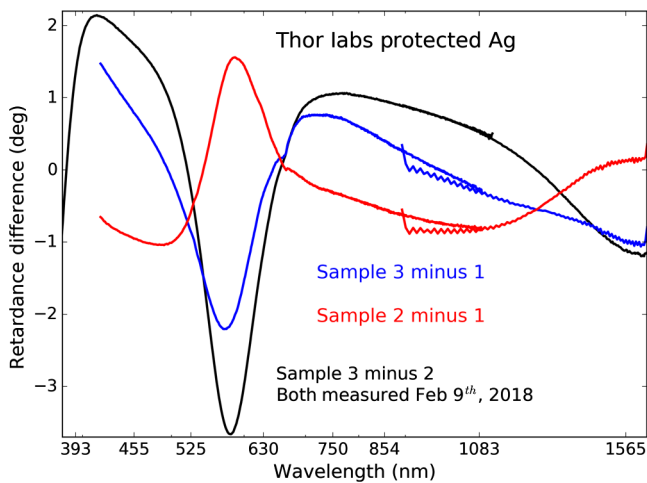


Fig. 54 The difference in retardance between Thorlabs-protected silver mirrors. Sample numbers 2 and 3 measured with NLSP on the same day. Sample 1 had been measured in July 2017. Differences are more than an order of magnitude larger than systematic errors.

there is no guarantee of their coating heritage. We measure significant differences in both the diattenuation and the retardance. The diattenuation measured in the first mirror is spatially offset by 0.25% in Fig. 53 to match values at NIR wavelengths. As we have shown above for the DKSIT silver mirrors in Fig. 46, there are significant impacts to diattenuation for even small variations in the layer thicknesses of the dielectrics in the model. Our 0.25% offset is a likely a combination of real systematic difference between measurements as outlined for NLSP in prior sections and also real variations between these commercial mirrors.

The retardance curves for all three samples match to within 3 deg, but there are easily detectable difference between nominally identical samples. We show in Fig. 54 the difference between mirror retardance for Thorlabs mirrors number 3 and 2 in black. Both mirrors were measured on the same day with NLSP at 45-deg incidence angle. We also show the difference

between sample 3 and sample 1 in blue as well as sample 2 and sample 1 in red.

We note that repeatability tests shown above in Figs. 43 and 44 showed that after remounting and aligning a mirror, we can reproduce a measurement to better than 0.05 deg. Estimates of retardance computed by using different combinations of the UV Mueller matrix elements agree to better than 0.3 deg. Both of these systematic errors are an order of magnitude smaller than the difference measured here between Thorlabs mirrors.

With these data sets, we can attempt to fit various coating models to the retardance measurements. Figure 55 shows the retardance and diattenuation measurements as the dashed black lines. The prediction from the best fit to retardance from our two-layer Berreman coating models are shown as solid lines of varying color. Retardance is shown on the left with the diattenuation on the right. The dielectric layer thicknesses found in the fit are shown in the legend of the retardance graph.

We have attempted to fit a large range of two-layer coating models but found that only a few reasonably reproduced the retardance curves. These better-fitting models generally use relatively high refractive index material curves such as ZnS, TiO₂ from TFCalc or vendor references, and Al₂O₃ from either Zemax or Boidin et al.⁶⁸ references. The red curve shows a coating model with a single layer of TiO₂ at 185 nm physical thickness using the Boidin et al.⁶⁸ refractive index curves from refractiveindex.info. The blue curve shows another model with layer of amorphous SiO₂ at 199 nm physical thickness coated on top of 104 nm of Al₂O₃. In all models fit, the layers end up with thicknesses of significantly >150 nm. The two-layer coating models described in the main text had total thickness around or <100 nm. All models diverge at longer wavelength where it is possible that both the metal and the refractive index curves for the dielectrics have higher error.

The right-hand graphic of Fig. 55 shows the diattenuation. All models consistently underestimate the diattenuation for blue and NIR wavelengths. The spectral feature around 600 nm shows a diversity of results between the models. We do not expect diattenuation to be modeled well as this parameter is

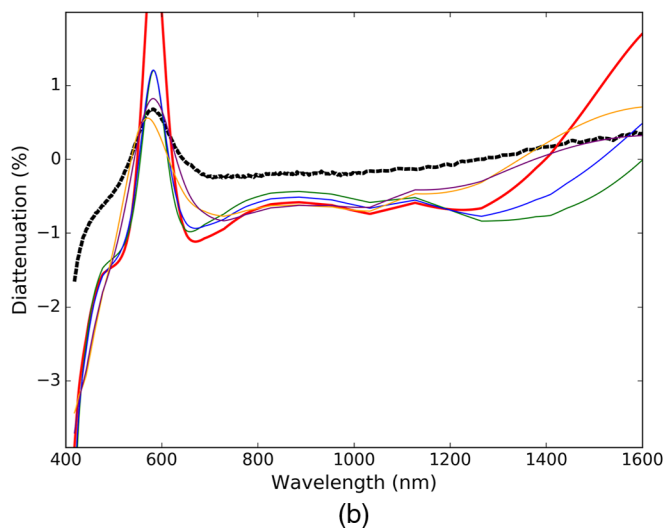
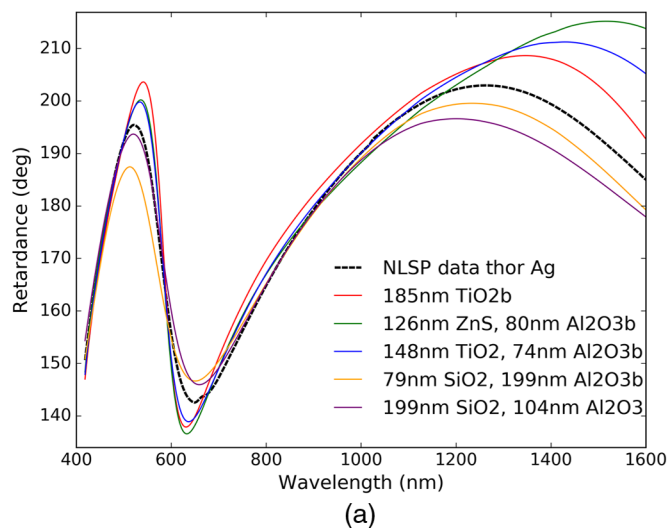


Fig. 55 Commercial Thorlabs-protected silver mirror and corresponding fits. (a) Shows retardance fits and some model fits using common materials. (b) Shows measured diattenuation along with the Berreman models for diattenuation (not fit). For this mirror the dielectric layers are much thicker and the fits to retardance data are significantly worse.

Table 16 K-cells.

Name	$\theta_{1,3}$	θ_2
Narrow	50.4	10.8
Middle	53.4	17.4
Wide	57.6	25.3

not included in the fit. We showed above in Sec. 3.1 that the metal complex refractive index can strongly influence the fit and can be highly variable between coating process and vendors.

We combined the three Thorlabs mirrors to create a sample where the beam enters and exits in translation and tilt exactly following the unperturbed incoming beam. This setup is often called an image rotator, derotator, K-mirror, or K-cell. Common designs use relatively high incidence angles near 60 deg for the outer two mirrors and a smaller angle for the inner mirror. In our setup, we are able to place these round 1-in. diameter mirrors into kinematic mounts with incidence angles near 50 deg to 60 deg for the outer mirrors and 10 deg to 17 deg for the inner mirror. Table 16 shows the incidence angles estimated for the two outer mirrors (θ_1 and θ_3) as well as the lower incidence angle inner mirror.

Using a HeNe laser with a ~ 3 -mm beam, we aligned the optical footprint location on each mirror as well as the individual mirror tilts. We ensured that the exit beam roughly matched the unperturbed beam in height and spot location over a ~ 1 -m path with and without the K-cell translated into the beam. As a further alignment step, our NLSP software provides tools to show the symmetry of detected flux upon 180-deg rotation of the NLSP retarders as the various optics are rotated in 10-deg steps through 360 deg. This diagnostic shows photometric errors over 0.5% if the beam is not well centered on the spectrograph fibers. We perform additional tilt adjustment of each mirror after aligning for translation and height in the

NLSP beam to maximize the flux through the system (minimize vignetting on the fiber) as well as to ensure the ~ 4 mm NLSP beam is centered on the optics.

In Fig. 56, we show the NLSP-measured retardance and diattenuation as solid colored lines. The narrower K-cell is shown as blue. The moderate K-cell configuration is shown in green. A wider K-cell is shown in red. Dashed lines show a two-layer Berreman coating model for the three mirrors operating in series at the appropriate incidence angles. We only show one of our better fit two-layer models as 200 nm of SiO₂ over 100 nm of Al₂O₃ coated over silver modeled using the default TFCalc values. There is a sharp change in the predictions for wavelengths short of 400 nm. This is caused by a strong change in the silver refractive index complex component in the default TFCalc values interpolated here. The value of k changes from 1.93 at 400 nm to 5.85 at 375-nm wavelength. We use linear interpolation, which accounts for the sharp change in behavior at 400 nm.

This issue with TFCalc default metal refractive index and all other metal refractive index values is drastically seen by the failure of the Berreman models to match the measured reflectivity through the K-cell. We show the three K-cell reflectivity measurement of the wider configuration as solid red in Fig. 57. The Berreman model using the default TFCalc values is shown in Fig. 57 as a red dashed line. There is reasonably good agreement in spectral shape and throughput for wavelengths longer than 420 nm. At short wavelengths, however, the high complex index of $k = 5.85$ in the TFCalc silver creates reflectivity values over 50% higher than observed. We additionally show two different sets of vendor values as black and blue. These values, respectively, overestimate and underestimate the throughput of this three-mirror system at longer wavelengths. Both silver refractive index values overestimate reflectivity at the shortest wavelengths.

These models are not expected to match in detail as this COTS mirror has an unknown coating in an unknown process. Additional work is required to adjust the refractive index of the dielectric and the metal to match this particular optic. The two

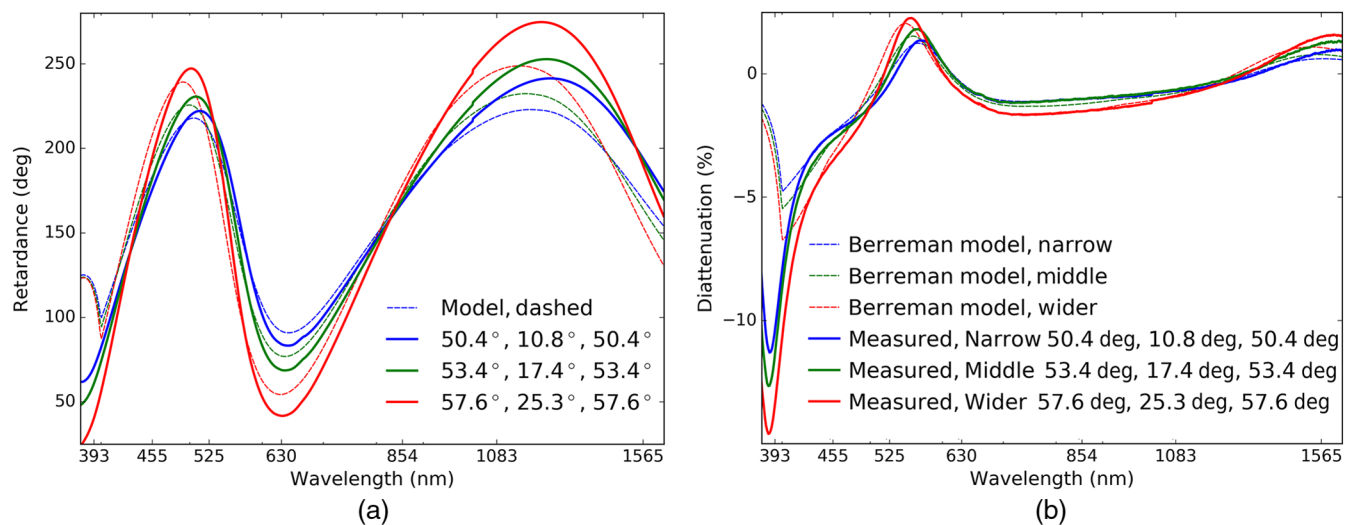


Fig. 56 Transmission measurements from a three-mirror K-cell using our three commercial Thorlabs-protected silver mirrors. (a) Shows retardance measurements and a Berreman prediction using our best-fit two-layer coating model. (b) Shows measured diattenuation along with the Berreman models for diattenuation (not fit). Note that the sharp change in behavior for wavelengths short of 400 nm is caused by a strong change in the silver refractive index complex component in the default TFCalc values used here.

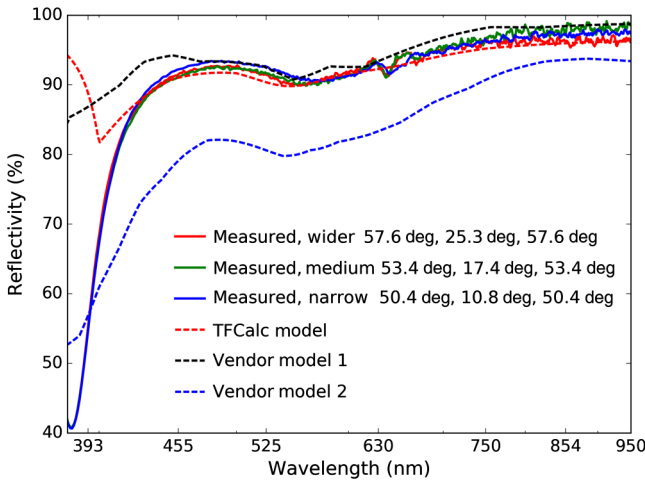


Fig. 57 The combined three-mirror reflectivity of the wider K-cell with Thorlabs silver mirrors. Dashed lines show two-layer coating models with 200 nm of SiO₂ over 100 nm of Al₂O₃ protecting silver. The complex refractive index of the silver varies between models, giving rise to strong changes in predicted reflectivity.

outer mirrors are at relatively high incidence with the inner mirror at small incidence angles. With all folds roughly in the same plane, we expect the retardance to be somewhat larger than double the magnitude about 180 deg than that of a single mirror at 45 deg. This is easily seen by a comparison between the single mirror of Fig. 55 and the three mirrors in Fig. 56.

One major benefit of testing K-mirror-type setups is that a much larger range of incidence angles can be tested. The polarization predictions need to be valid from near normal incidence to 45 deg to account for the full range of DKIST reflections. By building this type of setup, we can further constrain our simple coating models to ensure that accurate predictions are derived from these coatings as we have applied to telescopes such as DKIST and AEOS.^{11,67}

10.4 Image Rotator K-Cell: A NLSP Sample with Both ViSP and Thor Silver Mirrors

The K-cell-type sample can be useful in deriving reflectivity of individual mirrors using the well-calibrated transmission arm of NLSP. Given the various measurement techniques applied to the ViSP many-layered silver mirrors, we confirm the reduced transmission bands as well as the non-negligible polarization impacts at low incidence angles. We had taken the Thorlabs K-cell in the narrow configuration and had replaced the low-incidence middle mirror with the ViSP witness samples. This allows extraction of the polarization and reflectance properties at an incidence angle around 11 deg, similar to the ViSP F2 mirror at 12.3-deg incidence.

We show in the left-hand graphic of Fig. 58 the retardance and diattenuation of the combined three mirrors in the narrow configuration. The smooth, large magnitude structures of Fig. 56 are reproduced by the two high-incidence Thorlabs silver mirrors at 50.4-deg incidence. However, we now see significant narrow spectral features in both retardance and diattenuation around 450- to 500-nm wavelength. Additional small amplitude ripples are also seen in the retardance curve caused by the many-layered enhanced silver coating design. We attribute these narrow spikes and broader ripples to the ViSP many-layered mirrors.

In the right-hand graphic of Fig. 58, we extract the reflectivity of the ViSP samples by dividing the reflectivity of the two Thorlabs mirrors derived in the last section. We use the cube-root of the Thorlabs K-cell of Fig. 57 as an approximation of an individual Thorlabs mirror. The various incidence angles tested did not show an appreciable difference in reflectivity. Dividing the measured K-cell reflectivity by this Thorlabs reflectivity curve twice results in a reflectivity curve for the ViSP witness sample that very well correlates with the vendor data presented in the main paper. The black and blue reflectivity curves show two separate witness samples that each had different storage histories over roughly 9 months between coating and measurement. Though their storage conditions varied, the reflectivity

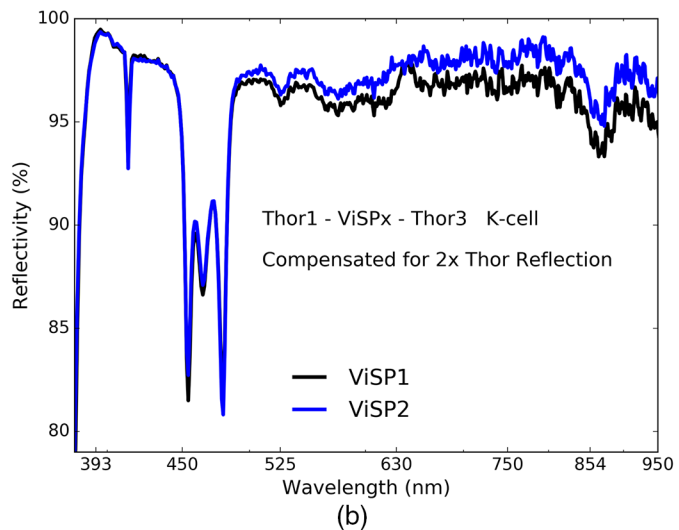
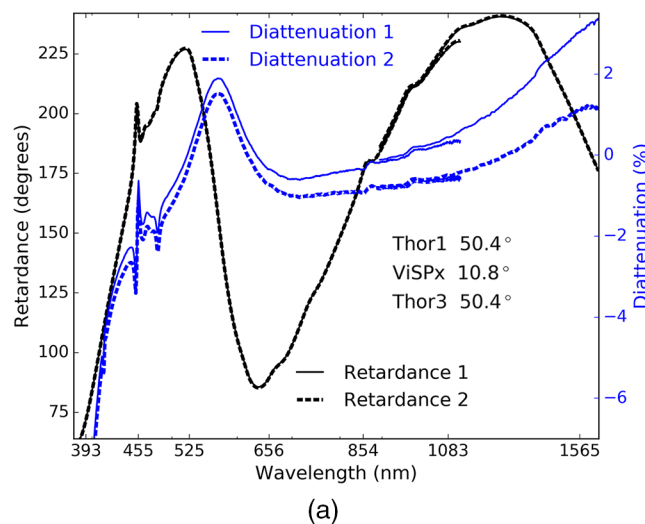


Fig. 58 (a) Shows retardance and diattenuation for a K-cell made of two Thorlabs-protected silver mirrors at high incidence angles and a ViSP witness sample at low incidence angles. (b) Shows the reflectivity of the ViSP sample after compensating for the two Thorlabs mirror reflections. The ViSP sample adds narrow spectral features seen around 450-nm wavelength and substantial drops in reflectivity in two separate bandpasses.

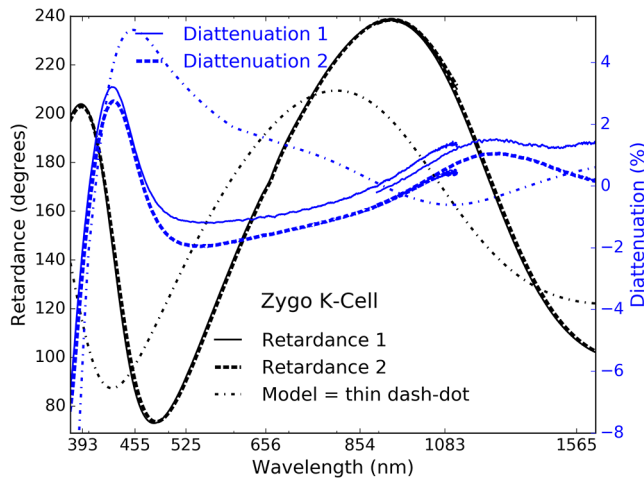


Fig. 59 An enhanced protected silver from Zygo in a *K*-cell configuration. Black shows retardance, while blue shows diattenuation using the right-hand *Y* axis. A model is a thin dash-dotted line.

and polarization properties between the two samples are remarkably consistent. In testing at the vendor site immediately after coating, the low reflectivity band between 450 and 500 nm is not present.

10.5 Protected Silver Mirrors: DKIST Feed Optics with Zygo Silver

DKIST has used an enhanced protected silver from Zygo for the feed mirror M9a as well as one instrument feed mirror (DL-FM1) inside the DL-NIRSP instrument relay optics. Figure 59 shows the retardance and diattenuation measured in a *K*-cell with witness samples from Zygo. Samples are roughly 8 years old and are stored in laboratory conditions. These coatings use an ion-assisted deposition process and are described as having a few layers over silver. The samples are stored in a laboratory environment that is roughly 50% humid in the summer and a bit drier in the winter. The *K*-cell sample is measured at the same 50 deg to 11 deg to 50 deg configuration.

The two different curves of Fig. 59 show the difference when we replaced the first fold at 50-deg incidence with a separate sample from a separate coating shot. There is only a small difference in retardance with a fraction of a percent change in diattenuation.

In the fall of 2018, the M9a and DL-FM1 optics had been coated. Figure 60 shows the reflectivity and diattenuation. The test run is shown in red. The M9a coating run is shown in green. The DL-FM1 coating run is shown in blue. These coatings are not blue-enhanced as they feed infrared optimized instruments working at wavelengths longer than 450 nm. The diattenuation is less than half percent for wavelengths longer than 500 nm. There is a fairly prominent absorption feature around 3- μ m wavelength and a corresponding change in diattenuation. Both curves show discontinuities around 1000 nm wavelength from the change in spectrophotometric equipment, also illustrating the level of systematic error present in the data. The reflectivity curves show that there are differences of roughly 1% between coating runs.

10.6 Protected Silver Mirrors: DKIST VBI and BBSO with Edmund Optics

We show additional examples of polarization properties derived from NLSP Mueller matrix measurements for commercial protected silver mirrors relevant to DKIST and BBSO. The VBI instrument in DKIST uses an Edmund Optics off-the-shelf protected silver mirror. We took the actual 6-inch diameter mirror from the VBI optical path and measured the Mueller matrix at 45-deg incidence in the center of the optic. The BBSO optical path also contains a few mirrors that are a commercial Edmund Optics protected silver coating with polarization properties possibly similar to this mirror. Figure 61 shows the retardance and diattenuation derived from the measurements. Diattenuation is rapidly increasing in magnitude for wavelengths shorter than 420 nm. For visible and NIR wavelengths, the diattenuation stays below 1% magnitude with a few sign changes. The retardance is broadly similar to the two-layer simple models we have presented in this paper with retardance crossing the theoretical 180-deg magnitude at wavelengths around 525 and 1100 nm.

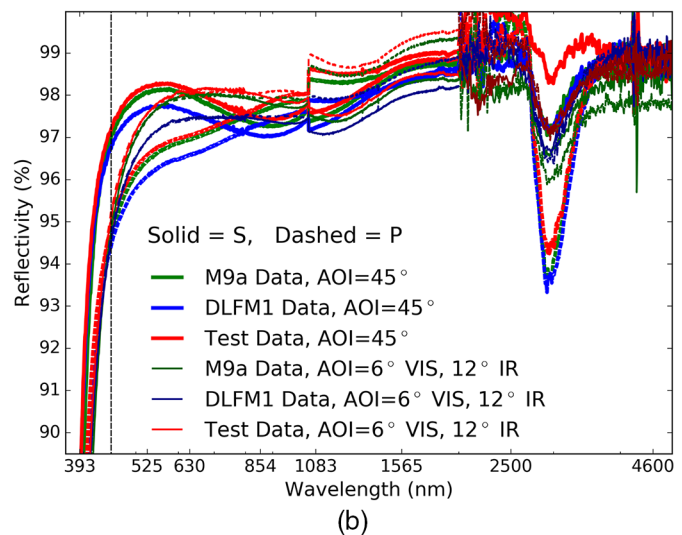
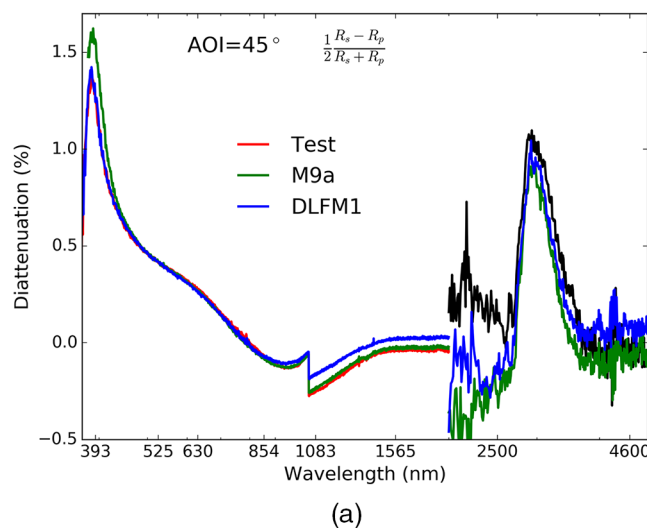


Fig. 60 Diattenuation of *S*- and *P*-polarization states measured by Zygo at 8 deg and 45 deg incidence in (a). Reflectivity of *S*- and *P*-polarization states measured by Zygo at 8 deg and 45 deg incidence in (b). Colors show different coating runs.

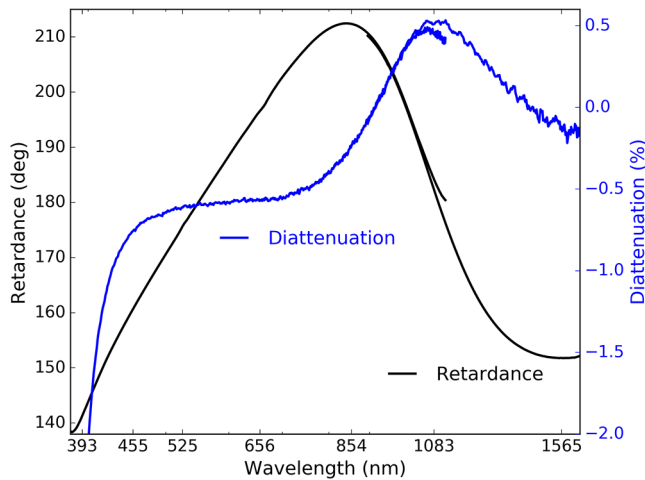


Fig. 61 An Edmund Optics-protected silver used in VBI-blue (and possibly similar to BBSO mirrors). Black shows retardance and blue shows diattenuation on the right-hand Y axis.

10.7 Protected Silver Mirrors: DKIST DL-NIRSP and EMF

The DL-NIRSP instrument contracted a vendor who ultimately procured some coatings that were not the specified DKIST silver. Once we discovered this alternate coating was present on several mirrors in the DL-NIRSP optics, we directly measured one of the flat DL-NIRSP mirrors that had used this alternate coating. Figure 62 shows measurement of a coating on a DL-NIRSP spectrograph mirror. Diattenuation values for the DL-NIRSP mirror are slightly higher, but still below 2% magnitude. This coating shows much stronger oscillations of diattenuation at short wavelengths. However, the DL-NIRSP only observes wavelengths >525 nm and this coating has <1% diattenuation for wavelengths >700 nm. The retardance also crosses the theoretical 180-deg magnitude at effectively three wavelengths: 380, 700, and 1080 nm. The reflectivity, retardance, and diattenuation are acceptable for DKIST purposes, especially since only one DL-NIRSP feed mirror uses this coating and only at 3.8-deg incidence angle.

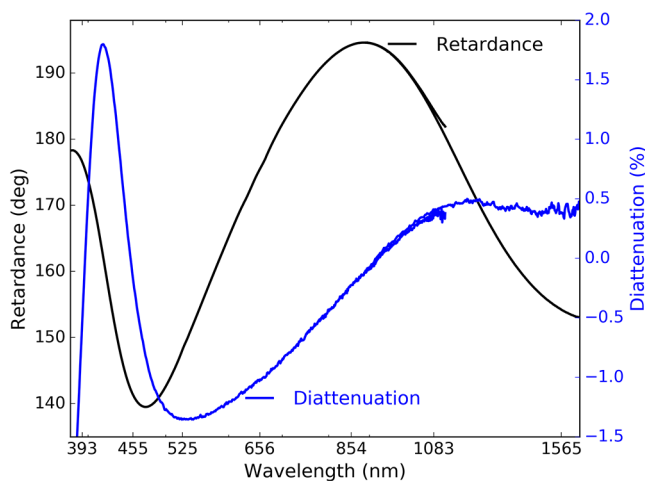


Fig. 62 A coating by EMF used on two of the DL-NIRSP spectrograph mirrors as well as the spherical steering mirror feed optic. Black shows retardance and blue shows diattenuation on the right-hand Y axis.

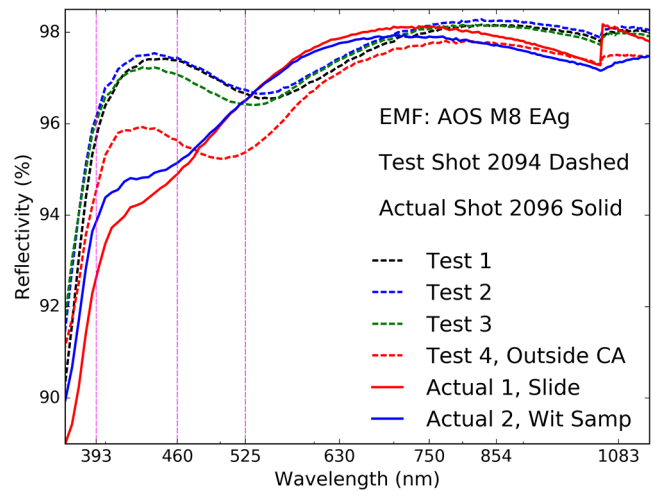


Fig. 63 The blue enhanced AG99 coating by EMF used on DKIST M8. Test run data are shown as dashed lines. Solid lines show witness samples adjacent to the M8 optic during the coating run.

10.8 Protected Silver Mirrors: DKIST M8 and EMF Blue-Optimized AG99

DKIST also utilized EMF for one of the coude feed mirrors: M8. We used a blue-modified flavor of the AG99 formula to ensure that we did not compromise the 393-nm wavelength throughput. Metrology was recorded at 8-deg incidence while the M8 off-axis parabola was mounted at roughly 5-deg incidence for the chief ray.

Figure 63 shows the spectrophotometry from EMF at 8-deg incidence for two coating shots. The test coating shot number 2094 is shown as dashed lines while the coating shot deposited on the actual DKIST M8 is shown in solid lines. As is typical, the test data show spectral reflectivity variation of up to 3% at some wavelengths. The test shot run 2094 had three samples distributed within the clear aperture shown as black, blue, and green dashed lines. There is a fourth sample located outside the clear aperture of the M8 optic that shows somewhat similar spectral behavior but with significant deviation at short wavelengths. The two solid lines of the actual coating shot show tests on a glass slide and also a standard witness sample coupon. As the M8 optic is coated, these samples are by definition outside the clear aperture of the optic and are only representative of the actual M8 coating within the limits of the coating spatial uniformity as deposited in this chamber. The test run data show a similar drop in blue reflectivity though with some differences in the spectral oscillations.

10.9 Protected Silver Mirrors: DKIST C-M1 and M9, ViSP Mirrors F1, F2, and FM1

We had several mirrors coated with an Infinite Optics-enhanced protected silver with formulas EAg1-420 and -450. We list in Table 17 the coating run number associated with each of the optics. The FIDO mirror C-M1 was in the same shot as the first ViSP feed mirror (FM1). The second two ViSP mirrors were in a second shot. A separate coating shot was done for DKIST M9.

We obtained three witness samples from each coating shot containing DKIST optics. With these, we were able to create a K-cell image rotator-type setup to use as a sample

Table 17 IOI EAg runs.

Run	Name	AOI
6-7759	Samples	—
6-7766	FIDO C-M1	15 deg
6-7766	ViSP F1	2.2 deg
6-7767	ViSP FM1	28 deg
6-7767	ViSP F2	12.3 deg
9-3095	DKIST M9	10 deg

in the transmissive arm of NLSP. Figure 64 shows the retardance on the left and diattenuation on the right for this sample.

We used the narrow *K*-cell setup with approximate incidence angles of 49 deg on the outer two samples and 8.6 deg on the inner sample. We only had two samples for the chamber six test shot 7759 so we substituted a DKIST sample from M10 spatial position U. At the low incidence angle of 8.6 deg, we expected retardance impact of less than a few degrees when modeling this system. The four curves represented the same materials but with different thicknesses of each material. All of these coatings were slightly thinner than the DKIST-specified coating with zero retardance values at correspondingly shorter wavelengths.

Figure 65 shows the reflectivity measured at IOI from 300 to 2200 nm. We follow the same color scheme as Fig. 64. One sample has been measured to 5000-nm wavelength with reflectivity slowly increasing above 99% as predicted in the coating model. All coatings have >96% reflectivity at the 393-nm Ca K line.

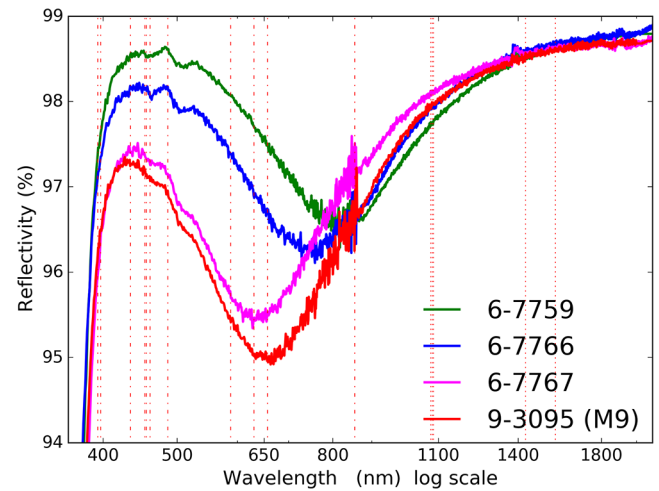
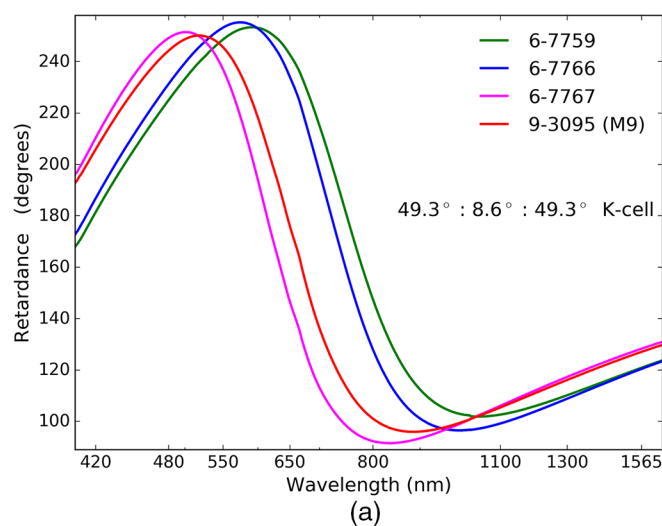


Fig. 65 The reflectivity of each coating by Infinite Optics measured at 8-deg incidence. Vertical dashed lines show spectral lines of interest.

10.10 Protected Silver Mirrors: ViSP Fold Mirrors FM2, FM3, FM4, and RMI EAg

The ViSP feed optics include a fold mirror (FM2) coated with a Rocky Mountain Instruments-enhanced protected silver. The optic is mounted in the *F*/32 diverging beam after the slit reflecting at an incidence angle of 47.7 deg toward the modulator. This optic sees footprints of only a few millimeters and is included in the system modulation matrix as it is ahead of the modulator. In Fig. 66, we show the reflectivity left and diattenuation right for 45-deg incidence. The reflectivity is mostly over 96% with an exception around 420-nm wavelength. The vertical dashed lines show spectral channels of interest. The diattenuation oscillates spectrally with six zero crossings in the nominal ViSP bandpass. The diattenuation is never >1% though the sign and magnitude changes along with the spectral oscillations.

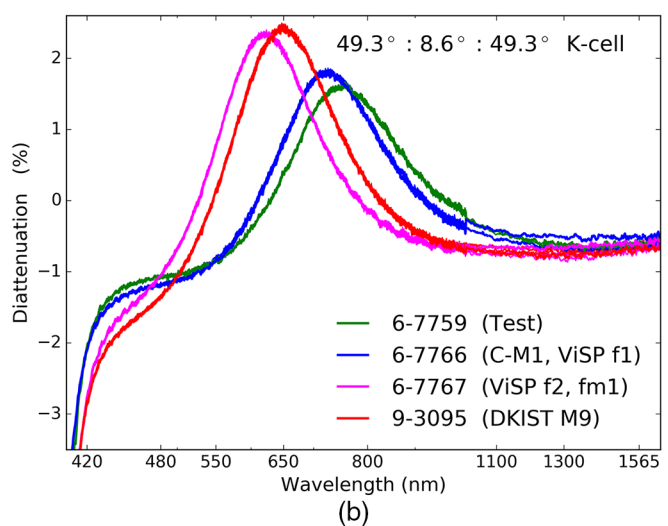


Fig. 64 (a) Shows retardance and (b) shows diattenuation. The chamber 6 test shot 7759 is shown in green, shot 7766 in blue, shot 7767 in magenta, and the chamber 9 shot for DKIST M9 in red. There are actually 12 red curves and 9 curves of all other colors as we repeated each optical alignment three or four times, and repeated each test at each alignment three times. Some enhanced statistical noise is seen in the diattenuation graph in (b).

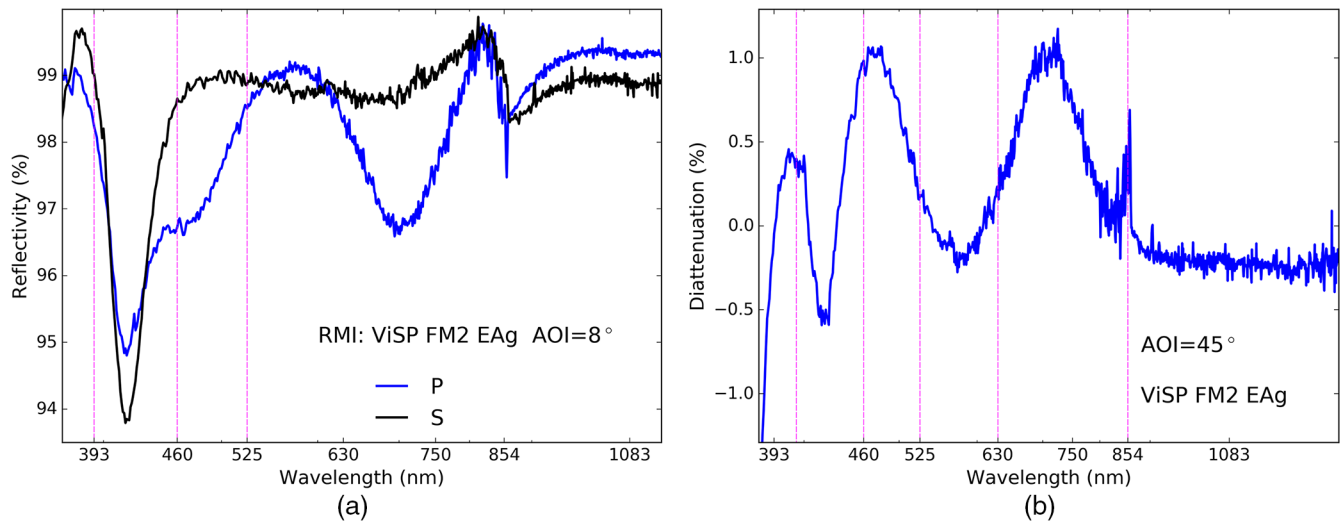


Fig. 66 Spectrophotometry for S (black) and P (blue) polarization states at 45-deg incidence shown in (a). Diattenuation derived from S&P reflectivity is shown in (b). Vertical dashed lines show typical solar-observing wavelengths.

10.11 Bare Aluminum Mirrors: DKIST Primary and Test Mirrors Coated at AFRL

The DKIST primary mirror (M1) is coated at the AFRL coating chamber located adjacent to DKIST on the summit of Haleakala, Maui. We also have a full-sized commissioning mirror as a replica of M1. Both are coated by AFRL with bare aluminum. Reflectivity of multiple samples in each coating run measured by a Varian Cary 5000 at Gemini in Hilo is shown in Fig. 67.

We tested two witness samples from the first coating on the science mirror. Figure 68 shows the retardance on the left and the diattenuation on the right. We ran our two-layer fitting routines using the Berreman calculus in our Python scripts. However, for this run we let the thickness of the aluminum metal layer be the second thickness variable on a grid from 40- to 200-nm thickness in steps of 10 nm. The top layer was the aluminum oxide using the Boidin refractive index curves

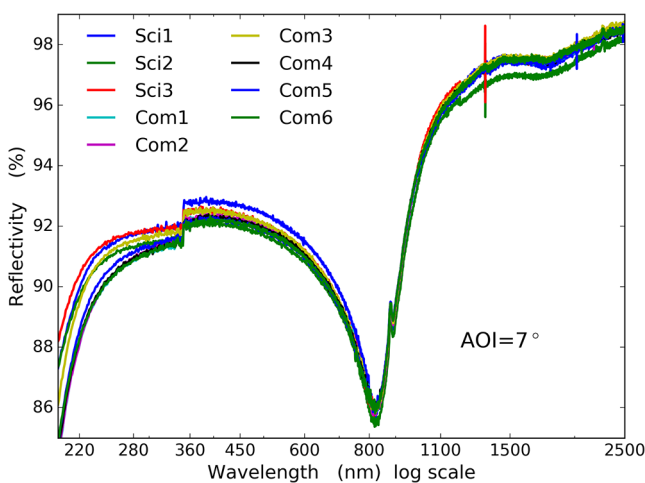


Fig. 67 The reflectivity measured at 7-deg incidence angle for three samples coated with the actual M1 science grade mirror and another six samples measured during coating of the full-sized M1 commissioning mirror.

running from 0 to 10 nm in steps of 0.5 nm. We found a coating model of 2.5 nm Al_2O_3 over 50 nm aluminum as the best fit when using the TFCalc aluminum metal refractive indices. We also noted that we have corrected the diattenuation in Fig. 68 for a linear offset to highlight the often crude spectral sampling of typical coating models. We found the same 2.5 nm of oxide but a thinner 40-nm metal layer when using an internal NSO aluminum metal interpolation.

Coatings on large mirrors are expected to be spatially variable. We note that we have interferometric testing of larger samples distributed throughout the chamber during testing showing that the coating is physically between 90- and 150-nm thick across the 4-m aperture so neither of these metal thickness fits are close to a direct thickness measurement. A recent study on polarization aberrations and the impact on the Habex system by Breckenridge et al.⁸¹ shows spatial variation in the retardance in reflection for a 3.75-m diameter mirror coated at the University of Arizona in Fig. 19.⁸¹ This form birefringence measurement at magnitudes of 0.002 radians retardance required a special setup developed, built, and measured by B Daugherty.⁸¹ As we have detailed above, getting correct values for the optical constants of the coated aluminum is critical for matching the data with high spectral accuracy. The Breckenridge et al.⁸¹ work shows that spatial variation is present and measurable across large area mirrors. Given the factor of ~ 2 thickness variation in the DKIST aluminum coating, we certainly anticipate spatial variations in the mirror at some undetermined magnitude due to the varying properties of the aluminum across the mirror.

11 Appendix D: Antireflection Coatings: Spectral Oscillations

We provide more details here on the antireflection coatings WBBAR1 and WBBAR2 described in Sec. 4. We have multiple coating runs over more than a year in several coating chambers at IOI. We show how the general magnitude and incidence angle behavior is very repeatable, but that spectral oscillations are always present impacting estimates of coating behavior at individual spectral channels typical of solar spectropolarimeters.

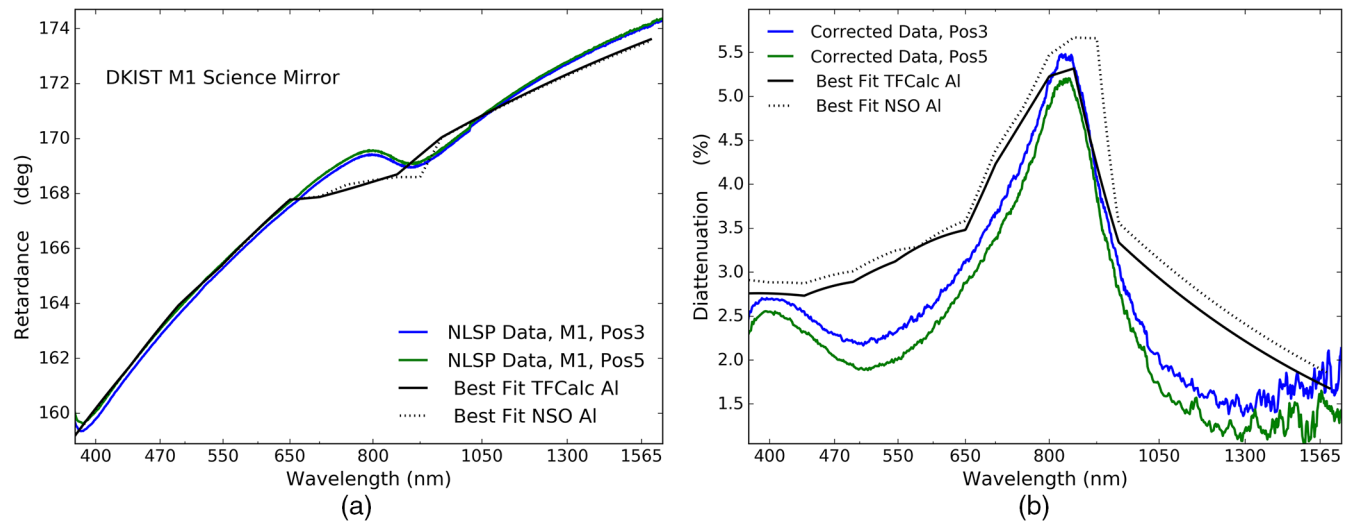


Fig. 68 (a) Shows retardance and (b) shows diattenuation of the DKIST M1 science mirror witness sample from spatial position 3 measured in reflection at 45-deg incidence angle. Blue shows the NLSP data. Green shows spatial position 5. The solid black line shows the Berreman code fit when using the TFCalc refractive indices for aluminum. Dashed black shows the fit with an internal NSO aluminum refractive index interpolation.

We did two test-coating shots of the WBBAR1 formula in chambers 7 and 10 and then coated both sides of an Infrasil window intended for use in one of the DKIST calibration polarizer assemblies in chamber 12. Both Infrasil window runs were coated sequentially in chamber 12 with first side coated in shot 6267 and the second side in shot 6268. We had a 1.1-mm-thick Infrasil 301 sample coated on both sides for photothermal and spectropolarimetric assessments in NLSP.

Figure 69 shows the retardance and diattenuation versus incidence angle for all WBBAR1 samples tested in NLSP. The two solid lines show excellent repeatability for the sequential shots 12-0267 and 12-0268. The dashed line shows that the

preliminary shot 10-0095 has very similar performance but with slightly different spectral oscillations. This is expected for a different shot in a different chamber. Additional comparison with the Infrasil sample that is coated on both sides is shown with the dot-dash lines in both graphics where results have been divided by 2.

The legend shows a few colors to note that the double-side coated sample had the results divided by 2 for each measurement at each incidence angle. The retardance in transmission should scale as $2\times$ but the transmission diattenuation will not. The diattenuation of the uncoated back surfaces adds significantly more polarization than a two-side coated surface.

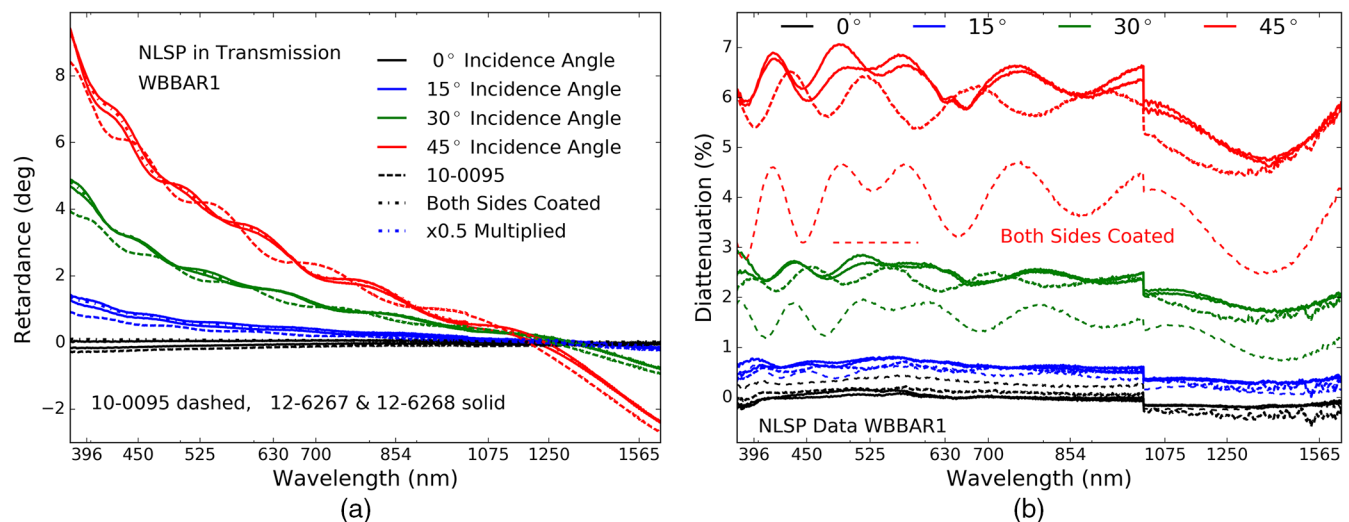


Fig. 69 Transmission retardance (a) and diattenuation (b) from NLSP measurements of Infinite Optics WBBAR1 on all samples with a common design: 10-0095, 12-6267, and 12-6268. The solid lines show measurements of samples 12-6267 and 12-6268. Dashed lines show the test shot 10-0095. The double-side coated sample with both 12-6267 and 12-6268 is shown with long dashes and has been divided by 2. The net retardance scales appropriately as the uncoated sample back surface reflection does not introduce retardance while the coated back surface reflection roughly doubles the sample net retardance. The diattenuation is significantly impacted as the back surface reflection is now also coated and significantly less diattenuating than uncoated surfaces.

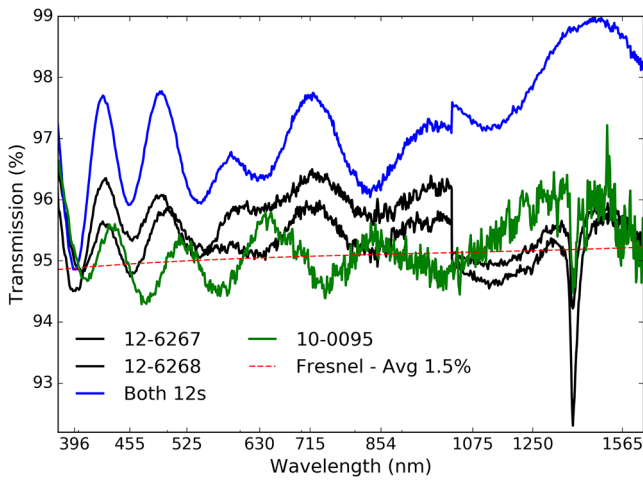


Fig. 70 The transmission in NLSP at normal incidence of the WBBAR1 coating on a Heraeus Infrasil 301-fused silica substrate. The test shot 10-0095 is shown in green. The two sides of a DKIST window are coated sequentially and are shown in black for runs 12-6267 and 12-6268. The combined two-surface coated sample transmission is shown in blue with larger oscillations.

Table 18 Photothermal.

λ (nm)	Side1 (ppm)	Side2 (ppm)
355	650	650
532	115	65
690	42	32
785	28	21
830	27	15
1064	10	5

We do not include the preliminary sample 7-4246 as the design changed slightly in response to a sensitivity analysis. We also note the offset in diattenuation between the visible and infrared spectrographs spliced at 1020 nm is due to the optical misalignment caused by the translation of the beam through a tilted sample.

Figure 70 shows the NLSP-measured transmission functions. At normal incidence (0 deg) we see reasonable agreement between NLSP metrology showing $\sim 1\%$ surface reflectivity hence 99% transmission on a single surface combined with the $\sim 3.8\%$ Fresnel reflection loss from the uncoated sample back surface. With a $\sim 1.5\%$ WBBAR1 average reflection loss, the transmission of a one-side coated sample should oscillate about an average of 94.7% transmission with peaks between 94.2% and 96.2% (max transmission, WBBAR1 reflectivity at zero). This is shown in Fig. 70 as the thin dashed red line. The two-side coated Infrasil sample is shown as the blue line with much higher transmission expectations, oscillating about 97.0%. The narrow spectral absorption spike around 1300 nm is caused by the fused silica used by IOI in their standard test samples.

In Table 18, we show the absorption in parts per million at wavelengths from the ultraviolet to NIR measured at Stanford Photothermal Solutions. We obtain low values, similar to our low-absorption isotropic MgF_2 coatings assessed as part of our prior calibration retarder thermal modeling.⁶⁹ Absorption at 355-nm wavelength is roughly 0.65% or 650 ppm in both coatings. The side two coating then shows absorption rapidly dropping to <100 ppm at visible wavelengths and <30 ppm at NIR wavelengths. This coating will not significantly contribute to the heating of most DKIST optics, which see roughly 80 W of optical power after the 2.8 arc min field stop at Gregorian focus.

The spectral oscillations are not repeatable run to run as a small fraction of a nanometer thickness layer variation can shift the oscillations while still preserving overall coating performance. We show examples of multiple repeated WBBAR coating runs in Fig. 71. The left graphic shows the wider WBBAR1 formula and the $<2.0\%$ absolute reflectivity spec with an average $<1.5\%$. The right-hand graphic shows six

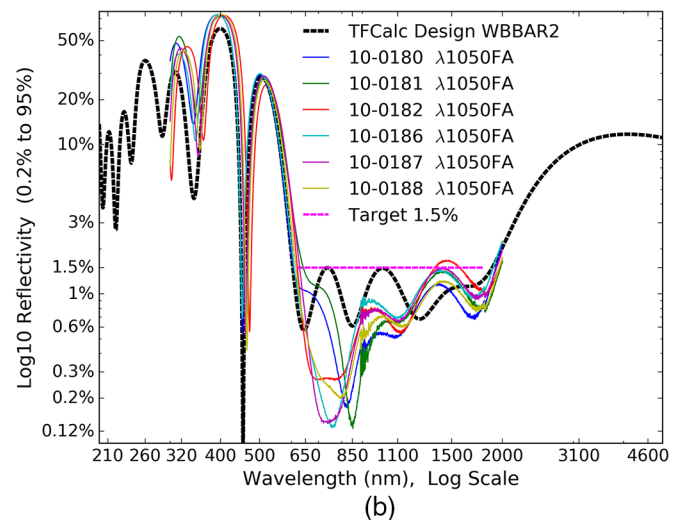
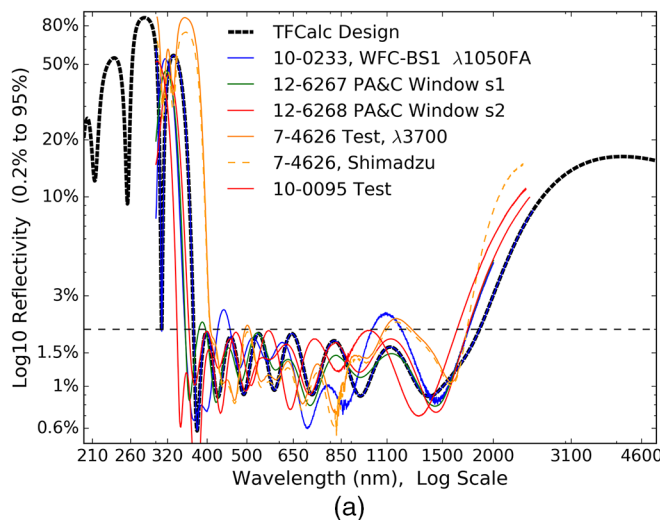


Fig. 71 Reflectivity measured for a single-surface reflection in multiple test coatings for the DKIST wide wavelength range antireflection coatings: WBBAR1 in (a) and WBBAR2 in (b). IOI measured the reflectivity of samples at their facility using either Shimadzu or Lambda (λ) spectrophotometers with various model numbers.

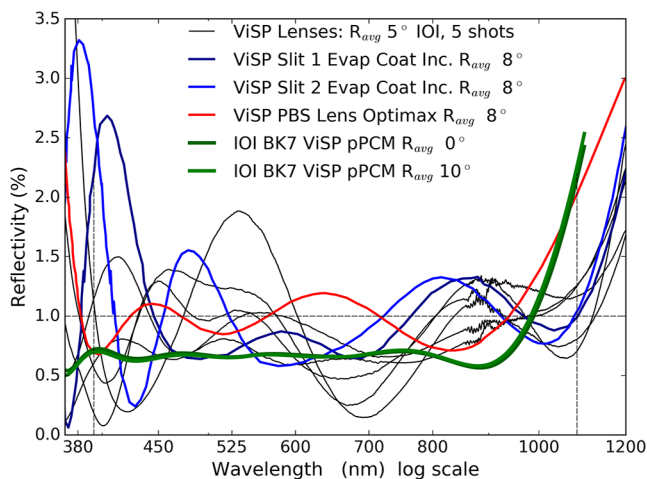


Fig. 72 Spectrophotometry measured by ECI for the ViSP slit entrance and exit interfaces at 8-deg incidence and is shown in blue. Optimax spectrophotometry at incidence angle 8 deg for the telecentric lens air-glass interfaces before bonding to the ViSP PBS. The upcoming polycarbonate modulator for ViSP from Meadowlark Optics will have BBAR-coated BK7 windows with the design from IOI shown in green.

sequential coating runs of the WBBAR2 formula done as part of our coating stress testing. The absolute reflectivity value spec is <1.5% in the 630- to 1800-nm wavelength range with an average <1.1%. Spectrophotometry is performed at IOI with their Lambda1050 FA system.

The DKIST throughput estimates also crucially depend on knowing the antireflection coatings on the many lenses and windows internal to the instruments. Coatings are often optimized for the specific bandpasses in each specific camera. The three ViSP camera arms can be configured to cover any ViSP wavelength and coatings are optimized for 380 to 950 nm with a goal to not significantly degrade performance at 1083 nm. In DL-NIRSP, a series of dichroic beam splitters limit the first camera to wavelengths shorter than 900 nm, the second camera to 950- to 1300-nm range, and the third camera to the 1400- to 1800-nm range.

Figure 72 shows the transmission measurements of the various coatings on the ViSP lenses. There are five coating shots at IOI to cover the lenses in the three ViSP cameras shown in black. The ViSP slit substrate has antireflection coatings on both sides from Evaporated Coatings Inc. (ECI) shown in light and dark blue. At shorter wavelengths, these coatings combine to reflect 5% of the light whereas longer wavelengths can have losses <1.5%. The spectral oscillations in the coatings can represent a significant uncertainty in the system flux budget. The PBS prisms are also coated by Optimax as shown in red. We also overlay a coating design from IOI we intend to use in an upcoming upgrade of the ViSP modulator. The specification is shown as the dashed black lines with an absolute value of <1.0% at any wavelength between 390 and 950 nm. The performance at the 1083-nm spectral line is still significantly below an uncoated Fresnel reflection loss.

We have compiled here examples of various antireflection coatings and their properties in transmission. Significant retardance of a few degrees can be observed depending on the complexity of the coating but the diattenuation of coated tilted surfaces is significantly reduced. The spectral oscillations are common and should be directly measured to ensure an accurate

throughput estimate. For DKIST, we also have oils and polycarbonate layers in various optics. The UV and IR bandpasses can see significant throughput changes depending on the oscillations of the coatings. Knowing the coating behavior into the UV impacts lifetime and damage estimates for these kinds of polarimetric optics common in solar telescopes.

12 Appendix E: Mueller Matrix Formalisms: (R_s, R_p, δ) or (X, τ)

Here we summarize the Mueller matrix terms and conventions for relating reflectivity and retardance to Mueller matrix elements.^{63,64,82} Many solar telescopes perform calibrations following an (X, τ) style Mueller matrix, where X relates to diattenuation and τ relates to retardance.^{48,49,61,83-86} We show how to relate this solar formalism to a reflectivity and phase formalism common in optics where strict equality between conventions allows us to compare reflectivity, diattenuation, and retardance.^{63,64,82}

We adopt a standard notation where the S and P polarization states represent incoming linear polarization states parallel and perpendicular to the plane of incidence. Their reflectivity is denoted as R_s and R_p , respectively, and their average is denoted as R_{avg} . Retardance is denoted as δ , which is the same as τ in the solar convention. In Eq. (13), we show a common definition of the Mueller matrix for a mirror folded along the $+Q$ plane. The II element is the average reflectivity. The retardance (δ) is a term in the UV rotation matrix in the lower right quadrant

$$\mathbf{M}_{ij} = \begin{pmatrix} R_{avg} & \frac{R_s - R_p}{2} & 0 & 0 \\ \frac{R_s - R_p}{2} & R_{avg} & 0 & 0 \\ 0 & 0 & \sqrt{R_p R_s} C_\delta & \sqrt{R_p R_s} S_\delta \\ 0 & 0 & -\sqrt{R_p R_s} S_\delta & \sqrt{R_p R_s} C_\delta \end{pmatrix} = R_{avg} \begin{pmatrix} 1 & \Delta & 0 & 0 \\ \Delta & 1 & 0 & 0 \\ 0 & 0 & \frac{\sqrt{R_p R_s}}{R_{avg}} C_\delta & \frac{\sqrt{R_p R_s}}{R_{avg}} S_\delta \\ 0 & 0 & -\frac{\sqrt{R_p R_s}}{R_{avg}} S_\delta & \frac{\sqrt{R_p R_s}}{R_{avg}} C_\delta \end{pmatrix}. \quad (13)$$

In the normalized Mueller matrix, the IQ/II and QI/II terms are a normalized reflectivity difference ratio $(R_s - R_p)/(R_s + R_p)$ often denoted with a capital delta (Δ). The lower right UV rotation matrix terms are modified by the scale factor $\frac{\sqrt{R_p R_s}}{R_{avg}}$. This term is above 0.999 for mirrors with diattenuation <10% as are all mirrors considered for DKIST

$$\mathbf{M}_{ij} = \frac{R_p}{2} \begin{pmatrix} 1 + \frac{R_s}{R_p} & 1 - \frac{R_s}{R_p} & 0 & 0 \\ 1 - \frac{R_s}{R_p} & 1 + \frac{R_s}{R_p} & 0 & 0 \\ 0 & 0 & 2\sqrt{\frac{R_s}{R_p}} C_\delta & 2\sqrt{\frac{R_s}{R_p}} S_\delta \\ 0 & 0 & -2\sqrt{\frac{R_s}{R_p}} S_\delta & 2\sqrt{\frac{R_s}{R_p}} C_\delta \end{pmatrix} = \frac{R_p}{2} \begin{pmatrix} 1 + X^2 & 1 - X^2 & 0 & 0 \\ 1 - X^2 & 1 + X^2 & 0 & 0 \\ 0 & 0 & 2XC_\delta & 2XS_\delta \\ 0 & 0 & -2XS_\delta & 2XC_\delta \end{pmatrix}, \quad (14)$$

$$R_{\text{avg}}\Delta = \frac{R_p}{2}(1 - X^2), \quad (15)$$

$$X^2 = 1 - \frac{R_s + R_p}{R_p}\Delta, \quad (16)$$

$$X^2 = 1 - \frac{2IQ}{(II + IQ)}, \quad (17)$$

$$\frac{IQ}{II} = \Delta = \frac{1 - X^2}{1 + X^2} = \frac{R_p - R_s}{R_p + R_s}, \quad (18)$$

$$X^2 = \frac{1 - \Delta}{1 + \Delta}. \quad (19)$$

A reflectivity ratio-denoted X can be computed from the IQ or QI elements of the intensity-normalized Mueller matrix (IQ/II or QI/II) and is typically near 1. Divide out one of the polarized reflectivities and denote the upper 2×2 submatrix in terms of intensity reflection coefficients $X = \sqrt{\frac{R_s}{R_p}}$ as in Eq. (14). The retardance is denoted as tau (τ). Other systems using this formalism include the Advanced Stokes Polarimeter (ASP) at the Dunn Solar Telescope (DST),⁶¹ the Hida Domeless Solar Telescope,^{83–85} the German Vacuum Tower Telescope,⁴⁸ and the Polarimetric Littrow Spectrograph,⁴⁹ and the solar tower in Arcetri.⁸⁶ We equate the two Mueller matrices and use IQ element to solve for X . Equation (13) gives the average mirror reflectivity (R_{avg}) times the normalized IQ element (Δ) giving the product: $R_{\text{avg}}\Delta$. This is equated to the Mueller matrix in Eq. (14) with intensity coefficient ($R_p/2$) times the normalized IQ element ($1 - X^2$). Equation (16) gives the relationship for X in terms of measured Mueller matrices and the relevant intensity scaling coefficients. We substituted $2R_{\text{avg}} = R_s + R_p$. Note that, in the limit of small diattenuation, $(R_s + R_p)/R_p$ is ~ 2 , but the scale factor between matrix conventions is $R_p/2$. If we compute the normalized Mueller matrix elements, we can equate the X values to the reflectivity ratios. A diagonalized convention for the Mueller matrix with a total transmission term outside the matrix and $II = 1$ is shown in Eq. (20).

The overall throughput term II is scaled by $\frac{R_p(1+X^2)}{2}$ for every matrix in our group model. As diattenuation is low, $X \sim 1$ and thus the overall throughput is close to 1. We also can solve for X using the terms in Eq. (20). The relations between (X , τ) and optical properties such as throughput and polarized reflectivities R_s and R_p are useful when comparing polarization calibrations and throughput estimates from these varying conventions

$$\mathbf{M}_{ij} = \frac{R_p(1 + X^2)}{2} \begin{pmatrix} 1 & \frac{1-X^2}{1+X^2} & 0 & 0 \\ \frac{1-X^2}{1+X^2} & 1 & 0 & 0 \\ 0 & 0 & \frac{2X}{1+X^2} C_\tau & \frac{2X}{1+X^2} S_\tau \\ 0 & 0 & \frac{-2X}{1+X^2} S_\tau & \frac{2X}{1+X^2} C_\tau \end{pmatrix} \\ = R_{\text{avg}} \begin{pmatrix} 1 & \Delta & 0 & 0 \\ \Delta & 1 & 0 & 0 \\ 0 & 0 & \frac{\sqrt{R_p R_s}}{R_{\text{avg}}} C_\delta & \frac{\sqrt{R_p R_s}}{R_{\text{avg}}} S_\delta \\ 0 & 0 & -\frac{\sqrt{R_p R_s}}{R_{\text{avg}}} S_\delta & \frac{\sqrt{R_p R_s}}{R_{\text{avg}}} C_\delta \end{pmatrix}. \quad (20)$$

Acknowledgments

This work was supported by the DKIST project. The DKIST is managed by the National Solar Observatory (NSO), which is operated by the Association of Universities for Research in Astronomy, Inc. (AURA) under a cooperative agreement with the National Science Foundation (NSF). This research made use of Astropy, a community-developed core Python package for Astronomy (Astropy Collaboration, 2013). We acknowledge the community effort devoted to the development of the following open-source packages used in this work: numpy(numpy.org) and matplotlib(matplotlib.org). We thank Thomas Kentischer, Lucia Kleint, Manolo Collados, and the KIS staff for mirror samples and discussions about GREGOR mirror polarization. We thank Kwangsu Ahn at BBSO for assisting us understand their polarimeter optical performance and for the BBSO mirror samples. We thank David Elmore for his assistance, guidance, and insight into the long history of work on the DKIST project. We thank Tom Schad, Sarah Jaeggli, and Christian Beck for their ongoing discussions of polarization performance at various telescopes. This research has made use of NASA's Astrophysics Data System Bibliographic Services.

References

1. J. P. McMullin et al., "Construction status of the Daniel K. Inouye Solar Telescope," *Proc. SPIE* **9145**, 914525 (2014).
2. S. L. Keil et al., "ATST: the largest polarimeter," in *Proc. Conf. Held in Maui*, Vol. **437**, p. 319 (2011).
3. T. R. Rimmele et al., "Instrumentation for the Advanced Technology Solar Telescope," *Proc. SPIE* **5492**, 944 (2004).
4. J. Marino, E. Carlisle, and D. Schmidt, "Simulation of DKIST solar adaptive optics system," *Proc. SPIE* **9909**, 99097C (2016).
5. J. P. McMullin et al., "Construction status of the Daniel K. Inouye Solar Telescope," *Proc. SPIE* **9906**, 99061B (2016).
6. L. C. Johnson et al., "Status of the DKIST system for solar adaptive optics," *Proc. SPIE* **9909**, 99090Y (2016).
7. D. F. Elmore, S. R. Sueoka, and R. Casini, "Performance of polarization modulation and calibration optics for the Daniel K. Inouye Solar Telescope," *Proc. SPIE* **9147**, 91470F (2014).
8. D. F. Elmore et al., "The Daniel K. Inouye Solar Telescope first light instruments and critical science plan," *Proc. SPIE* **9147**, 914707 (2014).
9. W. Schmidt et al., "A two-dimensional spectropolarimeter as a first-light instrument for the Daniel K. Inouye Solar Telescope," *Proc. SPIE* **9147**, 91470E (2014).
10. H. Socas-Navarro et al., "High precision polarimetry with the Advanced Technology Solar Telescope," *Solar Phys. Space Weather Instrum.* **5901**, 52 (2005).
11. D. M. Harrington and S. R. Sueoka, "Polarization modeling and predictions for Daniel K. Inouye Solar Telescope part 1: telescope and example instrument configurations," *J. Astron. Telesc. Instrum. Syst.* **3**, 018002 (2017).
12. D. M. Harrington, J. R. Kuhn, and A. L. Ariste, "Daytime sky polarization calibration limitations," *J. Astronom. Telesc. Instrum. Syst.* **3**(1), 018001 (2017).
13. D. M. Harrington et al., "Polarization modeling and predictions for DKIST part 2: application of the Berreman calculus to spectral polarization fringes of beamsplitters and crystal retarders," *J. Astron. Telesc. Instrum. Syst.* **3**, 048001 (2017).
14. D. W. Berreman, "Optics in stratified and anisotropic media: 4X4-matrix formulation," *J. Opt. Soc. Am.* **62**, 502 (1972).
15. M. W. McCall, I. J. Hodgkinson, and Q. Wu, *Birefringent Thin Films and Polarizing Elements*, 2nd Ed., Vol. **1**, Imperial College Press, London (2014).
16. D. M. Harrington and S. R. Sueoka, "Polarization modeling and predictions for DKIST part 3: focal ratio and thermal dependencies of spectral polarization fringes and optic retardance," *J. Astron. Telesc. Instrum. Syst.* **4**(01), 1 (2018).
17. D. M. Harrington and S. R. Sueoka, "Polarization modeling and predictions for Daniel K. Inouye Solar Telescope part 4: calibration

- accuracy over field of view, retardance spatial uniformity, and achromat design sensitivity," *J. Astron. Telesc. Instrum. Syst.* **4**, 1–49 (2018).
18. S. R. Sueoka, R. A. Chipman, and D. F. Elmore, "Characterization of DKIST retarder components with polarization ray tracing," *Proc. SPIE* **9293**, 929308 (2014).
 19. W. H. Schubert, E. Petrak, and T. G. Baur, "Measurement of polarization assemblies for the Daniel K. Inouye Solar Telescope," *Proc. SPIE* **9369**, 93690N (2015).
 20. A. G. de Wijn et al., "Preliminary design of the visible spectro-polarimeter for the Advanced Technology Solar Telescope," *Proc. SPIE* **8446**, 84466X (2012).
 21. S. Sueoka, "Polarization optical components of the Daniel K. Inouye Solar Telescope," *PhD Thesis*, University of Arizona (2016).
 22. J. Sánchez-Capuchino et al., "Current concept for the 4m European Solar Telescope (EST) optical design," *Proc. SPIE* **7733**, 99 (2010).
 23. F. C. M. Bettonvil et al., "The polarization optics for the European Solar Telescope (EST)," *Proc. SPIE* **7735**, 214 (2010).
 24. M. Collados et al., "European Solar Telescope: project status," *Proc. SPIE* **7733**, 15 (2010).
 25. B. Yao, N. T. Gu, and C. H. Rao, "Optical compensation of the Chinese Large Solar Telescope instrumental polarization," *J. Opt. Technol.* **85**(10), 639 (2018).
 26. S. Yuan, Y. Fu, and Z. Jin, "Polarization modeling for the main optics of Chinese Giant Solar Telescope," *Proc. SPIE* **1001**, 1001205 (2016).
 27. M. De Juan Ovelar et al., "Instrumental polarisation at the Nasmyth focus of the E-ELT," *Astron. Astrophys.* **562**, A8 (2014).
 28. F. Joos et al., "Reduction of polarimetric data using Mueller calculus applied to Nasmyth instruments," *Obs. Oper.* **7016**, 48 (2008).
 29. C. U. Keller and F. Snik, "Polarimetry from the ground up," in *Solar Polarization 5: In Honor of Jan Stenflo ASP Conf. Series* Vol. **405**, p. 371 (2009).
 30. C. U. Keller et al., "EPOL: the exoplanet polarimeter for EPICS at the E-ELT," *Proc. SPIE* **7735**, 212 (2010).
 31. C. U. Keller, "Solar polarimetry close to the diffraction limit," *Proc. SPIE* **4843**, 100 (2003).
 32. M. Rodenhuis et al., "The extreme polarimeter: design, performance, first results and upgrades," *Proc. SPIE* **8446**, 84469I (2012).
 33. R. Roelfsema et al., "The ZIMPOL high-contrast imaging polarimeter for SPHERE: design, manufacturing, and testing," *Proc. SPIE* **7735**, 144 (2010).
 34. J. Sánchez Almeida, "Instrumental polarization in the focal plane of telescopes. 2: Effects induced by seeing," *Astron. Astrophys.* **292**, 713–721 (1994).
 35. J. Sánchez Almeida and V. Martínez Pillet, "Instrumental polarization in the focal plane of telescopes," *Astron. Astrophys.* **260**, 543–555 (1992).
 36. J. Sánchez Almeida, V. Martínez Pillet, and A. D. Wittmann, "The instrumental polarization of a Gregory-Coude telescope," *Solar Phys.* **134**, 1–13 (1991).
 37. W. Schmidt et al., "POLIS: a spectropolarimeter for the VTT and for GREGOR," *Astronomische Nachrichten* **324**, 300 (2003).
 38. F. Snik et al., "Design of a full-Stokes polarimeter for VLT/X-shooter," *Proc. SPIE* **8446**, 844625 (2012).
 39. F. Snik et al., "The upgrade of HARPS to a full-Stokes high-resolution spectropolarimeter," *Proc. SPIE* **7014**, 701400 (2008).
 40. F. Snik, "Calibration strategies for instrumental polarization at the 10-5 level," *Proc. SPIE* **6269**, 182 (2006).
 41. H. Socas-Navarro et al., "Characterization of telescope polarization properties across the visible and near-infrared spectrum. Case study: the Dunn Solar Telescope," *Astron. Astrophys.* **531**, 2 (2011).
 42. H. Socas-Navarro, "Polarimetric calibration of large-aperture telescopes. II. Subaperture method," *J. Opt. Soc. Am. A* **22**, 907 (2005).
 43. H. Socas-Navarro, "Polarimetric calibration of large-aperture telescopes. I. Beam-expansion method," *J. Opt. Soc. Am. A* **22**, 539 (2005).
 44. P. Spano et al., "Optical design of CAOS: a high-resolution spectropolarimeter for the Catania Astrophysical Observatory 0.91-m telescope," *Ground Instrum. Astron. Proc. SPIE* **5492**, 373 (2004).
 45. K. G. Strassmeier et al., "PEPSI: the Potsdam Echelle Polarimetric and Spectroscopic Instrument for the LBT," *Proc. SPIE* **7014**, 21 (2008).
 46. K. G. Strassmeier et al., "PEPSI spectro-polarimeter for the LBT," *Proc. SPIE* **4843**, 180 (2003).
 47. J. Tinbergen, "Accurate optical polarimetry on the Nasmyth platform," *Publ. Astron. Soc. Pacif.* **119**, 1371–1384 (2007).
 48. C. Beck et al., "A polarization model for the German Vacuum Tower Telescope from in situ and laboratory measurements," *Astron. Astrophys.* **443**, 1047–1053 (2005).
 49. C. Beck et al., "Polarimetric Littrow spectrograph—instrument calibration and first measurements," *Astron. Astrophys.* **437**, 1159–1167 (2005).
 50. J. Marino, "Expected performance of solar adaptive optics in large-aperture solar telescopes," *Opt. Eng.* **51**(10), 101709 (2012).
 51. D. Schmidt et al., "Clear widens the field for observations of the Sun with multi-conjugate adaptive optics," *Astron. Astrophys.* **597**, L8–L4 (2017).
 52. D. Schmidt et al., "A review of solar adaptive optics," *Proc. SPIE* **9909**, 99090X (2016).
 53. D. Schmidt et al., "Progress in multi-conjugate adaptive optics at Big Bear Solar Observatory," *Proc. SPIE* **9909**, 990929 (2016).
 54. W. Schmidt et al., "End-to-end simulations of the visible tunable filter for the Daniel K. Inouye Solar Telescope," *Proc. SPIE* **9908**, 99084N (2016).
 55. S. A. Jaeggli, "An observational study of the formation and evolution of sunspots," PhD Thesis (2011).
 56. J. C. del Toro Iniesta and V. Martínez Pillet, "Assessing the behavior of modern solar magnetographs and spectropolarimeters," *Astrophys. J. Suppl. Ser.* **201**, 22 (2012).
 57. <https://dkist.nso.edu/CSP/instruments>
 58. D. M. Harrington and S. R. Sueoka, "Polarization modeling and predictions for Daniel K. Inouye Solar Telescope part 1: telescope and example instrument configurations," *J. Astron. Telesc. Instrum. Syst.* **3**, 018002 (2017).
 59. K. Ichimoto et al., "Polarization calibration of the Solar Optical Telescope onboard Hinode," *Solar Phys.* **249**, 233–261 (2008).
 60. W. T. Thompson, "Coordinate systems for solar image data," *Astron. Astrophys.* **449**(2), 791–803 (2006).
 61. A. Skumanich et al., "The calibration of the advanced stokes polarimeter," *Astrophys. J. Suppl. Ser.* **110**, 357–380 (1997).
 62. E. Collett, *Polarized Light. Fundamentals and Applications*, Vol. **1**, CRC Press (1992).
 63. R. A. Chipman, "Handbook of optics," in *Polarimetry*, 3rd ed., Vol. **1**, McGraw Hill, New York (2014).
 64. R. A. Chipman, "Handbook of optics," in *Mueller Matrices*, 3rd ed., M. Bass, Vol. **1**, McGraw Hill, New York (2010).
 65. F. Snik and C. U. Keller, *Astronomical Polarimetry: Polarized Views of Stars and Planets*, 2nd ed., Vol. **1**, Springer, Dordrecht (2013).
 66. D. M. Harrington et al., "Polarization modeling and predictions for DKIST part 2: application of the Berreman calculus to spectral polarization fringes of beamsplitters and crystal retarders," *J. Astronom. Telesc. Instrum. Syst.* **3**, 048001 (2017).
 67. D. M. Harrington, J. R. Kuhn, and A. L. Ariste, "Daytime sky polarization calibration limitations," *J. Astronom. Telesc. Instrum. Syst.* **3**, 018001 (2017).
 68. R. Boidin et al., "Pulsed laser deposited alumina thin films," *Ceram. Int.* **42**, 1177–1182 (2016).
 69. D. M. Harrington and S. R. Sueoka, "Polarization modeling and predictions for DKIST part 3: focal ratio and thermal dependencies of spectral polarization fringes and optic retardance," arXiv.org, **1** (2018).
 70. C. R. Givens and A. B. Kostinski, "A simple necessary and sufficient condition on physically realizable Mueller matrices," *J. Mod. Opt.* **40**, 471 (1993).
 71. A. B. Kostinski, C. R. Givens, and J. M. Kwiatkowski, "Constraints on Mueller matrices of polarization optics," *Appl. Opt.* **32**, 1646 (1993).
 72. R. Chipman, "Classification of depolarizing Mueller matrices," in *Spatially Variant Polarization Fields, Polarized Speckle Patterns, Polarized Vortices and Polarization Aberrations II*, Frontiers in Optics, Washington, D.C. (2006).
 73. K. Twietmeyer and R. Chipman, "Condition number as a metric for the effectiveness of polarimetric algorithms," *Front. Opt.* (2005).
 74. R. A. Chipman, "Depolarization in the Mueller calculus," *Proc. SPIE* **5158**, 184–192 (2003).
 75. D. H. Goldstein and R. A. Chipman, "Error analysis of a Mueller matrix polarimeter," *J. Opt. Soc. Am. A* **7**, 693–700 (1990).
 76. R. A. Chipman, E. A. Sornsin, and J. L. Pezzaniti, "Mueller matrix imaging polarimetry: an overview," *Proc. SPIE* **2873**, 5–12 (1996).

77. H. D. Noble and R. A. Chipman, "Mueller matrix roots," *PhD Thesis*, The University of Arizona (2011).
78. H. D. Noble and R. A. Chipman, "Mueller matrix roots algorithm and computational considerations," *Opt. Express* **20**, 17 (2012).
79. H. D. Noble, S. C. McClain, and R. A. Chipman, "Mueller matrix roots depolarization parameters," *Appl. Opt.* **51**, 735 (2012).
80. R. A. Chipman, "Structure of the Mueller calculus," *Proc. SPIE* **4133**, 1–9 (2000).
81. J. B. Breckinridge et al., "Terrestrial exoplanet coronagraph image quality: study of polarization aberrations in Habex and LUVOIR update," *Proc. SPIE* **1069**, 106981D (2018).
82. R. A. Chipman, W. S. T. Lam, and G. Young, *Polarized Light and Optical Systems*, CRC Press, New York (2018).
83. M. Makita, Y. Funakoshi, and Y. H. S. Polarimetry, "Polarization of the Domeless Solar Telescope of the Hida Observatory (Preliminary report)," in *Solar Polarimetry NSO/SP Summer Workshop 11*, pp. 198–201 (1991).
84. J. Kiyohara et al., "Calibration of the instrumental polarization of the Domeless Solar Telescope at the Hida Observatory," *Ground Instrum. Astron.* (2004).
85. Y. Hanaoka, "Spectropolarimetry with the Hida Domeless Solar Telescope," *Publ. Astron. Soc. Jpn.* **61**(2), 357–365 (2009).
86. C. Capitani et al., "Polarization properties of a Zeiss-type coelostat: the case of the solar tower in Arcetri," *Solar Phys.* **120**(1), 173–191 (1989).

Biographies for the authors are not available.